TR-ACR-0002

Lateral Junction Light Emitting Devices Fabricated on GaAs(311)A-oriented Substrates

Yohei Hashizume*, Pablo O. Vaccaro
and Akira Sugimura**

*Sanyo Electric Co. Ltd. **Konan University

2001.11.28

(株)国際電気通信基礎技術研究所
適応コミュニケーション研究所
〒619-0288 京都府相楽郡精華町光台二丁目 2 番地 2
Tel: 0774-95-1501 Fax: 0774-95-1508

Advanced Telecommunications Research Institute International
Adaptive Communications Research Laboratories
2-2-2 Hikaridai, Seika-cho, Soraku-gun, Kyoto 619-0288, Japan
Telephone: +81-774-95-1501 Fax: +81-774-95-1508

©2001 (株)国際電気通信基礎技術研究所
©2001 Advanced Telecommunications Research Institute International

Abstract

Light emitting devices with an unconventional structure that includes a lateral p-n junction were studied. This lateral p-n junction can be formed by taking the advantage of the crystal orientation dependence of the amphoteric properties of silicon dopant in GaAs. In this research, the lateral p-n junctions were fabricated with Si-doped GaAs epilayers grown by molecular beam epitaxy (MBE) on GaAs(311)A-oriented substrates that were patterned before growth to alternately expose slopes of different orientations. Two types of lateral junction light emitting diodes (LEDs) and a lateral junction vertical-cavity surface-emitting laser (VCSEL) were fabricated and measured. LEDs with an active layer composed of GaAs/$Al_{0.5}Ga_{0.5}As$ 30 periods multiple quantum well (MQW) were fabricated and the visible electoluminescence (EL) spectra was observed up to room temperature. Modulation doped LEDs with an active layer composed of an $In_{0.2}Ga_{0.8}As$/GaAs single quantum well (SQW) with non-doped GaAs barriers were fabricated and peculiar EL spectra were obtained. In the EL spectra a flat portion that is nearly independent of measurement temperature shows the presence of a two-dimensional hole gas in the p-type region. An optically-pumped VCSEL with an active layer composed of 5 $In_{0.2}Ga_{0.8}As$/GaAs quantum wells (QWs) and non-doped GaAs barriers was fabricated. From PL spectra, high reflectivity tuned DBRs were successfully fabricated with optimized oxidation conditions. On set of amplified spontaneous emission was obtained with very low excitation laser power of 60.6 mW.

Contents

Chapter 1

Introduction

Conventional (Vertical) p-n junction devices such as laser diodes (horizontal and vertical cavity types) have electrons and holes injected in the active layer through higher bandgap layers for optical confinement. Therefore, carriers have unnecessary energy excess and they have to thermalize before becoming available for radiative recombination. This relaxation time effect is an intrinsic limitation to the modulation bandwidth in the present design of semiconductor lasers.[1][2]

In this thesis, we investigate a new solution that consists of a lateral p-n junction structure. The lateral p-n junction is formed by growing the Si-doped GaAs epilayer with the molecular beam epitaxy (MBE) process on a GaAs (311)A-oriented patterned substrate that exposes slopes of different orientations. Due to amphoteric properties of Si in GaAs grown on high index (n11)A-oriented substrates,[3][4] p-type doping is obtained on the flat region of the substrate and n-type doping is obtained on the slopes of the substrate, thus a lateral p-n junction is formed.

Basic properties of the lateral p-n junction have been reported,[5] and a few devices using this lateral junction structure such as lateral tunneling diodes and transistors have been demonstrated.[6] The processing of lateral junction devices is simpler than that of conventional vertical devices. Also, the device process simplifies the combination with other planar devices as the Field Effect transistors (FET) and High Mobility Transistors (HEMT) in LSIs. However, recent focus is on the superior advantages that the lateral p-n junction could exhibit when applied laser diodes.[7] This is because, the lateral p-n junction allows direct injection of electrons and holes in the active layer of a laser diode without having to pass through any higher bandgap material, therefore, carriers have little energy excess that reduces relaxation time and increases modulation bandwidth. Moreover, the applied bias required to inject a given current can be reduced and the power efficiency of device would improve. Besides, the lateral junction area can be made orders of magnitude smaller as compared to vertical junctions, with consequent reduction of device capacitance. This lateral p-n junction can be used for making both horizontal and vertical cavity laser diodes.

The goal of this research is fabricating this new laser diode successfully. In order to reach the goal, I first fabricated and measured two types of lateral junction light emitting diodes

(LEDs) to study carrier transport in the lateral p-n junction. One is a visible LED with an active layer composed of GaAs/$Al_{0.5}Ga_{0.5}As$ 30 periods multiple quantum well (MQW) and a bottom distributed Bragg reflectors (DBR) composed of AlAs (oxidized)/$Al_{0.5}Ga_{0.5}As$ 4.5 periods multiple layer structure. The other is a modulation doped LED with an active layer composed of $In_{0.2}Ga_{0.8}As$ single quantum well (SQW) with non-doped GaAs barriers. Each LED was evaluated through electrical and optical measurements, and a thorough investigation on the electroluminescence (EL) of the devices is reported. Finally, an optically-pumped lateral junction vertical-cavity surface-emitting laser (VCSEL) with an active layer composed of 5 $In_{0.2}Ga_{0.8}As$ quantum wells (QWs) and non-doped GaAs barriers is fabricated and measured. Si-doped GaAs layers are sandwiched by QWs in the cavity to make the lateral p-n junction. The top and bottom DBRs are formed by 3 and 4 periods of AlAs (oxidized)/$Al_{0.5}Ga_{0.5}As$ layers, respectively. VCSEL was evaluated through optical measurement, and a thorough investigation on the photoluminescence (PL) of the devices is also reported.

This thesis has the following structure. In Chapter 2, the basic theories and background on which this research is based are reviewed. The Si-doping characteristics in GaAs epilayers, the basic mechanism of a semiconductor light emitting device, and the advantages of a lateral p-n junction laser diode are described in this chapter. Fabrication methods and characterizations (electrical and optical) used in two types of lateral junction LEDs are presented in Chapter 3 and 4. Finally, fabrication method and optical characterization of VCSELs are presented in Chapter 5.

Chapter 2

Lateral p-n junctions

2.1 p-n junction diodes

The p-n junction is the vital component of most semiconductor devices. In this section I briefly discuss the concept of the p-n junction and the optical phenomena in LEDs.

2.1.1 p-n junctions

A p-n junction is made from a single crystal modified in two separate regions. Acceptor impurity atoms are incorporated into one part to produce the p-region in which the majority carriers are holes. Donor impurity atoms in the other part produce the n-region in which the majority carriers are electrons. The interface region may be less than 10^{-4} cm thick. Away from the junction region on the p-side there are $(-)$ ionized acceptor impurity atoms and an equal concentration of free holes. On the n-side there are $(+)$ ionized donor atoms and an equal concentration of free electrons. Thus the majority carriers are holes on the p-side and electrons on the n-side, Fig. 2.1.

Holes concentrated on the p-side would like to diffuse to fill the crystal uniformly. Electrons would like to diffuse from the n-side. But diffusion will upset the local electrical neutrality of the system.

A small charge transfer by diffusion leaves behind on the p-side an excess of $(-)$ ionized acceptors and on the n-side an excess of $(+)$ ionized donors. This charge double layer creates an electric field directed from n to p that inhibits diffusion and thereby maintains the separation of the two carrier types. Because of this double layer the electrostatic potential in the crystal takes a jump in passing through the region of the junction.[8]

2.1.2 Principle of LEDs

Photonic devices are those in which the basic particle of light-the photon, plays a major role. Photonic devices can be divided into three groups: (1) devices that convert electrical energy into optical radiation-the LED and the diode laser (light amplification by stimulated

emission of radiation), (2) devices that detect optical signals through electronic processes-photo detectors, and (3) devices that convert optical radiation into electrical energy-the photovoltaic device or solar cell. Then, I shall review the first group in this subsection.

Radiative transitions

The LEDs and semiconductor lasers belong to the luminescence device family. Luminescence is the emission of optical radiation (ultraviolet, visible, or infrared) as a result of electronic excitation of a material, excluding any radiation that is purely the result of the temperature of the material (incandescence). Type of luminescence may be distinguished by the source of input energy: (1) photoluminescence involving excitation by optical radiation, (2) cathodoluminescence by electron beam or cathode ray, (3) radioluminescence by other fast particles or high-energy radiation, and (4) electroluminescence by electric field or current. Here I shall mention electroluminescence, especially with injection electroluminescence; that is, optical radiation obtained by injecting minority carriers into the region of a semiconductor p-n junction where radiative transitions take place.

Figure 2.2 schematically shows the basic transitions in a semiconductor. These transitions may be classified as follows. The first classification type is the interband transitions: (a) intrinsic emission corresponding very closely in energy to bandgap, where phonons or excitons may be involved, and (b) higher-energy emission involving energetic or hot carriers, sometimes related to avalanche emission. The second classification type is the transition involving chemical impurities or physical defects; (a) conduction band to acceptor, (b) donor to valence band, (c) donor to acceptor (pair emission), and (d) deep levels. The third classification type is the interband transition involving hot carriers, sometimes called deceleration emission.

Not all transitions can occur in the same material or under the same conditions, and not all transitions are radiative. An efficient luminescencent material is one in which radiative transitions predominate over non-radiative ones.

Emission spectra

There are three processes for interaction between a photon and an electron in a solid. A photon may be absorbed by the transition of an electron from a filled state in a valence band to an empty state in the conduction band. In addition to being absorbed, a photon can stimulate the emission of a similar photon by the transition of an electron from a filled state in the conduction band to an empty state in the valence band. Also, an electron in the conduction band can spontaneously return to an empty state in the valence band with the emission photon.

The spontaneous emission rate depends in the density of filled conduction band states and the density of empty valence band states and may be written as

$$I(h\nu) \sim \nu \langle M \rangle^2 N_C N_V F_C(E) F_V(E) \tag{2.1}$$

Where $\langle M \rangle$ is called the transition matrix element, N_C is the density of state in the

conduction band, N_V is the density of states in the valence band, $F_C(E)$ and $F_V(E)$ are, respectively, the electron and hole Fermi Dirac distribution functions. The spontaneous emission rate generally has the form

$$I(h\nu) \sim \nu^2 (h\nu - E_g)^{1/2} \exp[-(h\nu - E_g)/kT] \tag{2.2}$$

Where E_g is the bandgap.[9]

At the impurity densities often encountered for LEDs and semiconductor lasers, the representation of localized impurity levels separated from the band edges cannot be used. Instead, the random distribution of charged impurities in the crystal results in potential fluctuation, which produce tails in the conduction band and valence band density of states.

LEDs can emit external radiation under proper forward-biased conditions, by utilizing phenomena mentioned above. Fig. 2.3 shows the basic band diagram of an operating LED. When a forward bias is applied, electrons are injected from the n-type region into the p-type region, and holes are injected in a reverse manner, causing the increase of minority carriers. These carriers recombine with the majority carriers, and if the process is radiative, an optical radiation is obtained. The wavelength of the radiation is mainly dependent on the bandgap energy of the material where the recombination takes places and can be expressed as

$$\lambda = \frac{1239.8}{E_g} \tag{2.3}$$

where λ (nm) is the wavelength and E_g (eV) is the energy bandgap.

2.2 Lateral p-n junctions

Silicon is widely used as an n-type dopant in GaAs growth using MBE. However, it has been reported that in GaAs growth on GaAs (n11)A substrate, Si atoms are incorporated as acceptors when n≤3.[3][4] Due to the unique bonding structure on GaAs (n11)A surface, the condition type of a Si-doped layer for GaAs growth on GaAs(n11)A (n≤3) can be controlled by the MBE growth conditions and crystal orientations.[10] In this section I shall review the interesting properties of Si which are used to fabricate lateral p-n junctions.

2.2.1 Incorporation behavior of Si in GaAs

Si, the group IV element, is expected to act either as donors or acceptors in III-V compound semiconductors such as GaAs depending on which substantial site they occupied. As shown in Fig. 2.4, If Si atoms are incorporated into Ga sites, they act as donors, so the conductivity of the GaAs layer becomes n-type (a). Conversely, If Si atoms occupy As sites, they act as acceptors and the grown layer becomes p-type (b).

This amphoteric characteristic of Si and its incorporation behavior in MBE growth have been studied and reported extensively.[11][12][13][14][15] The Si incorporation site is mainly dependent on the crystal orientation of the substrate, but it is also greatly affected by the

MBE growth conditions such as substrate temperature and the V/III flux ratio as shown in the following subsections.

2.2.2 Si-doping dependence on crystal orientation

Si-doping characteristics in GaAs are mainly affected by the atomic arrangements of different surfaces on GaAs substrate orientation. Fig. 2.5 shows a sectional view of the ideal atomic structure of GaAs.

On GaAs (100) surfaces, If Si atoms bond to the two As bonds, they act as donors and if Si atoms bond to the two Ga bonds, they act as acceptors. However, under the As-rich, far from thermodynamical equilibrium conditions found in the MBE growth, Si bonds preferentially to As and epilayers become n-type. Nearly all Si atoms (up to 6×10^{18} cm^{-3}) occupy Ga sites and the Si doped GaAs layers grown by MBE on (100) oriented substrates are nearly always n-type.[11] However, as the Si concentration is increased further, Si atoms begin to occupy As sites and the free-electron carrier concentration n increases only slightly for standard MBE growth. So, the carrier concentration n reaches a maximum value (7×10^{18} cm^{-3}) before decreasing for higher Si-doping concentration.

Due to the unique bonding structure on GaAs (n11)A (n$\leq$3) surfaces, the conduction types of Si-doped GaAs layers can be further controlled. As shown in Fig. 2.4, GaAs (111)A surface has single dangling bonds from Ga atoms. The valence band electron density of this single dangling bond site is believed to be very low. So, little energy is available for decomposing the incoming As_4 molecule. Consequently, Si atoms occupy preferentially As sites, because of the low As atoms population at the surface. Thus, Si atoms usually act as a p-type dopant in the layer grown on this plane. However, when the (111)A substrate is tilted slightly toward the (100) orientation, a large number of surface steps with a (100)-like bonding geometry appear at the surface as shown in Fig. 2.6.[11] These (100) steps can promote the decomposition of As_4 molecules and induce lateral growth from the steps leading to a (100)-like incorporation of Si atoms.[11] Therefore, the conductivity type is determined by a competition between Si incorporation in (111)A terrace sites and in (100) step sites as shown in Fig. 2.6. By misorienting further the (111)A surface, the (100)-step density increases, resulting in a higher probability of n-type growth. The (311)A surface clearly shows these two kinds of bonding sites at equal densities: double dangling bond sites formed on (100) steps and single dangling bond sites formed on (111)A terraces. Due to this characteristic surface structure, the incoming Si atoms can behave either as donors or acceptors and they have such the strongly amphoteric property.

The distribution of the Si atoms between these two sites depends not only on the relative bond strength between Si and Ga or As, but also on the competition that Si atoms encounter to occupy sites. Si atoms have to compete with incoming Ga atoms or As atoms to occupy a donor or an acceptor sites, respectively. This competition can be controlled by the MBE growth conditions.

2.2.3 Si-doping dependence on MBE growth conditions

The conductivity of Si-doped GaAs layers grown on high-index substrates is also greatly affected by the substrate temperature and V/III flux ratio during MBE growth. By increasing the temperature of the substrate, desorption of the arsenic species from the surface becomes more important. Consequently, low substrate temperatures enhance incorporation of Si atoms into Ga sites, then n-type epilayers are produced. In particular, the GaAs (111)A surface has a stronger dependence on growth temperature regarding the Si-doping than other surfaces. The V/III flux ratio during the MBE growth is also an important factor in controlling the surface concentration of As atoms. When the V/III ratio is low, the plentiful supply of Ga atoms competes with Si for Ga sites; hence, the Si atoms preferably occupy the As sites. However, by increasing the V/III ratio, the As surface coverage increases and As atoms are enough to fill the As vacancies. Thus, the incorporation of Si atoms in As sites can be reduced. The GaAs (311)A surface has the largest dependence on V/III flux ratio on all Si-doped high index GaAs surfaces. Thus by controlling the V/III flux ratio, p or n-type epilayers having low carrier compensation can be obtained on GaAs (311)A substrates.

Based on the interesting properties of Si mentioned above, lateral p-n junctions can be made on patterned GaAs (n11)A-oriented ($n \leq 3$) substrates and high quality epilayers on GaAs (311)A-oriented substrates can be grown. Under optimized MBE growth conditions, we can obtain p-type doping on the flat regions and n-type doping on properly oriented slope of the patterned substrates. This fabrication method of lateral p-n junctions requires the MBE growth only once.

Lateral p-n junctions have particular properties that are promising for application in new devices. Junction area is controlled by the thickness of the Si-doped epilayer that can be as thin as one atomic single layer; therefore, junction area can be made orders of magnitude smaller than in conventional p-n junctions. The p-type and n-type regions are side by side on the sample surface. Therefore, all the electric contacts can be made on the same side of the sample using a coplanar geometry. Moreover electrically insulating substrates can be used, simplifying electrical isolation of multiple devices made on the same substrate. Besides, the junction can be clad between non-doped epitaxial layers that reduce leakage current and produce carrier confinement. Finally, when undoped quantum wells are included in the structure, carriers in the lateral p-n junction are transferred inside the quantum wells (modulation doping) and transported in the plane of the wells, where carriers have a high mobility.

Chapter 3

Lateral junction visible LEDs

3.1 Fabrication

Conventional LEDs have a large portion of the light emitting area covered by the top contact. This configuration obstructs light emission and reduces total efficiency. On the other hand, lateral junction LEDs have contacts placed on the side of the light emitting area, and light emission is not obstructed. Fig. 3.1 shows the process flow diagram of lateral junction LEDs. The fabrication process is as follows.

1. Pretreatment

GaAs (311)A semi-insulating (CrO-doped) substrates were cut to 1.5 cm × 2.0 cm for MBE growth. The substrates were cleaned with acetone for 3 minutes and deionized water for 3 minutes in an ultrasonic cleaner. After an ultrasonic cleaning, substrates were blown by N_2 gas, and then dried at 125 ℃ for 10 minutes.

2. Substrate patterning (Mesa wet etching)

Mesa of 500×250 μm^2 were patterned on GaAs (311)A-oriented substrates using conventional photolithography and wet etching with H_3PO_4:H_2O_2:H_2O (3:1:50, 40 ℃, 18 min.). (Fig. 3.2) The longest side of mesas was along the $[0\bar{1}1]$ direction. The angle θ between the patterned slope and the substrate plane was about 16.7 degrees, and the orientation of slope was near (100) plane.

3. MBE growth

The patterned substrates were etched in HCl to remove native oxides and NH_4OH:H_2O_2:H_2O (2:1:96) to obtain a stoichiometric surface. These processes were taken just before introducing the patterned substrates into a Varian Modular Gen MBE chamber. The detailed surface treatment process is shown in Fig. 3.3. And the conditions used in the MBE growth are listed in Table 3.1.

The MBE layer structure is shown in Fig. 3.4. The substrate was rotated during growth to obtain even epilayers. First, a 100 nm undoped GaAs buffer layer was grown on the substrate to make a smooth surface. Then a bottom DBR was formed by 4.5 periods $Al_{0.5}Ga_{0.5}As$/AlAs layers. The active layer was composed of $Al_{0.5}Ga_{0.5}As$ 30 periods (1.5 nm) MQW with undoped 1.5 nm GaAs barriers. Si-doped (Si-doping concentration: 10^{16} cm^{-3}) $Al_{0.5}Ga_{0.5}As$ layers were grown on both sides of the active layer to realize the p-n junction. And a 50 nm AlAs layer was grown on the top-side of Si-doped $Al_{0.5}Ga_{0.5}As$ layers as a high barrier. Finally, a 20 nm thick undoped GaAs cap layer was grown on the top of epilayers.

4. Isolation wet etching

After the MBE growth the devices were isolated by removing portions of the epitaxial layer and forming isolation mesas by using the photolithography and wet etching. The etching was done in H_2SO_4:H_2O_2:H_2O (1:8:8) at room temperature (R.T.) for 40 seconds.

5. Ohmic electrode fabrication

Fig. 3.5 and Fig. 3.6 are flow charts of the fabrication process of n-type and p-type ohmic electrodes on the GaAs cap layer, respectively. The lift-off technique was used to make the electrodes. First, the n-type ohmic electrodes (AuGe/Ni/Au=100 nm/30 nm/200 nm) were formed on the slopes. Next, the p-type ohmic electrodes (Zn/Au=20 nm/200 nm) were formed on the flat surfaces using photolithography and metal evaporation. These electrodes were alloyed at 400 ℃ for 60 seconds in N_2 gas.

The schematic top view and the optical microscope image of a completed device are shown in Fig. 3.7. The distance between electrodes, a, and the junction length, b, of the device are also shown in this figure.

3.2 Characterization

The electrical characteristics of the LEDs were studied by current-voltage (I-V) and capacitance-voltage (C-V) measurements, and the optical properties were studied by EL measurements. The experimental apparatus for these measurements are shown in Fig. 3.8 and 9, respectively.

3.2.1 Current-Voltage characteristics

Fig. 3.10 shows the current-voltage characteristics of the sample, at R.T. and low temperatures. The I-V characteristics at low temperatures were measured at 15 K intervals from 30 K to 300 K.

The I-V curves in Fig. 3.10 show rectifying characteristics, indicating that p-n junctions were successfully formed on the sample. They also have series resistances that decrease when the temperature is increased. The effect of a Schottky barrier at the contact between

electrodes and the GaAs materials are observed at low temperatures. Under reverse bias conditions, the reverse breakdown voltage of the sample is -28 V and the breakdown is abrupt.

The forward current in an actual diode can be represented by the form

$$I_d = I_s \exp\left(\frac{qV_d}{nkT}\right) \tag{3.1}$$

where q is the magnitude of electron charge and kT is the thermal energy. The factor n is the ideality factor of the diode and I_s is the reverse saturation current. However, an actual diode will have a series resistance R_s that contains the resistance of the semiconductor bulk material, and a shunt resistance R_{sh} that contains the resistance associated with leakage current as shown in Fig. 3.11. The forward current and voltage in the diode's junction can be represented by the following equations

$$I_d = I(V) - \frac{V_d}{R_s h} \tag{3.2}$$

$$V_d = V - IR_s \tag{3.3}$$

where $I(V)$ and V are the current and the voltage applied to the diode, respectively. The logarithm of the equation (3.2) has a linear relationship with respect to V_d. Experimental data can be fitted to this logarithmic equation by using as fitting parameters R_s and R_{sh}. The resulting values of R_s and R_{sh} obtained by this fitting procedure are shown in Fig. 3.12. Decreasing of R_{sh} and R_{sh} as the temperature increases are due to the increase of the thermally excited carrier population.

3.2.2 Capacitance-Voltage characteristics

The capacitance-voltage characteristics were measured at 30 K intervals from 30 K to 300 K. The depletion layer capacitance of an abrupt junction is given by

$$C_d = \frac{\varepsilon_s}{W} = \left[\frac{q\varepsilon_s N_B}{2(V_{bi} \pm V)}\right]^{\frac{1}{2}} \tag{3.4}$$

$$N_B = \frac{2N_A N_D}{N_A + N_D} \tag{3.5}$$

where W is the depletion layer width, ε_s is the GaAs permittivity (F/cm), V_{bi} is the built-in potential, the signs $+$ and $-$ are for the reverse and forward bias, respectively, and N_B is the reduced carrier concentration. The C^2-V characteristics of the sample have been calculated from the measured results, and curves are shown in Fig. 3.13. As the forward bias is increased, the capacitance of the sample increases due to the reduction of the depletion width. The weak temperature dependence suggests that there are not large variations in the free carrier concentration in this temperature range.

3.2.3 Electroluminescence characteristics

The visible electroluminescence (EL) spectra of a sample were observed up to R.T. The EL spectra were measured under two different applied currents to study the influence of the carrier injection. One of the applied currents was 0.2 mA and spectra were measured from 10 K to 300 K at 30 K intervals (Fig. 3.14). Two major peaks shown in Fig. 3.14 as the Peak2 and Peak3 can be observed from the spectra. Another shoulder can be observed near 1.85 eV. It is also shown in Fig. 3.14 as the Peak1. The intensity and transition energy of three peaks as a function of the temperature are shown in Fig. 3.15(a) and (b). The temperature dependence of band-to-band transition energy of GaAs was calculated using the equation

$$E_g = 1.519 - \frac{5.405 \times 10^{-4} \times T^2}{T + 204} \tag{3.6}$$

and is shown together with the experimental results in Fig. 3.15(b). From this graph it can be assumed that these peaks are related transitions occurred in the MQW. These peaks can be explained by the energy band diagram of the MQW structure at 300 K. shown in Fig. 3.16. When the applied current is 0.2 mA, QW is filled by carriers from the lowest energy state e_1 (electron1) for electrons up to the quasi fermi level (e_n) for electrons. At 300 K, the Peak1 energy coincides with the transition energy between e_1 and the $Al_{0.5}Ga_{0.5}As$ valence band. The Peak2 energy coincides with the transition energy between the e_1 and Si-acceptor level of the p-type region. These two peaks indicate that most of the EL is emitted from the p-type region. The Peak3 energy is due to the fundamental transition between the e_1 and the hh_1 (heavy hole1) for heavy holes. At low temperatures, the flat portion can be observed in Peak3 and is probably due to the presence of a two-dimensional hole gas.

The other applied current was 2.3 mA and spectra were measured from the 10 K to 300 K at 10 K $\sim$ 50 K intervals. In this condition, the similar EL spectra were obtained and two major peaks can be observed as the Peak2 and Peak3 shown in Fig. 3.17. Another weak peak can be observed near 2.0 eV as the Peak1 from the spectra. It is also shown in Fig. 3.17. The intensity and the transition energy of three peaks as a function of the temperature are shown in Fig. 3.18(a) and (b). The temperature dependence of band-to-band transition energy of GaAs is also shown together with the experimental results in Fig. 3.18(a) and (b). Fig. 3.19 shows the energy band diagram of the MQW structure with the applied current of 2.3 mA at 300 K. The Peak1 energy coincides with the transition energy between $Al_{0.5}Ga_{0.5}As$ conduction band and Si-acceptor level of the p-type region. But, the intensity of Peak1 disappears as the temperature decreases, this could imply that the carriers gain the thermal energy and are able to exist the higher energy level such as $Al_{0.5}Ga_{0.5}As$ conduction band. The Peak2 energy coincides with the transition energy between the e_1 and Si-acceptor level. The Peak3 energy is due to the fundamental transition between the e_1 and the hh_1.

Chapter 4

Lateral junction modulation doped LEDs

4.1 Fabrication

Fabrication processes were almost the same as described in Section 3.1. The MBE conditions are listed in Table 4.1. The multilayer structure shown in Fig. 4.1 was grown on GaAs(311)A patterned substrates. A 500 nm undoped GaAs layer was first grown as the buffer layer. The active layer was composed of an 8 nm $In_{0.2}Ga_{0.8}As$ SQW with undoped 5 nm GaAs barriers. Si-doped $Al_{0.3}Ga_{0.7}As$ layers were grown on both sides of the active layer (modulation doping) to realize the p-n junction. 5 nm thick Si-doped GaAs cap layer was grown on the top of the epilayers. The schematic top view and the optical microscope image of a completed device are shown in Fig. 4.2. The distance between electrodes, a, and the junction length, b, of a device are also shown in this figure.

4.2 Characterization

The electrical characteristics of LEDs were evaluated with I-V and C-V measurements. Optical properties were evaluated by EL measurements. The experimental apparatus for these measurements are the same as shown in Fig. 3.8 and 9, respectively.

4.2.1 Current-Voltage characteristics

Fig. 4.3 shows the current-voltage characteristics of the sample at R.T. and low temperatures. The I-V characteristics at low temperatures were measured at 30 K intervals from 30 K to 300 K. The I-V curves in Fig. 4.3 indicate that p-n junctions were successfully formed. They also have series resistances that decrease when the temperature is increased. The effect of a Schottky barrier at the contact between electrodes and the GaAs materials are observed at low temperatures. Under reverse bias conditions, the reverse breakdown voltage of the sample is -7.42 V.

Fig. 4.4 shows the series and shunt resistance values of the sample as a function of the temperature. The parameters R_s and R_{sh} are the same as described in Section 3.2.1. Decrease of R_s and R_{sh} as the temperature increases are due to the increase of the thermally excited carrier population.

The I-V curves after correcting the influence of R_s and R_{sh} are shown in Fig. 4.5 (a). Under forward bias a tunneling current for applied voltage lower than 1.0 V is observed in all the curves measured at several temperatures. This one indication that an abrupt p-n junction is formed. This tunneling phenomena can be observed more clearly in another sample with MBE growth temperature of 560 ℃ shown in Fig. 4.5 (b). The tunneling current in all curves does not decrease when the forward bias increases (negative differential resistance as it is usual in a tunnel diode (Esaki diode)). The reason of this phenomenon can be explained by the energy band diagram of an abrupt p-n junction with modulation doped QW shown in Fig. 4.6 (b). In this figure, a two-dimensional electron gas (2DEG) and a two-dimensional hole gas (2DHG) exist inside the QW in each side of the junction. Tunneling current is large not only when the fermi level in each side of the junction is nearly aligned. It is large as long as there is an energy overlap of the 2DEG and 2DHG. Therefore, the sum of 2DEG and 2DHG energy depth calculated from diode's structure (0.23 eV) coincides with the bias range where a large tunneling current is observed. (Fig. 4.6 (a)) Therefore, the tunneling current with a broad plateau shows the presence of a 2DEG and a 2DHG in the p-n junction.

4.2.2 Capacitance-Voltage characteristics

The capacitance-voltage characteristics of the sample measured at 300 K are shown in Fig. 4.7 (a). Fig. 4.7 (b) shows the C^2-V characteristics calculated from the measured results and its fitting curve. As the forward bias is increased, the capacitance of the sample increases due to the reduction of the depletion width.

To determine the detailed distribution of shallow level concentration near the lateral p-n junction, C^2-V characteristics of the sample is analyzed. Actually, since C^2-V values in Fig. 4.7 (b) are not proportional to the applied voltage, it can be assumed that the lateral p-n junction of the sample is graded. Data are divided at $V = -2.4$ V into a large voltage region where C^2-V is proportional to V and a small voltage region where C^2-V is not proportional to V. Capacitance values for the applied voltage smaller than (non-linear region) are plotted as C^3-V giving a fairly linear fit shown in Fig. 4.8 (a). Fig. 4.8 (b) shows C^2-V a fairly linear fitting characteristics of capacitance values for the applied voltage larger than $V = -2.4$ V (linear region). This result indicates that shallow level concentration is graded in the range of the applied voltage smaller than $V = -2.4$ V. The graded region has a thickness of about 39.7 nm.

4.2.3 Electroluminescence characteristics

Near infrared EL spectra were obtained from a sample measured at 30 K intervals from 10 K to 300 K for an applied current of 2.0 mA shown in Fig. 4.9. Two major peaks and a

weak peak can be observed from the spectra shown in Fig. 4.9 as Peak1, Peak2 and Peak3. We assume that Peak1 is related to the e_1-hh_1 transition and shows a plateau that extends to higher energies. Peak2 is related to the e_2-hh_2 transition and Peak3 coincides with the GaAs bandgap energy.

To observe more clearly the shape of Peak1, the fitting curves of Peak2 are removed from all EL spectra as shown in Fig. 4.10. The width of the plateau of Peak1 is nearly independent of measurement temperatures. The shape and position of Peak1 and Peak2 can be explained by the density states diagram of a p-type modulation doped SQW structure shown in Fig. 4.11. In this figure e_1, e_2 and e_3 are the energy levels for electrons in the conduction band QW and hh_1, hh_2 and hh_3 are energy levels for heavy holes in the valence band QW. The heavy hole levels are filled from hh_1 up to the quasi fermi level E_{fp}, accordingly to the hole density for this sample shown in Table 4.1. At 300 K, the left shoulder of Peak1 energy coincides with the fundamental transition energy between e_1 and hh_1 (1.27 eV). The difference in energy between hh_1 and E_{fp} is 42.3 meV and it coincides with the width of the plateau of Peak1. This is a clear indication of the presence of a 2DHG in the p-type region. Peak2 coincides with the transition energy between e_2 and hh_2 (1.37 eV). This experiment is an original and elegant method to identify and characterize a 2DHG in the lateral junction.

Chapter 5

Vertical-cavity surface-emitting lasers

5.1 Principle of VCSELs

VCSELs are generating intense interest as a light source for optical systems. Their advantages include simple integration into 2-D arrays, on-wafer testing, and optical disk memories, as well as efficient optical fiber coupling [16]. In this section I briefly discuss the some anticipated characteristics of VCSELs. I also briefly discuss the comparison between conventional QW laser diodes and lateral junction QW laser diodes.

5.1.1 Threshold current and quantum efficiency

The schematic structure of a VCSEL is shown in Fig. 5.1. A circular buried heterostructure in which the active region is buried in a material with smaller bandgap energy is considered. And injected carriers are completely confined in the circular active region with diameter D. The optical loss for the resonant mode must balance the gain to reach the threshold. That is

$$g_{th} = \alpha_{ac} + \alpha_{ex}\left(\frac{1}{\xi} - 1\right) + \frac{1}{\xi d}\ln\left(\frac{1}{R_f R_r}\right) + \alpha_d \tag{5.1}$$

Where g_{th} is the threshold gain, d is the active layer thickness, L is the cavity length, α_{ac} and α_{ex} are the absorption loss in the active and cladding layers, respectively, R_f and R_r are the reflective of the front and rear side reflector, and α_d is the diffraction loss. ξ is the energy confinement factor, which is expressed as the product of the longuituditional confinement factor ξ_l and the transverse factor ξ_t as

$$\xi = \xi_l \cdot \xi_t \tag{5.2}$$

ξ_l is expected as

$$\xi_l = \gamma d/L \tag{5.3}$$

When a very thin active layer (~100Å) is placed at the maxima of standing wave, γ equals two, and it is unity for a thick active layer. The concept of reducing the threshold by placing the active layer at the maxima which is called *periodic gain structure* is suggested.

If I assume that $\alpha_{ac} = 10$ cm^{-1}, $\alpha_{ex} = 10$ cm^{-1}, $\alpha_d = 10$ cm^{-1}, $L = 7$ μm, $d = 3$ μm and $g_{th} = 200$ cm^{-1} in Eq. (5.1), the necessary average reflectivity must be

$$\sqrt{R_f R_r} = 0.95 \tag{5.4}$$

The threshold gain is expressed in terms of the threshold carrier density N_{th} as

$$g_{th} = A_0 N_{th} - \alpha_{in} \tag{5.5}$$

where α_{in} is the residual absorption loss, and A_0 is the gain coefficient. Thus, the threshold carrier density N_{th} is expressed as

$$N_{th} = \frac{g_{th} + \alpha_{in}}{A_0} \tag{5.6}$$

If I put $g_{th} = 200$ cm^{-1}, $\alpha_{in} = 400$ cm^{-1} and $A_0 = 3 \times 10^{-16}$ cm^2 for the AlGaAs/GaAs system, $N_{th} = 2 \times 10^{18}$ cm^{-3}. The threshold current density of the surface-emitting laser is then expressed as

$$J_{th} = \frac{N_{th}}{\tau_s} = \frac{edB_{eff}}{A_0^2}\left(\alpha_{ac} + \alpha_{in} - \alpha_{ex} + \frac{L}{d}\alpha_{ex} + \frac{1}{2d}\ln\left(\frac{1}{R_f R_r}\right) + \alpha_d\right)^2 \tag{5.7}$$

where τ_s is a carrier lifetime, e is electron charge and B_{eff} is the effective recombination constant. Here we have used the following relationship:

$$\tau_s = \frac{1}{B_{eff} N_{th}} \tag{5.8}$$

If there is no guiding structure in a cladding layer of a device, it results in a divergence of a resonant beam. This causes a diffraction loss, which limits thinning of the diameter to maintain a small diffraction. Assuming that the transverse field distribution loss, α_d is expressed as follows

$$\alpha_d = \frac{1}{d}\ln\left(\frac{1}{2 + 3(2l_c/ks^2)^2 + (2l_c/Ks^2)^4}\right) \tag{5.9}$$

where l_c is the cladding layer thickness, and k is the propagation constant. The reduction of a resonant beam, causing a large increase in the diffraction loss α_d.

Figure 5.2 (a) shows a calculated threshold current density of a AlGaAs/GaAs surface-emitting laser against active layer thickness without taking a diffraction loss into account. When $R = 95$ % and $d = 2$-3 μm, the threshold current density J_{th} is 25 to approximately 30 kA/cm^2. This value is the same as that of high-radiance LEDs and is not a suprisingly

high level. The increase of reflectivity can provide further reduction of the threshold current density. A similar result is obtained for a InGaAsP/InP surface-emitting laser ($\lambda_g = 1.3$ μm) as shown in Fig. 5.2 (b). We can find that the threshold current density can be reduced to less than 10 kA/cm^2 by increasing the reflectivity to 99 % This may be achievable by employing a suitably controlled dielectric or semiconductor multilayer reflector. In addition, a quantum well structure can provide a lower threshold by 40 %. By reducing the active layer thickness to 100 Å and increasing the reflectivity to 99.9 %, a threshold current density of less than 1 kA/cm^2 can be expected. Fig. 5.3 shows a calculated threshold current density and threshold current against the diameter of the active region in a AlGaAs/GaAs surface-emitting laser, in which the spot diameter $2s$ is assumed to be equal to the active region diameter D. When the diameter is more than 3 μm, the diffraction loss is negligibly small. Therefore, the threshold current can be decreased in proportion to the square of the diameter in this region. The threshold current is a minimum in the range of the diameter from 1 to 2 μm.

Also, we consider the differential quantum efficiency of the surface-emitting laser. If we use a non-absorbing mirror for the front mirror, the differential quantum efficiency from the front mirror is expressed as

$$\eta_d = \eta_i \frac{\ln(1/R_f)}{2\alpha L + \ln(1/R_f R_t)} \tag{5.10}$$

where η_i is the internal quantum efficiency and α is the internal loss. A calculated result for the AlGaAs/GaAs surface-emitting laser is shown in Fig. 5.4, in which a dielectric multilayer reflector and Au-coated reflector are considered for the front mirror. We have assumed that $R_r = 1.0$ and the internal quantum efficiency $\eta_i = 1$. As for the Au-coated mirror, efficiency deteriorates due to the differential quantum efficiency stays at 40 % because of its short cavity structure.[16]

5.1.2 Lateral junction VCSELs

The intrinsic limitation of modulation speed in QW laser diodes is given by the electron relaxation time from the 3-dimensional laser cavity into the 2-dimensional QW.[17] Holes relax much faster than electrons, and so do not limit modulation speed. Experimental results indicate that this electron relaxation time is between 3 and 15 ps.[18] Therefore, the maximum modulation bandwidth that conventional QW laser diodes could reach is roughly between 60 and 300 Ghz. Tunneling injection of electrons into the QW has been proposed as a solution to increase the modulation bandwidth.[17] Electron relaxation time from the cladding layer into the 3-dimensional laser cavity is about 1 or 2 ps, and drift/diffusion time in the laser cavity is below 0.75 ps.[18] These short times do not greatly influence the modulation speed of conventional QW laser diodes.

Electrons in lateral junction QW laser diodes are already inside the QW in the n-type region, outside the p-n junction depletion layer. Therefore, the relaxation time from the 3-ddimensional laser cavity into the 2-dimensional QW and the relaxation time from the cladding layer into the 3-dimensional laser cavity are eliminated. Only the drift/diffusion

time (< 0.75 ps) remains. In this case, the modulation bandwidth of the lateral junction QW laser diodes can be greatly enhanced. Moreover, the applied bias required to inject a given current can be reduced and the power efficiency of the device would improve. The lateral junction area can be made orders of magnitude smaller as compared to vertical junctions, with the consequent reduction of the device capacitance. This p-n junction can be used for making vertical cavity as well as edge-emitting laser diodes.[7]

5.2 Fabrication

Substrate patterning was the same as described in section 3.2. MBE growth conditions are listed in Table 5.1. The multilayer structure shown in Fig. 5.4 was grown on patterned substrates. The active layer is $In_{0.2}Ga_{0.8}As$ 5 periods MQW with non-doped GaAs barriers. There are Si-doped GaAs layers between QWs to make the p-n junction. The bottom and top DBRs are formed by 4 and 3 periods of $AlAs/Al_{0.5}Ga_{0.5}As$ layers, respectively. AlAs layer thickness was calculated to have one-fourth laser emission wavelength ($\lambda \sim 970$ nm) after oxidation (Al-oxide's refractive index 1.55) and including a 13 % contraction that was previously measured in other samples. There are $Al_{0.5}Ga_{0.5}As$ layers on both sides of the cavity (3 λ) as a spacer layer. A 30 nm GaAs cap layer was grown on the top of epilayers.

After MBE growth the devices were isolated to 10 μm and 20 μm square mesas by using isolation wet etching process the same as described in section 3.1. Mesas with one edge near the (100)-oriented slope were made by wet etching, to expose the edges of the AlAs layers. The AlAs layers were oxidized at 400 ℃ in a flowing nitrogen atmosphere saturated with water vapor (wet oxidation process) to form the high-reflectivity DBRs. A schematic drawing of the wet oxidation system is shown in Fig. 5.5. Figure 5.6 shows the schematic top view and the microscope image of the completed device. The high reflectance required for the DBRs is obtained using just a few periods due to the large difference of refractive index between the $Al_{0.5}Ga_{0.5}As$ and the oxidized AlAs (Al-oxide) layers. This structure design of the VCSEL was optimized at room temperature.

5.3 VCSEL luminescence dependence on DBR oxidation conditions

Epitaxially grown oxide/semiconductor DBRs formed by wet thermal oxidation have been used to fabricate VCSELs.[19][20][21][22] The AlAs in an AlAs/GaAs multilayer stack is selectively oxidized to form a very low index material, useful for high-contrast DBRs.[20][23][24][25] The differences in the indexes between these materials are large, and the DBRs have a high reflectivity and a wide bandwidth.[16] The cavity resonance peak wavelength of DBRs can be adjusted by oxidation conditions. In this section I study how the oxidation conditions affect the spectral reflectance of the DBR.

5.3.1 Wet oxidation

Al-oxide layers are formed by wet thermal oxidation of AlAs through chemical reaction in a nitrogen and water vapor atmosphere. The expected reaction is represented by the following chemical formula [26][27].

$$2AlAs + 3H_2O \rightarrow Al_2O_3 + 2AsH_3 \tag{5.11}$$

The equation shows that two molecules of AlAs react to form one molecule of Al-oxide. The volume per "molecule" of AlAs, crystallized in a zinc blended structure (lattice constant of 5.662 Å) is 45.4 Å^3. On the other hand, Al-oxide in the γ-phase, crystallized with a cubic Fd3m spinel-like structure, consisting of 32 atoms of oxygen, $21\frac{1}{3}$ atoms of Al, and 2 $\frac{2}{3}$ vacancies per unit cube, has a cube edge of 7.9 Å. This coincides with a volume of 46.2 Å^3 per molecule of Al-oxide. Therefore, the reaction given by Eq. (5.11) implies a shrinkage of about 50% (by volume) in the AlAs layer if it is converted to compact $\gamma-$Al-oxide.

5.3.2 Optical reflectivity of multilayer structures

The reflectivity and transmissivity of a series of slabs of $Al_xGa_{1-x}As$ with x between 0 and 1, separated by abrupt plane boundaries, can be calculated using the transefer-matrix method. Fig. 5.7 shows the incident, reflected and transmitted light in one slab of material "1" with thickness d between slabs of materials "0" and "2". Since the tangential components of the electric and magnetic fields pararell to the boundaries are continuous can be equated at each interface "a" and "b", and characteristic matrix for each layer is obtained:

$$\begin{pmatrix} E_a \\ H_a \end{pmatrix} = \begin{pmatrix} \cos\delta_1 & i \cdot \sin\delta_1/y_1 \\ i \cdot \sin\delta_1/y_1 & \cos\delta_1 \end{pmatrix} \begin{pmatrix} E_b \\ H_b \end{pmatrix} \tag{5.12}$$

where $y_1 = n_1 - i \cdot k_1$ is the optical admittance and $\delta_1 = 2\pi y_1 d_1/\lambda_{light}$. The results can be extended to n-layers, and after rearrangement, the following equation is obtained:

$$\begin{pmatrix} B \\ C \end{pmatrix} = \prod_{j=1}^{n} \left(\begin{pmatrix} \cos\delta_1 & i \cdot \sin\delta_1/y_j \\ i \cdot \sin\delta_1/y_j & \cos\delta_j \end{pmatrix} \right) \begin{pmatrix} 1 \\ y_{sub} \end{pmatrix} \tag{5.13}$$

where $B = E_a/E_b$, $C = H_a/E_b$, and y_{sub} is the substrate's optical admittance. The reflection coefficient is calculated as:

$$R = \frac{(y_0 B - C)(y_0 B - C)}{(y_0 B + C)(y_0 B + C)} \tag{5.14}$$

where y_0 is the optical admittance of the incidence media (typically, it is air).

The transmission coefficient is calculated as:

$$T = \frac{4 y_0 Re(y_{sub})}{(y_0 B + C)(y_0 B + C)} \tag{5.15}$$

A multi-layer structure can be characterized by the PL measurement and comparison with a simulated spectrum based on this theory.

5.3.3 Optical reflectivity dependence on DBR oxidation conditions

An oxidation model of AlAs/$Al_{0.5}Ga_{0.5}As$ DBRs is proposed to investigate the influence of DBR oxidation conditions for its optical reflectivity. The $Al_{0.5}Ga_{0.5}As$ layer inserted between two AlAs layers partially oxidizes in the vertical direction as shown in Fig. 5.8. The oxidation rate of the $Al_{0.5}Ga_{0.5}As$ layer is much lower and the AlAs layer completely oxidizes before any significant oxidation of the $Al_{0.5}Ga_{0.5}As$ occurs. The oxidized AlAs layer supplies the $Al_{0.5}Ga_{0.5}As$ layer with the reactants so that it oxidizes in the growth direction.

I calculated the optical reflectivity of the VCSEL with the several oxidation conditions of DBR using the transfer-matrix method mentioned in Section 5.3.2. Fig. 5.9 shows the calculated reflectance spectrum of the 3 λ -cavity VCSEL described in the previous section as the AlAs layer's oxidation completed. In this figure three major resonance peaks can be observed as long wavelength peak (1144 nm), center wavelength peak (995 nm) and short wavelength peak (891 nm). The stop band with the reflectance of 99.992 % is also observed. Fig. 5.10 shows the reflectance spectra dependence on an $Al_{0.5}Ga_{0.5}As$ oxidized layer width of each peak at 5 nm oxidation intervals from non-oxidation up to oxidation completed. The long wavelength peak and the center wavelength peak shift to shorter wavelengths as the oxidation width of $Al_{0.5}Ga_{0.5}As$ layers increased. This shift cannot observed in the short wavelength peak spectra due to the GaAs absorption. This shift is due to the difference of the reflective index of materials. The refractive index of the semiconductor is much greater than that of the oxide, the thickness change of the semiconductor has a proportionally greater influence over the wavelength shift of the DBR than the thickness change of the oxide. Since the semiconductor is consumed and becoming thinner, the resonance peak shifts to shorter wavelength.

The wavelength, resonance depth and full-width at half-maximum (FWHM) of three peaks and the stop band reflectance as a function of the oxidation width of $Al_{0.5}Ga_{0.5}As$ layers are shown in Fig. 5.11. From these graphs the resonance peak wavelength can be controlled with good characteristics up to the $Al_{0.5}Ga_{0.5}As$ oxidation width of 30 nm. Therefore, we can obtain the centered wavelength of the VCSEL's cavity ($\lambda \sim 970$ nm) with the $Al_{0.5}Ga_{0.5}As$ oxidation width of 15 nm.

Fig. 5.12 (a) shows the PL spectra from the cavity of samples oxidized at 400 ℃ for 10 min., 20min., and 40 min. The PL was excited with a He-Ne laser (633 nm). The peak shifts to the shorter wavelengths as the oxidation time increases. This means that $Al_{0.5}Ga_{0.5}As$ layers were consumed and becoming thinner. Fig. 5.12 (b) shows the PL spectra from the cavity of samples oxidized at 400 ℃, 440 ℃, and 480 ℃ for 10 min. The peak shifts to the short wavelength stronger than the previous one. In each graphs, the light intensity of peaks decreases drastically near the wavelength of 970 nm. This is due to the sensitivity of the monochromator's detector. Therefore, a 30 nm shift to shorter

wavelengths is observed with the oxidation temperature of 480 ℃ and time of 10 min. The optical microscope images of samples are shown in Fig. 5.13. As shown in this figure, the DBR's color of all the samples are different and this indicates the DBR's reflectivity was changed by reducing the thickness of $Al_{0.5}Ga_{0.5}As$ layers. The cracked DBR was observed in the sample with the oxidation temperature of 480 ℃. For the reason that it is necessary to transport H_2O molecules inward and AsH_3 gas outward in the oxidation process. When the oxidation temperature is high, the reaction rate is larger than the transport rate. Then the AsH_3 gas remains inward of the mesas and large strain is generated. When the surface cannot endure this strain, it grooves and the AsH_3 gas emitted from this groove.

5.4 Photoluminescence characteristics

A lateral junction VCSEL oxidized at 400 ℃ for 10 min. was prepared for optical pumping. These oxidation conditions were chosen based on results of Section 5.3.3. PL measurement was performed by using a Ti-sapphire laser (710 nm) excited with an Ar^+ laser under continuous wave (CW) conditions.

Fig. 5.14 compares the active-layer photoluminescence spectrum (a), measured before oxidizing the AlAs layers of the DBRs, and measured after oxidizing DBRs (b). The spectrum (a) is the spontaneous light emission from QWs because DBRs has low reflectivity. After oxidizing, high reflectivity DBRs are formed, the spectrum (b) shows the light emission affected by the cavity-resonance. Fig. 5.15 also shows PL spectra with (a), excitation laser power of 60.6 mW, and 0.63 mW (b). From the shape of spectra and the narrowing the line width, we can observe onset of amplified spontaneous emission with excitation laser power of 60.6 mW. The PL peak wavelength shows good matching with the structure design. Fig. 5.16 shows the PL peak intensity dependence on excitation laser power and Fig. 5.17 shows the line width of spectra dependence on excitation laser power. From these graphs, the amplified spontaneous emission is observed with very low excitation laser power.

PL spectra dependence on the measured temperature from 225 K to 275 K are shown in Fig. 5.18. The peak wavelength shifts to shorter wavelengths as temperature decreases due to the increase of energy bandgap. The tail of the peak could be related to variations of thickness or composition near the edge of the mesa. The peak light intensity as a function of temperature are shown in Fig. 5.19. From this graph, the good matching between spontaneous-light-emission peak wavelength and cavity-resonance peak wavelength is observed at 260 K.

This lateral junction VCSEL is expected to obtain laser operation by electrical injection. This device has the advantage of being grown on a semi-insulating substrate, that facilitates the fabrication of arrays and integrated circuits with coplanar contacts. Besides, it has a total thickness of 2.75 μm, that is much smaller than conventional designs due to the use of oxidized AlAs DBRs, reducing epitaxial growth time and simplifying device processing.

Chapter 6

Conclusions

Two types of lateral junction LEDs and a lateral junction VCSEL were fabricated and measured. The lateral junctions were fabricated with Si-doped GaAs epilayers grown by molecular beam epitaxy (MBE) on GaAs (311)A-oriented patterned substrates. Each device takes advantage of the peculiarities of the lateral junction. LEDs have a light-emitting region unobstructed by contacts.

The visible EL spectra observed from the GaAs/$Al_{0.5}Ga_{0.5}As$ 30 periods MQW structure up to room temperature and most of EL was emitted from the p-type region.

Peculiar near infrared EL spectra where observed from the $In_{0.2}Ga_{0.8}As$/GaAs SQW structure with non-doped GaAs barriers up to room temperature. In the EL spectra a plateau that is nearly independent of measurement temperatures shows the presence of a 2DHG in the p-type region. This EL measurement is an original and elegant method to identify and characterize a 2DHG in the lateral junction.

The optically-pumped lateral junction VCSEL with an active layer composed of 5 $In_{0.2}Ga_{0.8}As$/GaAs QWs and non-doped GaAs barriers has electrically insulating distributed Bragg reflectors that simplifies device processing. The cavity-resonance wavelength can be tuned over a 30 nm range of wavelength by progressive oxidation of the AlGaAs layers in the Al-oxide/AlGaAs DBRs. The amplified spontaneous emission was obtained with very low excitation laser power of 60.6 mW. This lateral junction VCSEL shows the best overlap between the spontaneous light emission peak wavelength and cavity-resonance peak wavelength at 260 K.

Further investigation on the lateral junction VCSEL is required to obtain laser operation by electrical injection. The use of a lateral p-n junction will allow the direct injection of electrons and holes into the active layer, and is expected to improve the high frequency characteristics of the semiconductor laser diode.

Acknowledgement

This research was done at the ATR Adaptive Communications Research Laboratory, Department 4 (ATR-ACRL) from April 1, 1999 to March 31, 2001. I would like to express my sincere gratitude to Prof. Pablo O. Vaccaro for his excellent guidance throughout this work. I would also like to thank Dr. Bokuji Komiyama (ACRL president), Dr. Tahito Aida (Department4 chief) and other researchers in ATR for their valuable discussions during this research.

I am deeply thankful to Prof. Akira Sugimura for his continuous encouragement and giving me this research opportunity. I would like to thank Prof. Hiroaki Ando for his valuable discussions throughout this research and critical reading of the manuscript.

Finally, I wish especially to thank my girlfriend Maiko for her assistance in many ways.

Bibliography

[1] S. Morin, B. Devaud, F. Clerot, K. Fujiwara and K. Mitsunaga, IEEE J. Quantum Electron. **27**, 1669 (1991)

[2] W. Rideout, W. F. Sharfin, E. S. Koteles, M. O. Vassell and B. Elman, IEEE Photon. Tech. Lett. **3**, 784 (1991)

[3] J. M. Ballingall and C. E. C. Wood, Appl. Phys. Lett. **41**, 947 (1982)

[4] W. I. Wang, E. E. Mendez, T. S. Kuan and L. Esaki, Appl. Phys. Lett. **47**, 826 (1985)

[5] M. Inai, T. Yamamoto, M. Fujii, T. Takebe and K. Kobayashi, Jpn. J. Appl. phys. **32**, 523 (1993)

[6] H. Ohnishi, M. Hirai, K. Fujita and T. Watanabe, Jpn. J. Appl. Phys. **35**, 1168 (1996)

[7] P. O. Vaccaro, H. Ohnishi and K. Fujita, Appl. Phys. Lett. **74**, 3854 (1999)

[8] C. Kittel, Introduction to Solid State Physics sixth edition, John Wiley and Sons, Inc., ch.19 (1986)

[9] S. M. Sze, Physics of Semiconductor Devices second edition, A Wiley-Interscience publication, ch.12 (1981)

[10] M. Shigeta, Y. Okano, H. Seto, H. Katahana, S. Nishine and K. Kobayashi, J. Cryst. Growth. **111**, 248 (1991)

[11] K. Fujita and P. O. Vaccaro, Current Topics in Cryst. Growth. Res. **3**, (1997)

[12] T. Takatori, T. Fukunaga, J. Kobayashi, K. Ishida and H. Nakashima, Jpn. J Appl. Phys. **26**, 1097 (1987)

[13] T. Ohachi, J. M. Feng, K. Asai, M. Uwani, M. Takeuchi, P. O. Vaccaro and K. Fujita, Microelectron. J. **30**, 471 (1999)

[14] T. Ohachi, J. M. Feng, K. Asai, M. Uwani, M. Takeuchi, P. O. Vaccaro and K. Fujita, J. Cyst. Growth. **201**, 226 (1999)

[15] J. M. Feng, M. Takeuchi, K. Asai, M. Uwani, P. O. Vaccaro, K. Fujita and T. Ohachi, Microelectron. J. **30**, 433 (1999)

[16] G. A. Evans and J. M. Hammer, Surface Emitting Semiconductor Lasers and Arrays, Academic press, Inc., ch.3 (1993)

[17] H. C. Sun, L. Davis, S. Sethi, J. Singh and P. Bhattacharya, IEEE Photon. Tech. Lett. **5**, 870 (1993)

[18] W. Rideout, W. Sharfin, E. Koteles, M. Vassell and B. Elman, IEEE Photon. Tech. Lett. **3**, 784 (1991)

[19] M. H. MacDougal, P. D. Dupkus, V. Pudikov, H. Zhao and G. M. Yang, IEEE Photon. Tech. Lett. **7**, 229 (1995)

[20] M. J. Ries, T. A. Richard, S. A. Maranowski, N. Holonyak, Jr. and E. I. Chen, Appl. Phys. Lett. **65**, 740 (1994)

[21] H. Deng, D. L. Huffaker, J. Shin and D. G. Deppe, Electron. Lett. **31**, 278 (1995)

[22] M. H. MacDougal, G. M. Yang, A. E. Bond, C. K. Lin, D. Tishinin and P. D. Dupkus, IEEE Photon. Tech. Lett. **8**, 310 (1996).

[23] M. H. MacDougal, H. Zhao, P. D. Dupkus, M. Ziari and W. H. Steier, Electrom. Lett. **30**, 1147 (1994).

[24] M. H. MacDougal, S. G. Hummel, P. D. Dupkus, H. Zhao and Y. Cheng, IEEE Photon. Tech. Lett. **7**, 385 (1995).

[25] S. G. Hummel, M. H. MacDougal and P. D. Dupkus, Electrom. Lett. **31**, 972 (1995).

[26] S. Guha, F. Agashi, B. Pezeshki, J. A. Kash, D. W. Kisker and N. A. Bojarczuk, Appl. Phys. Lett. **68**, 906 (1996).

[27] R. D. Twesten, D. M. Follstaedt, K. D. Choquette, R. P. Schneider, Jr., Appl. Phys. Lett. **69**, 19 (1996).

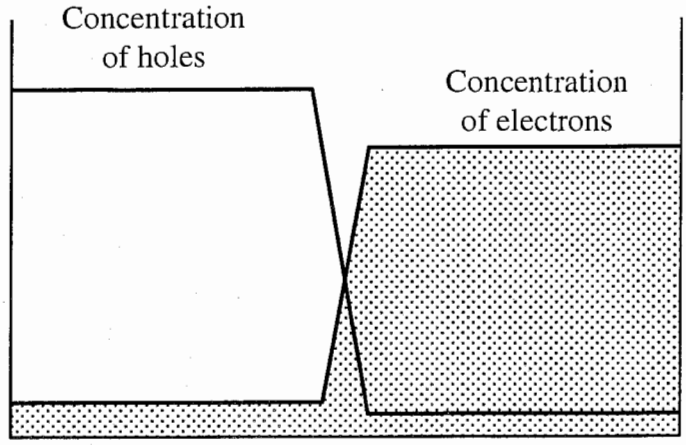

(a)

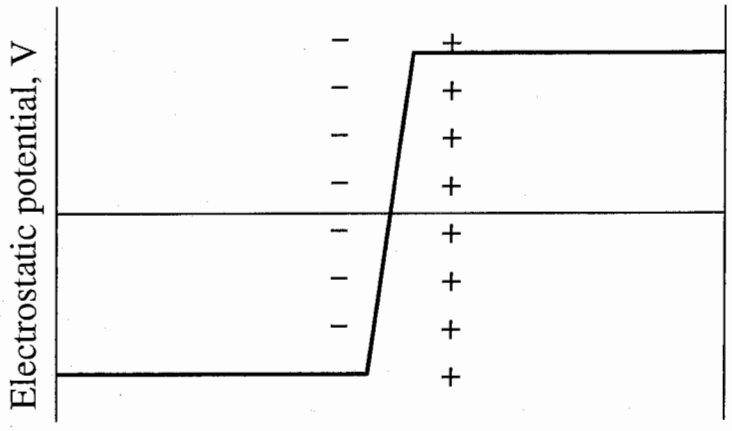

(b)

Fig. 2.1 (a) Variation of the hole and electron concentrations across unbiased junction
(b) Electrostatic potential from acceptor (-) and donor (+) ions near the junction

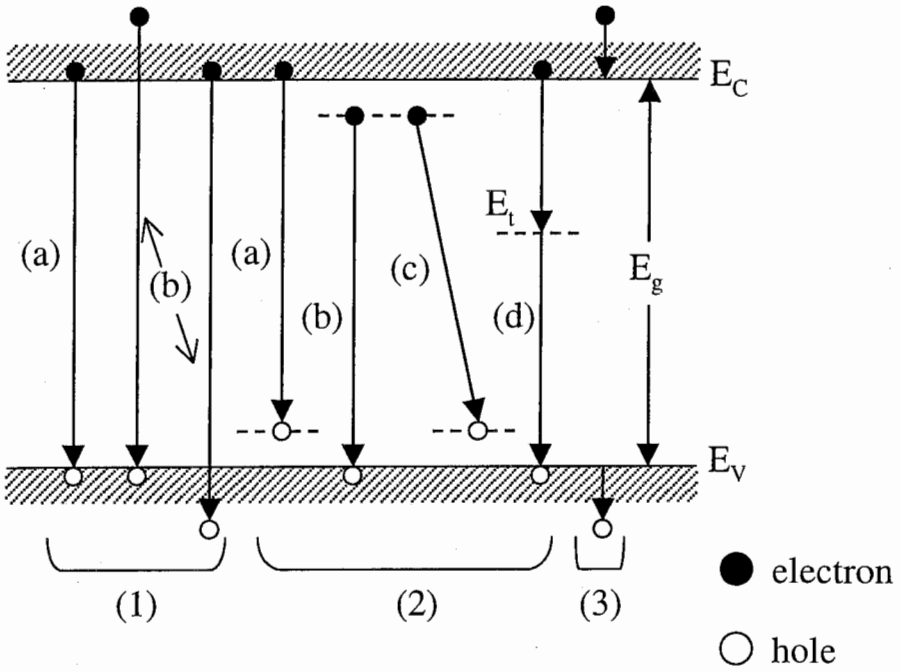

Fig. 2.2 Basic electronic transitions in a semiconductor

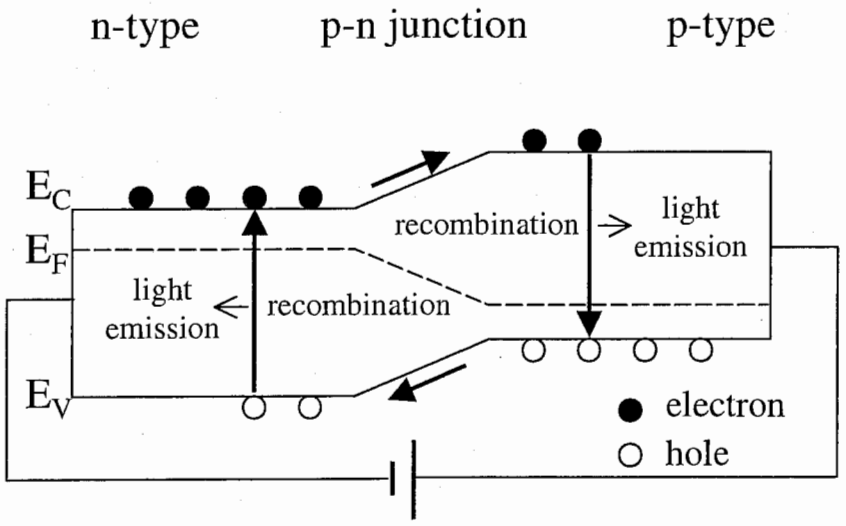

Fig. 2.3 Schematic energy band diagram of a LED in operation

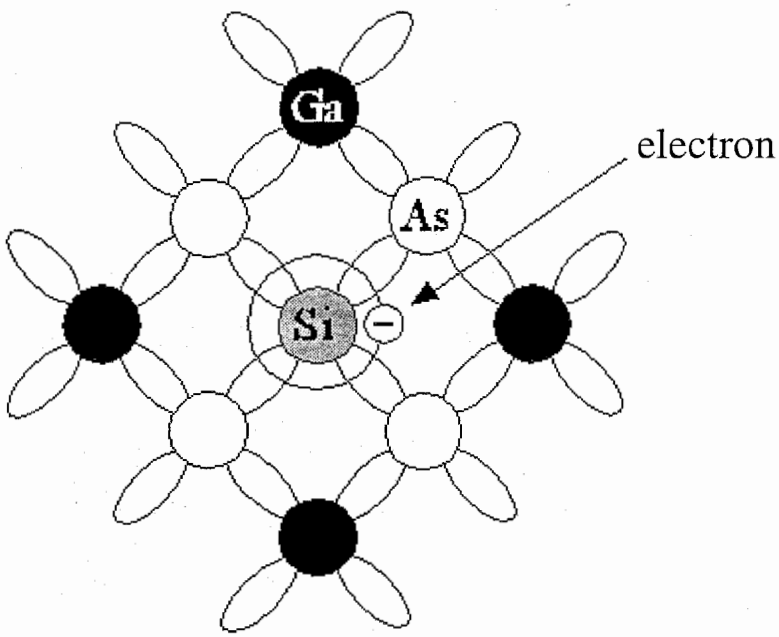

(a) n-type GaAs with Si in Ga site

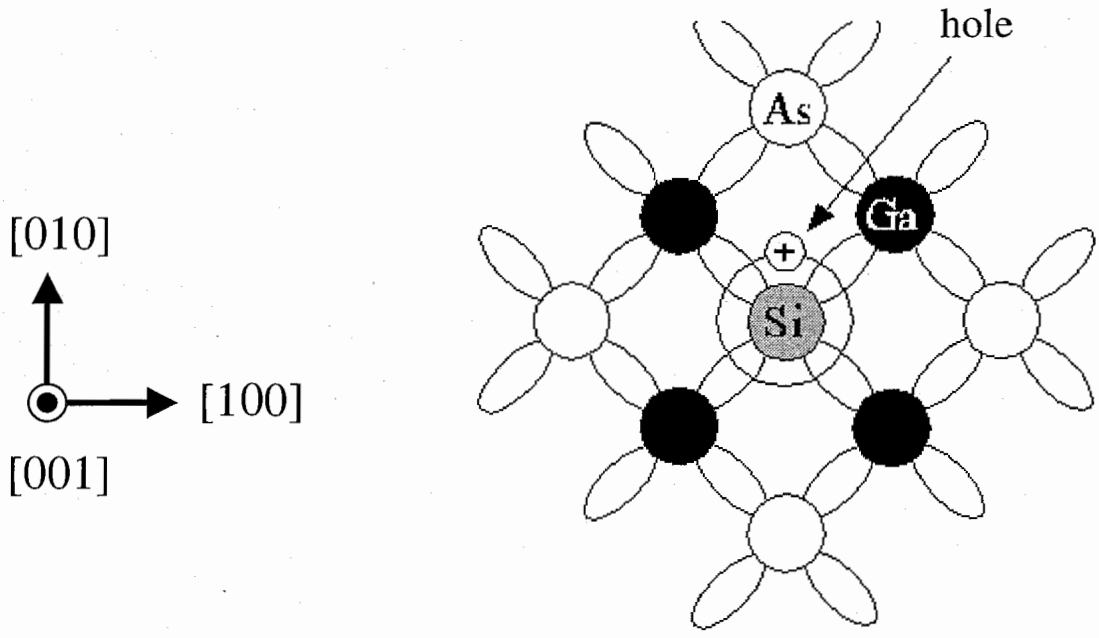

(b) p-type GaAs with Si in As site

Fig. 2.4 Schematic bond pictures of GaAs with Si-doping

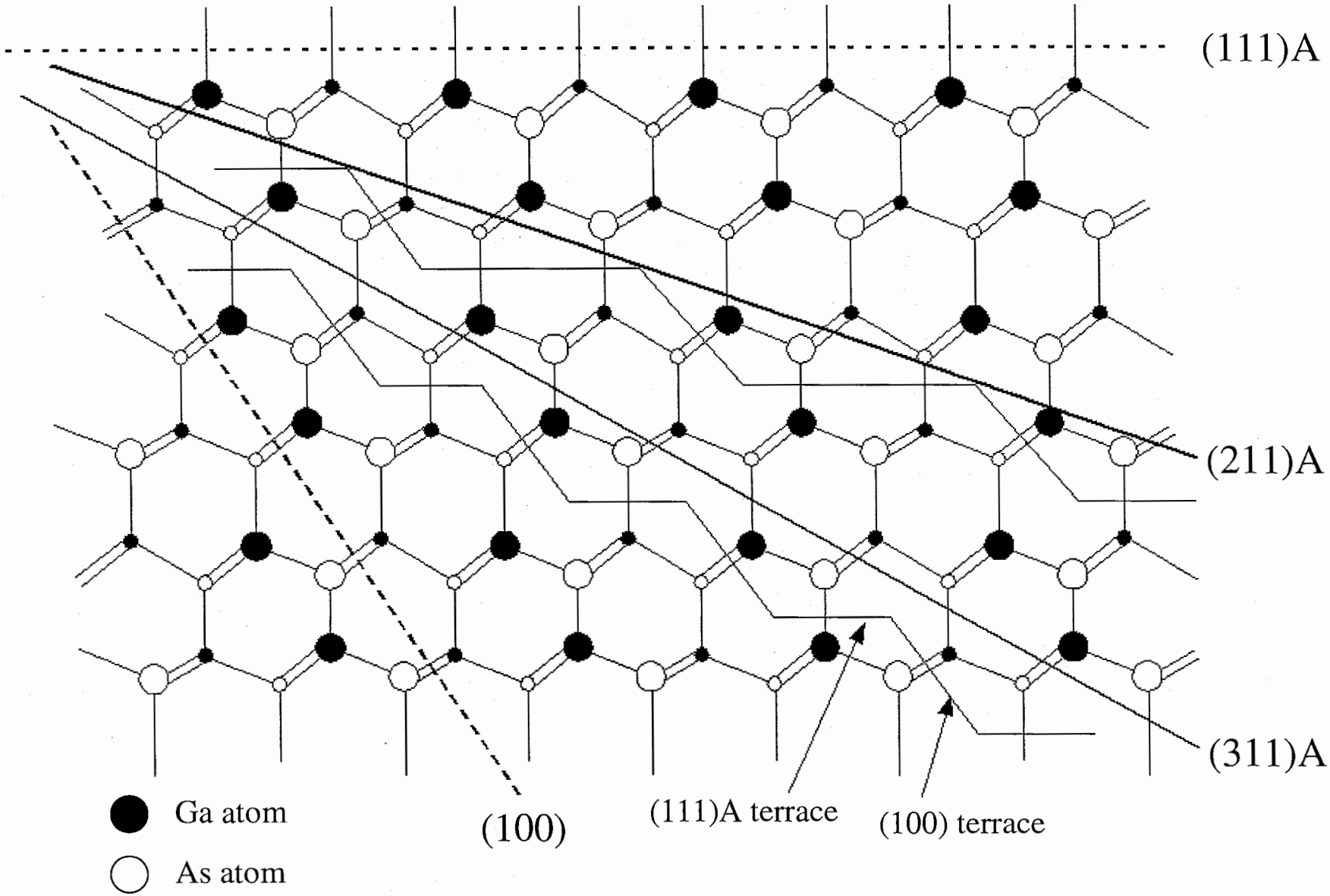

Fig. 2.5 Sectional view of the ideal atomic structure of GaAs

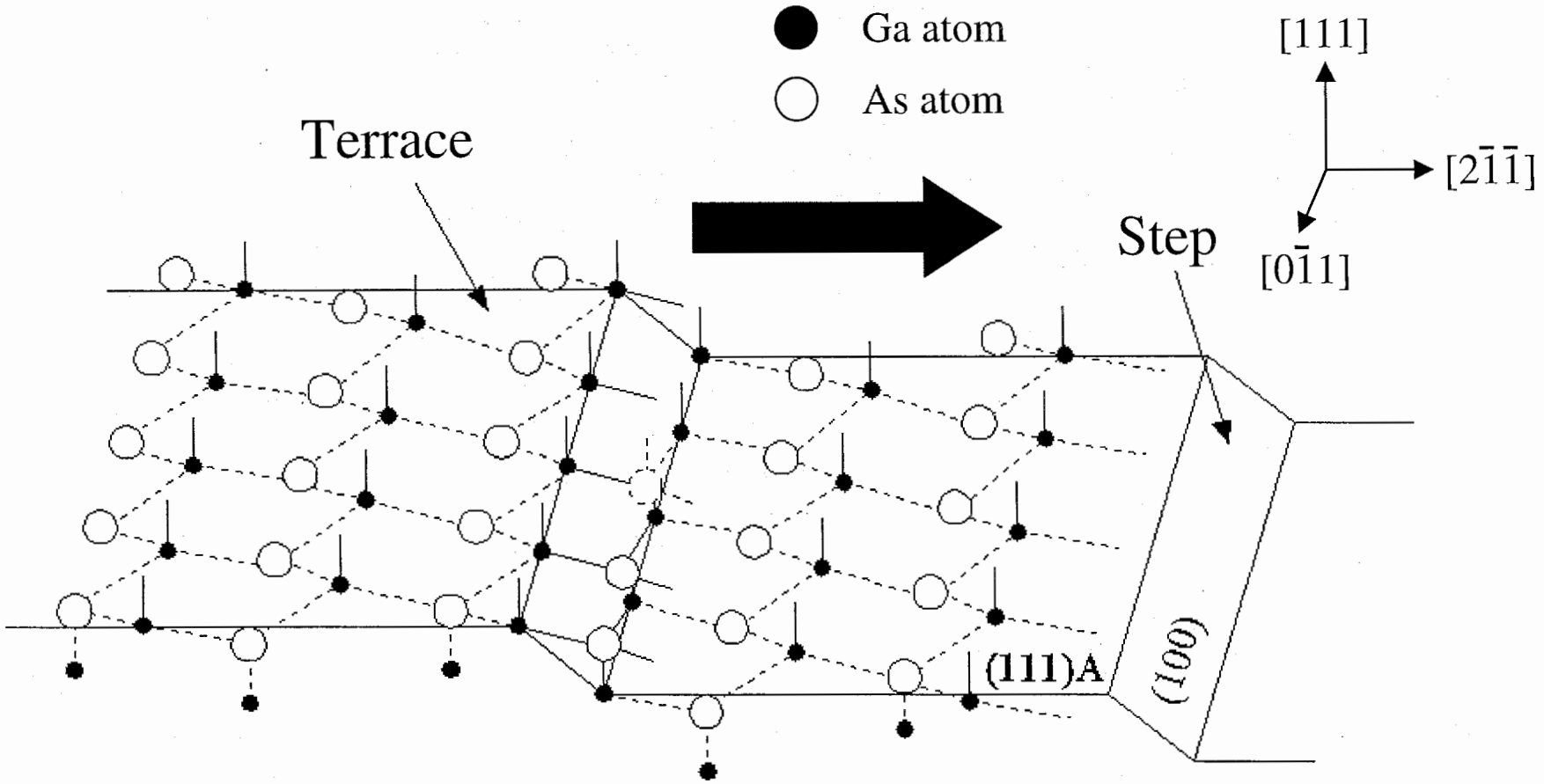

Fig. 2.6 Crystallographic scheme of an ideal misoriented GaAs (111)A surface, showing kinds of bonding sites

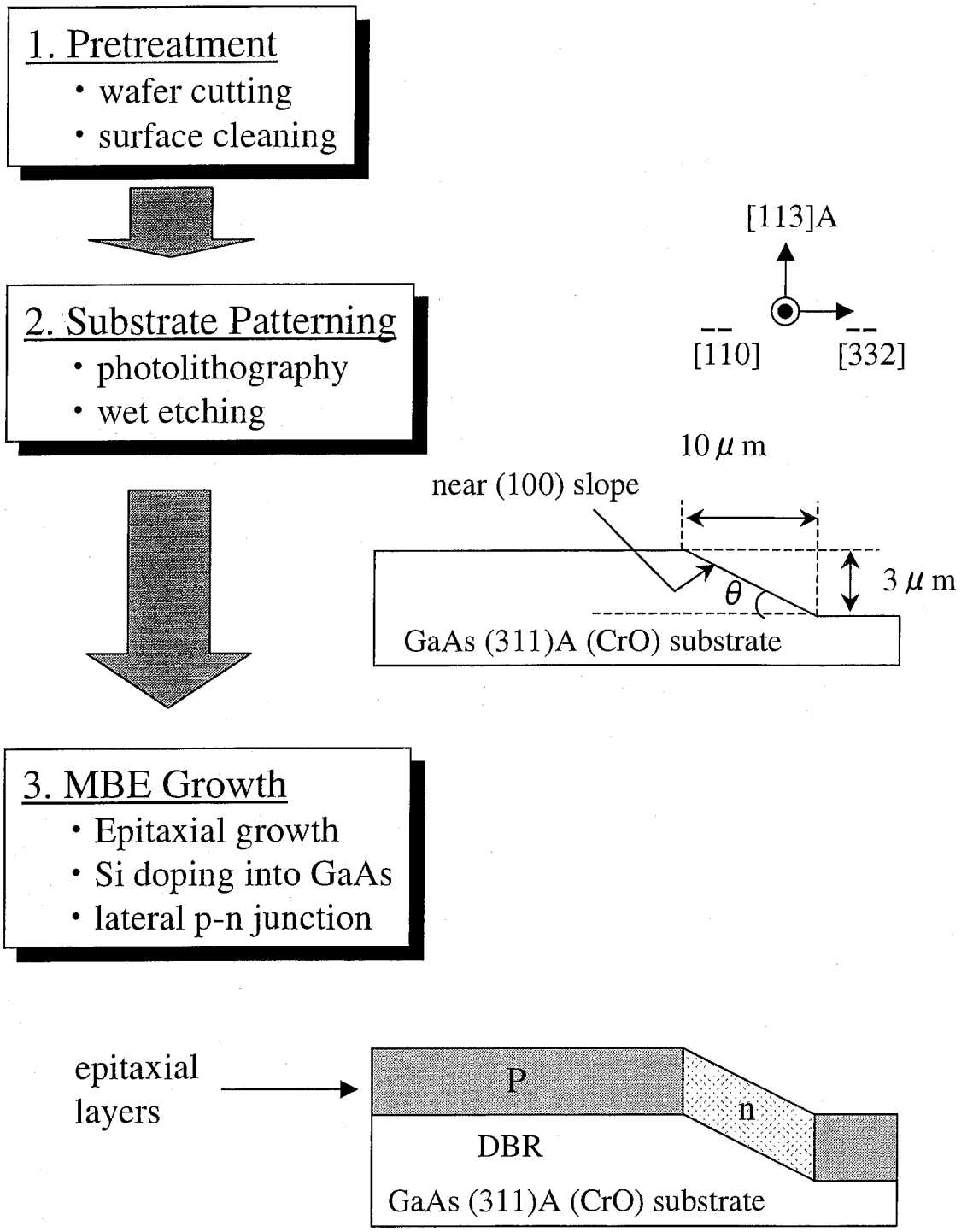

Fig. 3.1_1 Fabrication process flow of a lateral junction (LJ) LED (1)

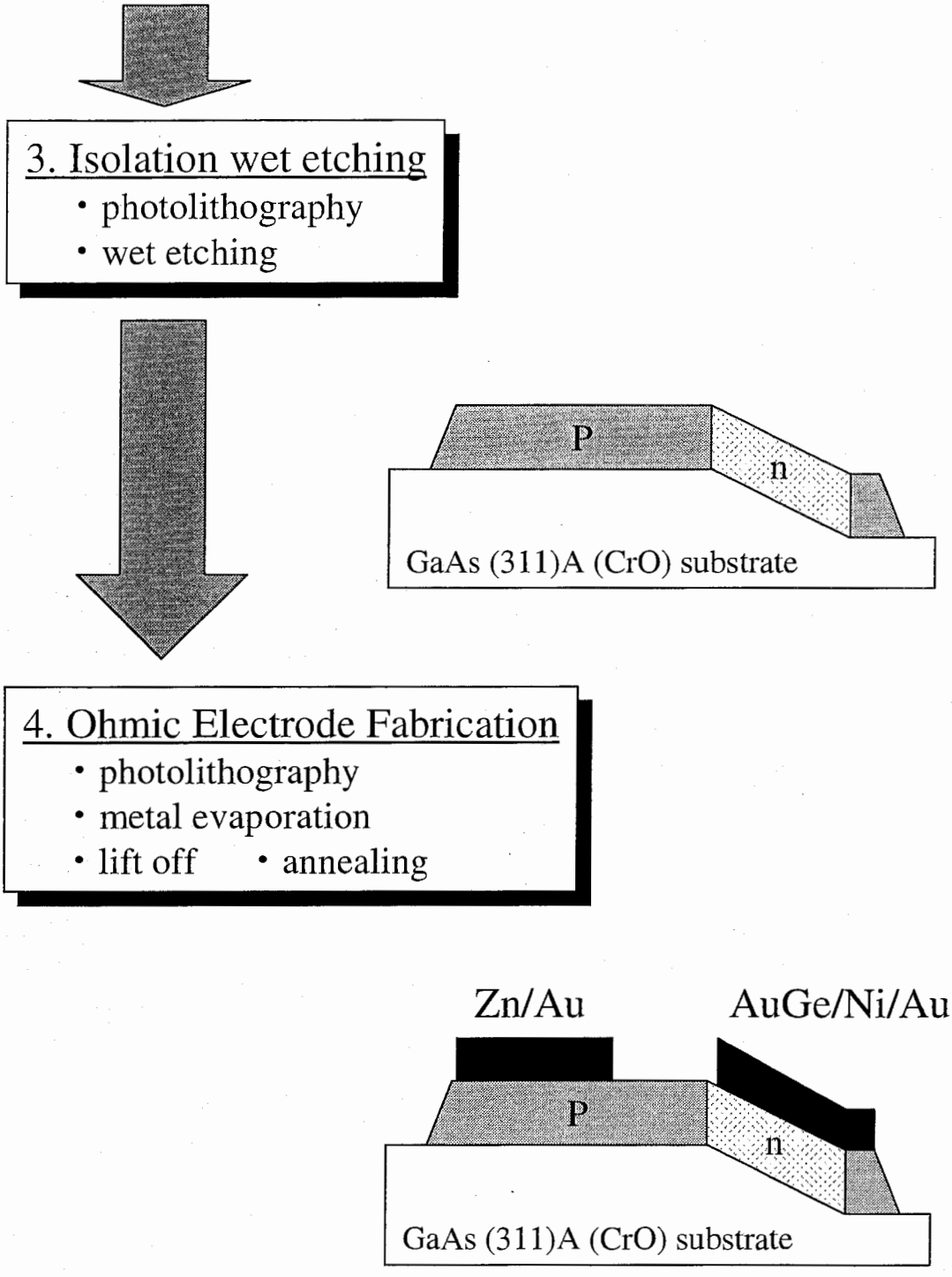

Fig. 3.1_2 Fabrication process flow of a LJ-LED (2)

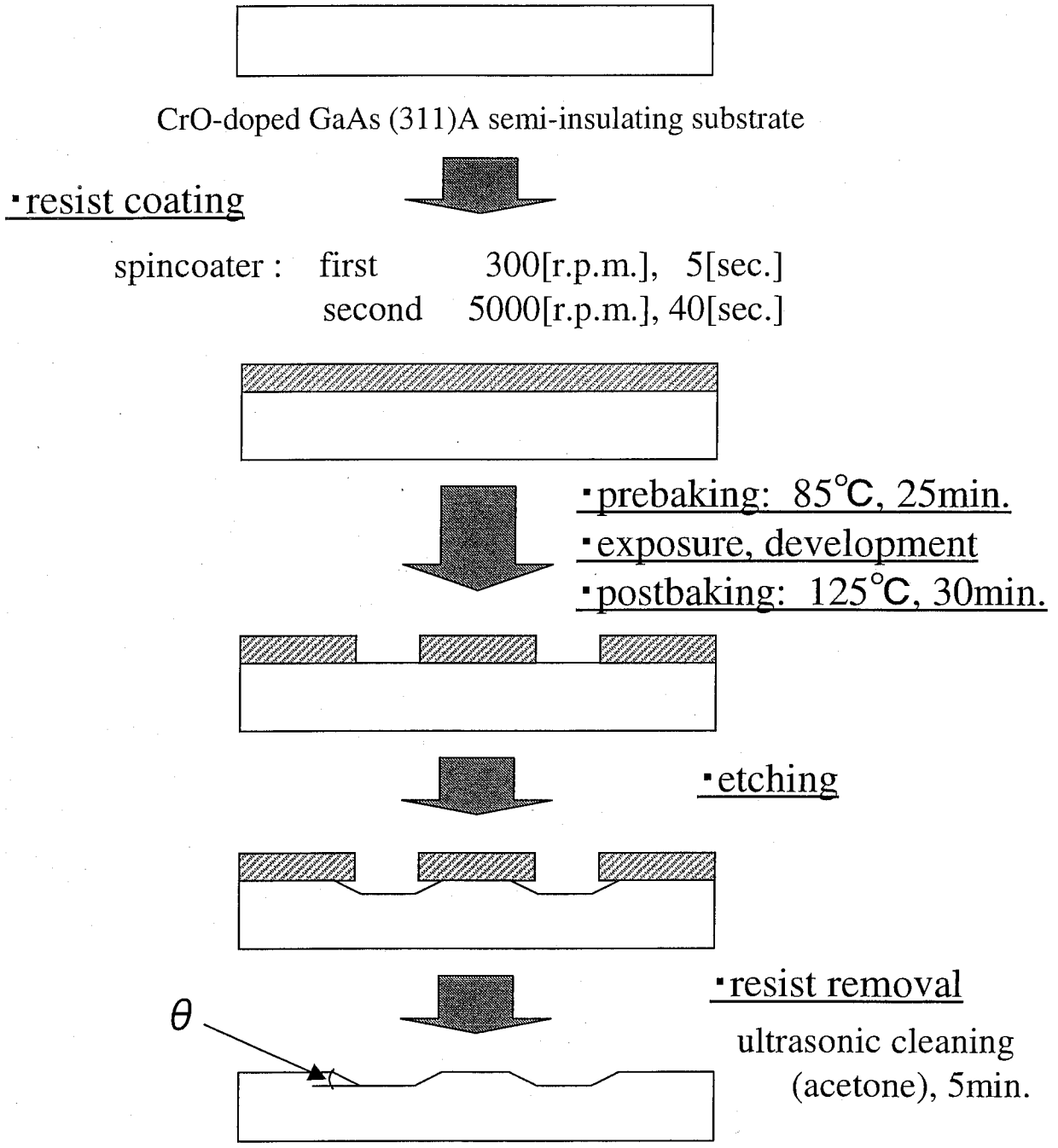

Fig. 3.2 Fabrication process flow diagram of a patterned substrate

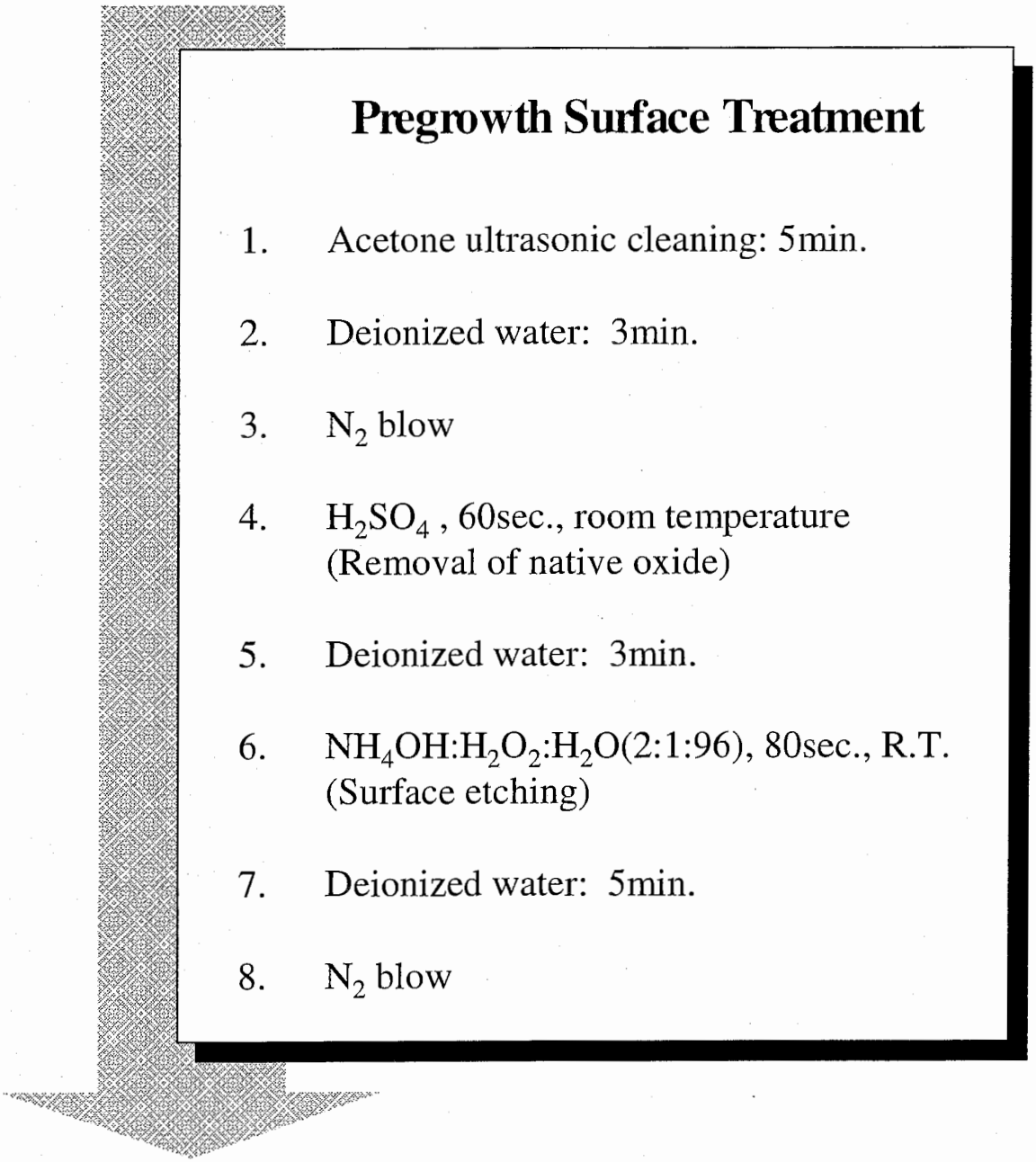

Fig. 3.3 Surface treatment process before MBE growth

Growth temperature	▪540℃ (311)A ▪580℃ (100)
As_4-BEP (Beam equivalent pressure)	▪6.48×10^{-6} Torr (GaAs) ▪1.17×10^{-5} Torr (AlGaAs)
Growth rate	▪469.5 nm/h (GaAs) ▪471.1 nm/h (AlAs)
Carrier concentration	▪(311)A 6.0×10^{16} cm^{-3} (p-type) ▪(100) 2.2×10^{16} cm^{-3} (n-type)

Table 3.1 MBE Growth Conditions

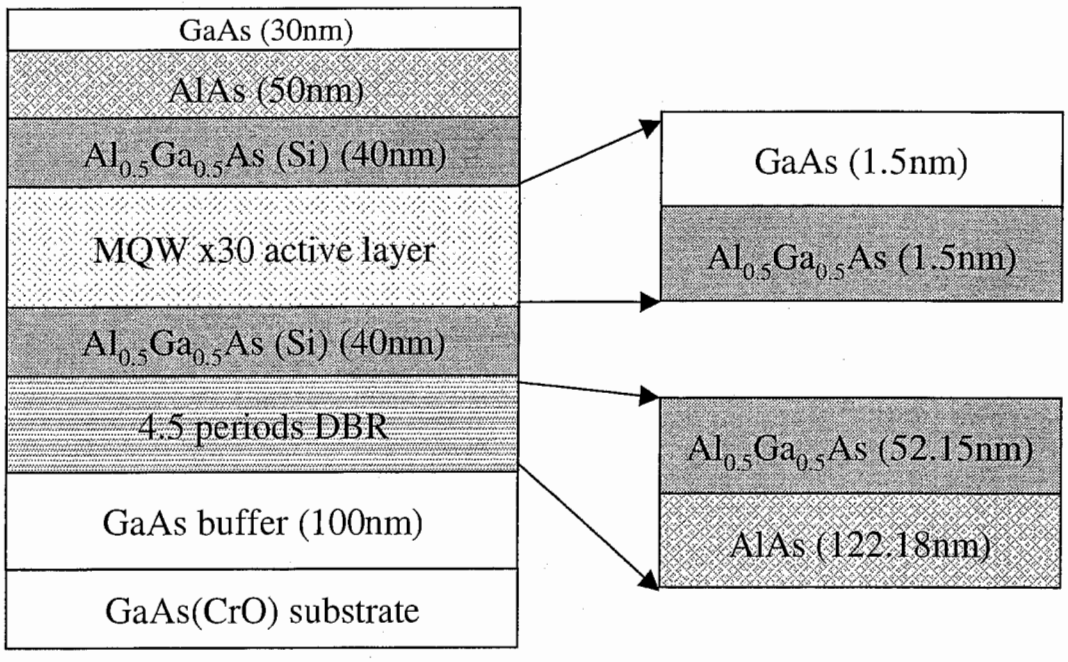

Fig. 3.4 Cross section view of multilayer structures grown by MBE

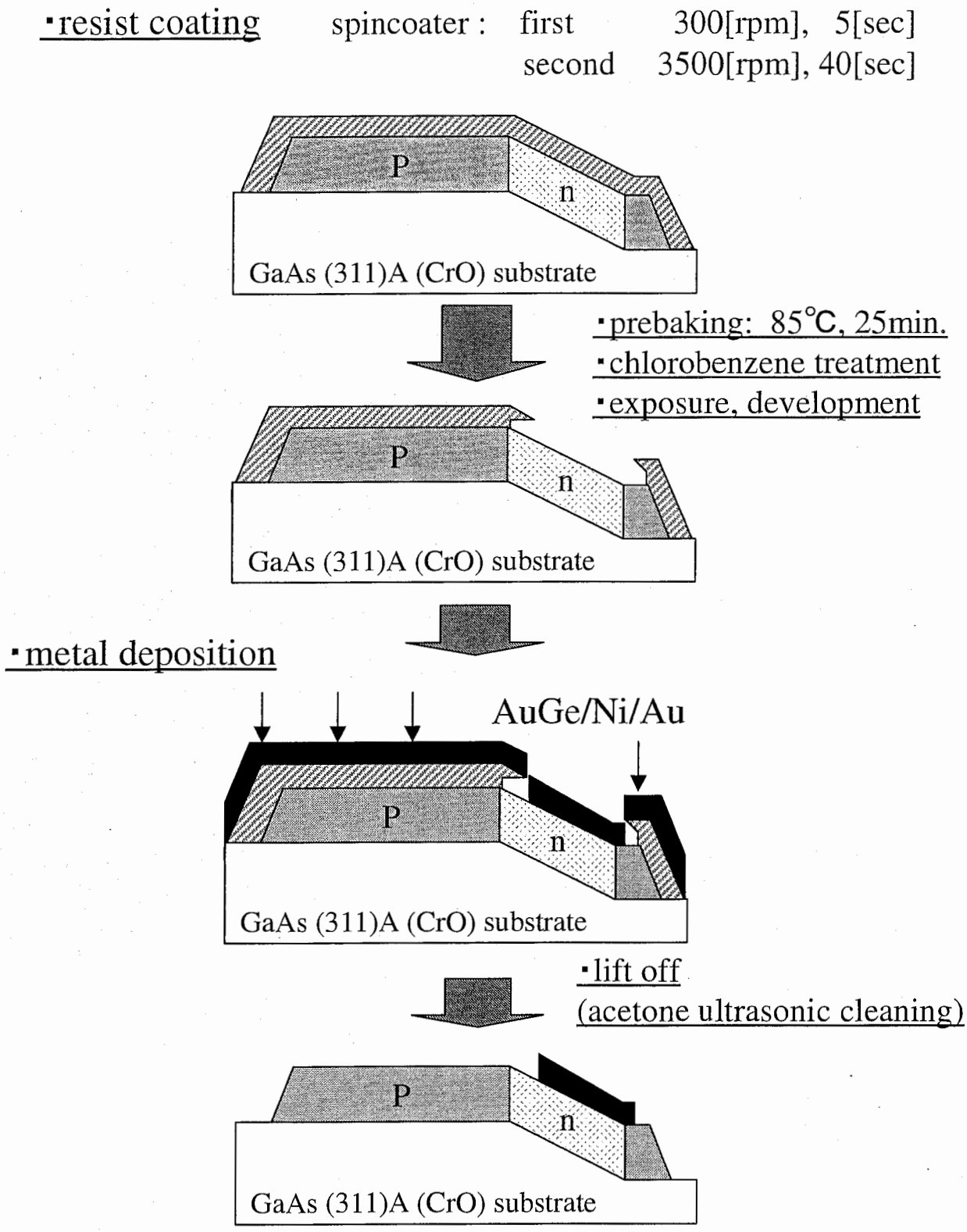

Fig. 3.5 Fabrication process flow of n-type ohmic electrode

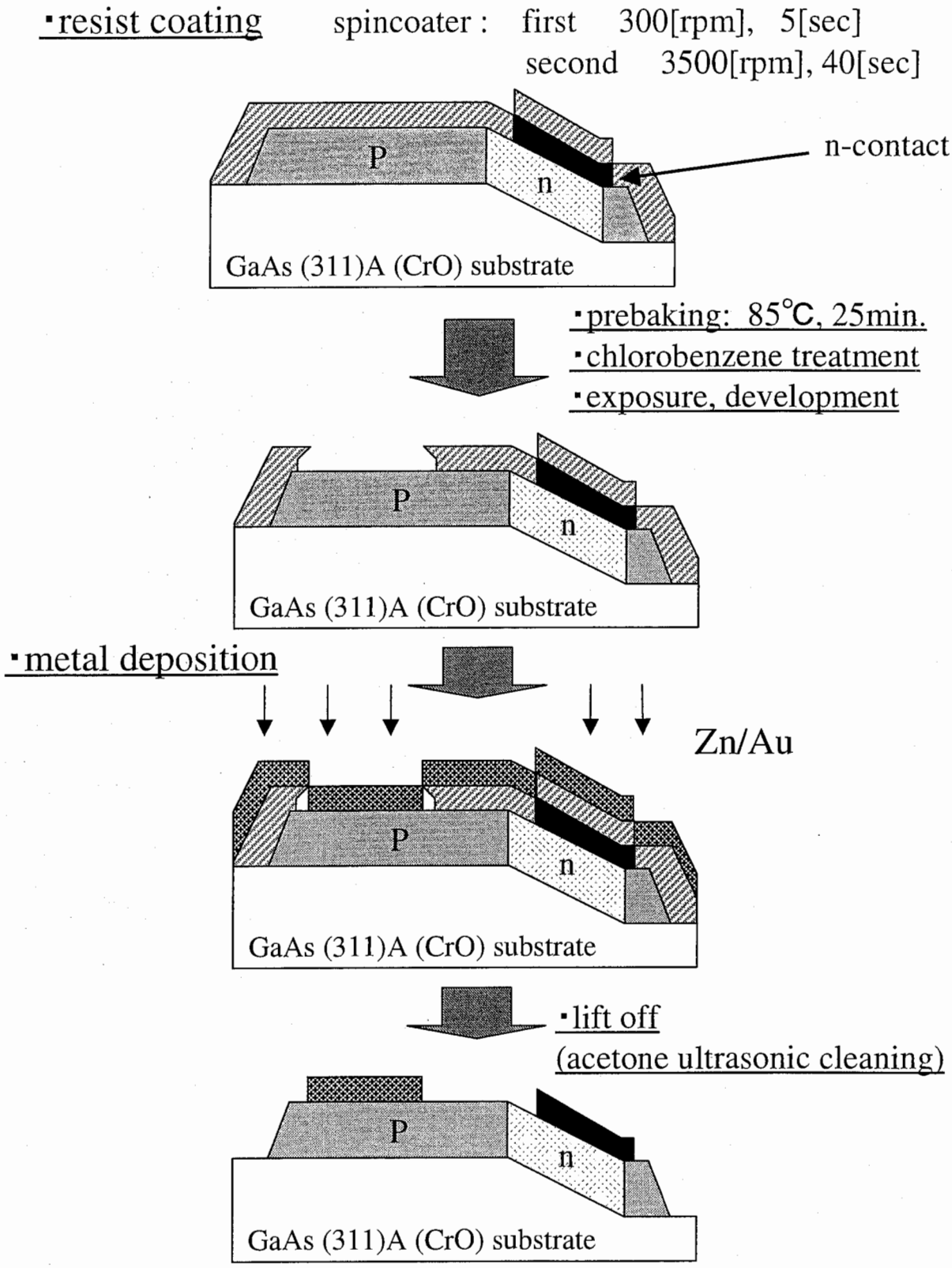

Fig. 3.6 Fabrication process flow of p-type ohmic electrode

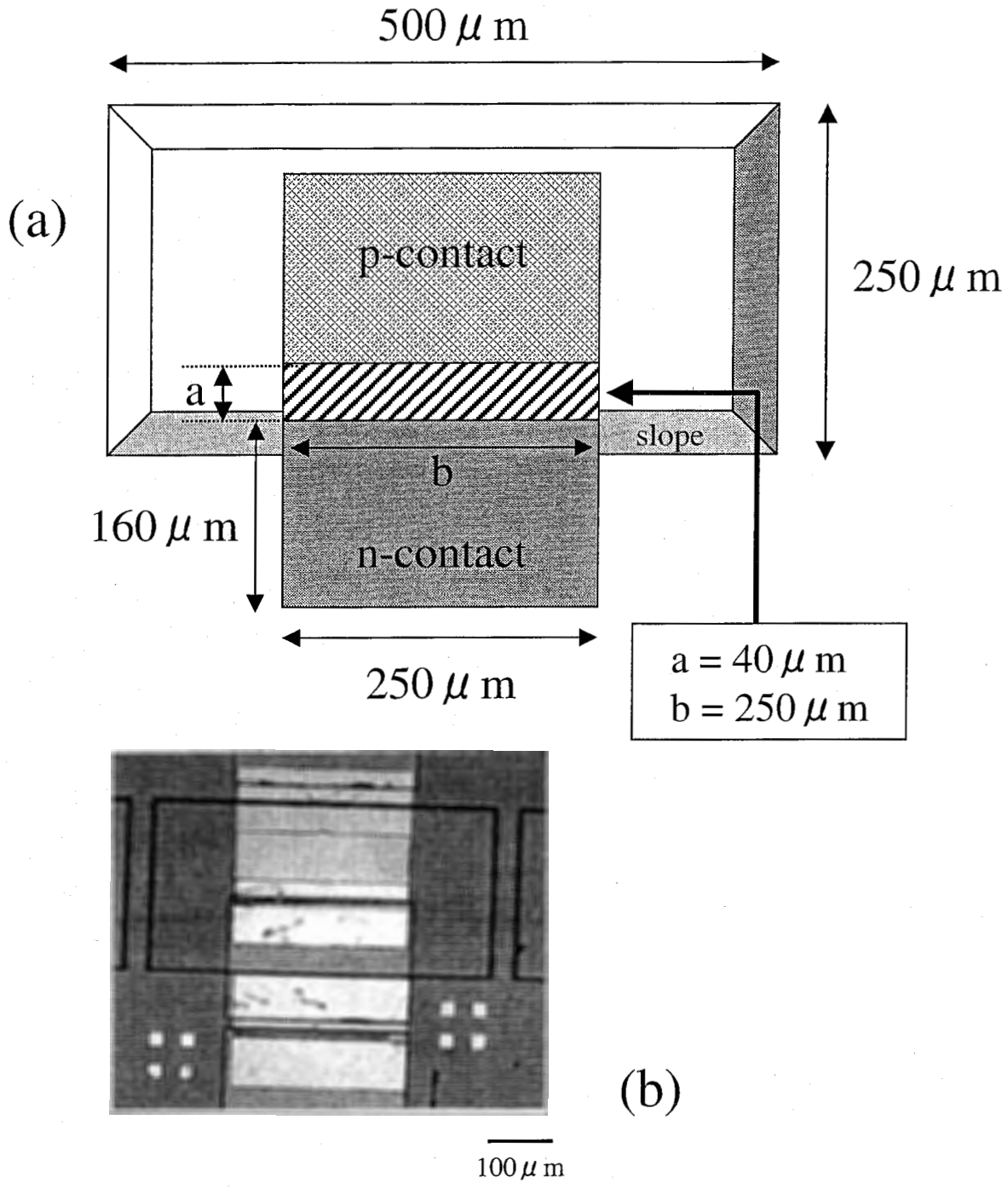

Fig. 3.7 Top view of the LJ-visible LED
(a) Schematic illustration
(b) Optical microscope image

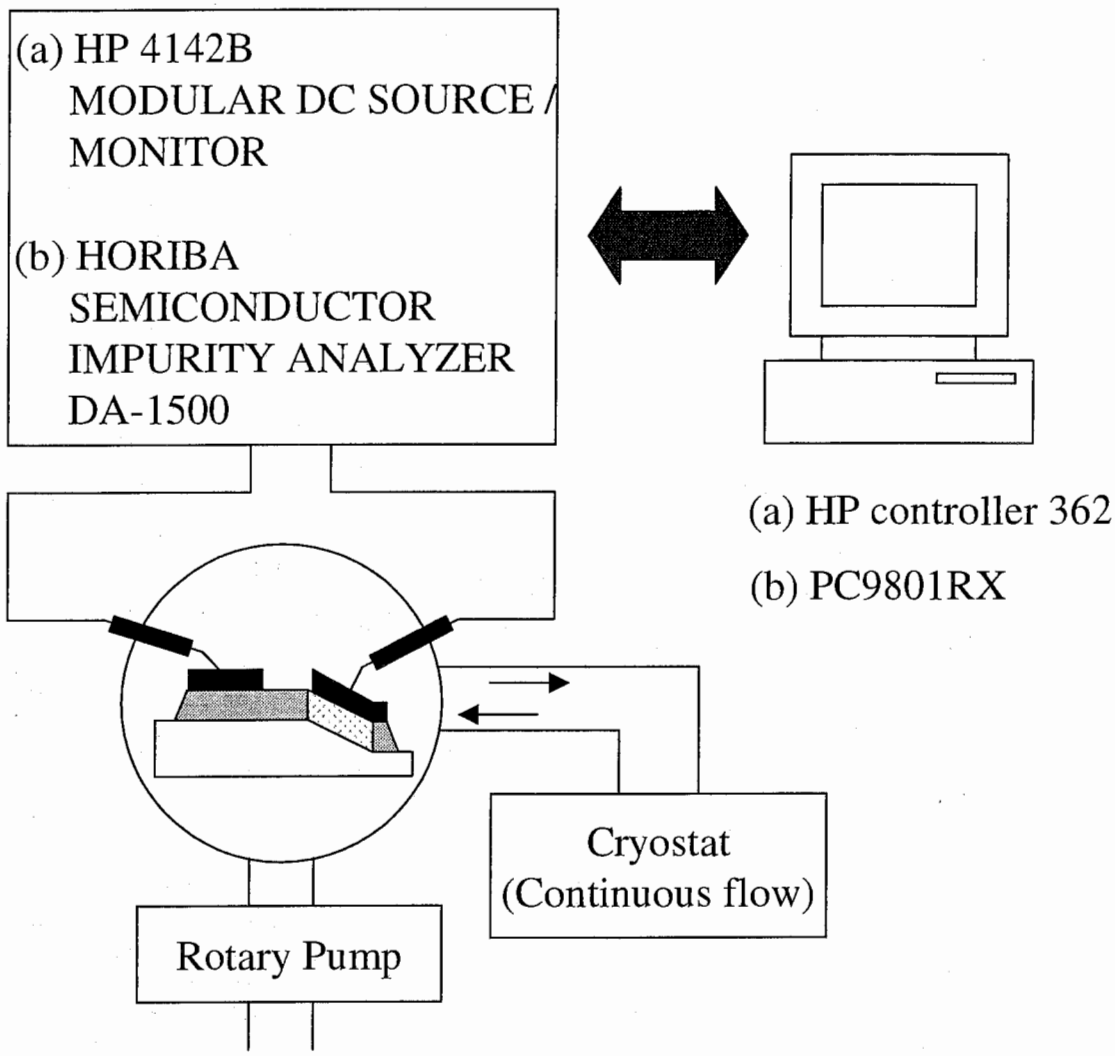

Fig. 3.8 Experimental apparatus for
(a) I-V measurements
(b) C-V measurements

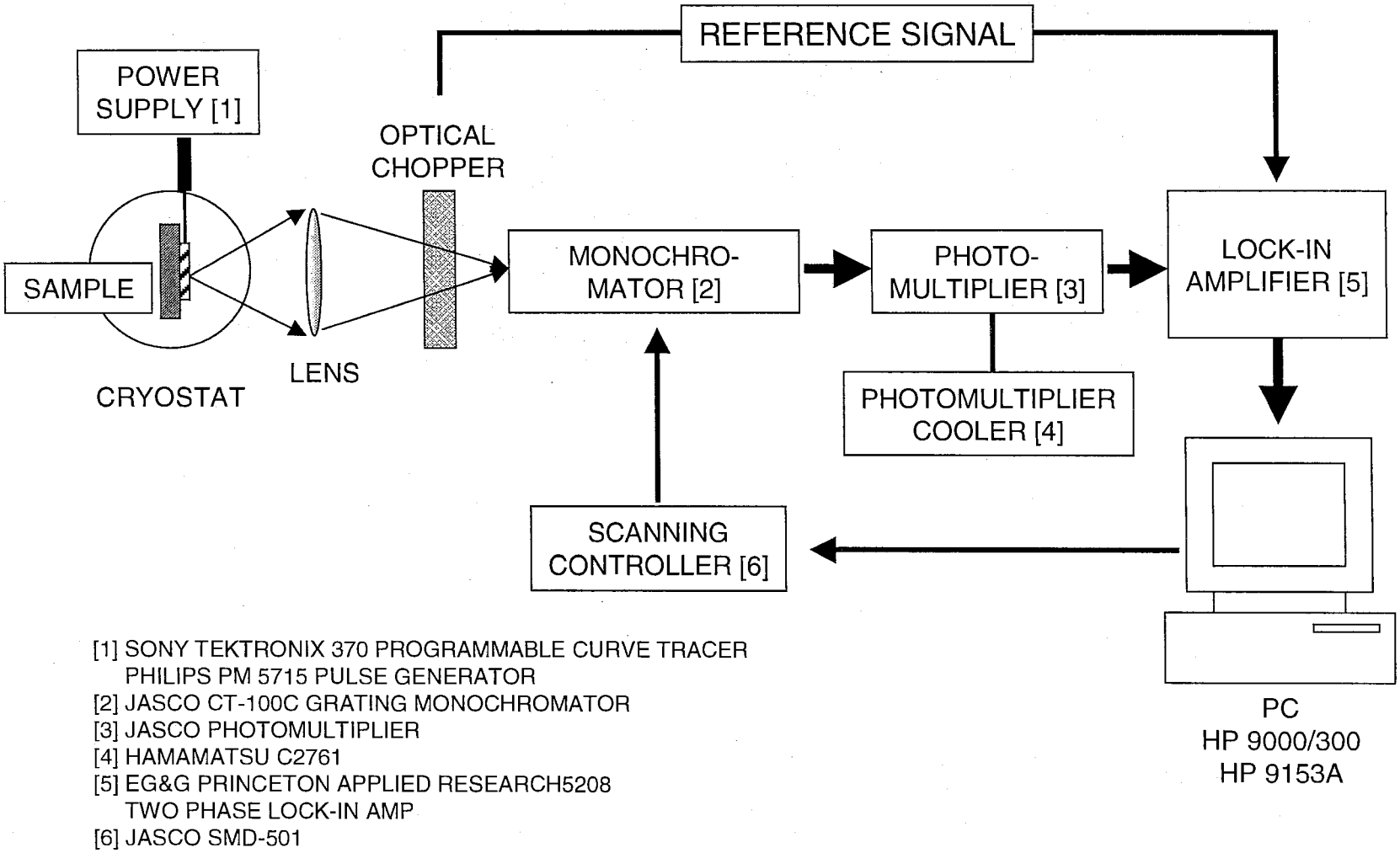

Fig. 3.9 Experimental apparatus for EL measurements

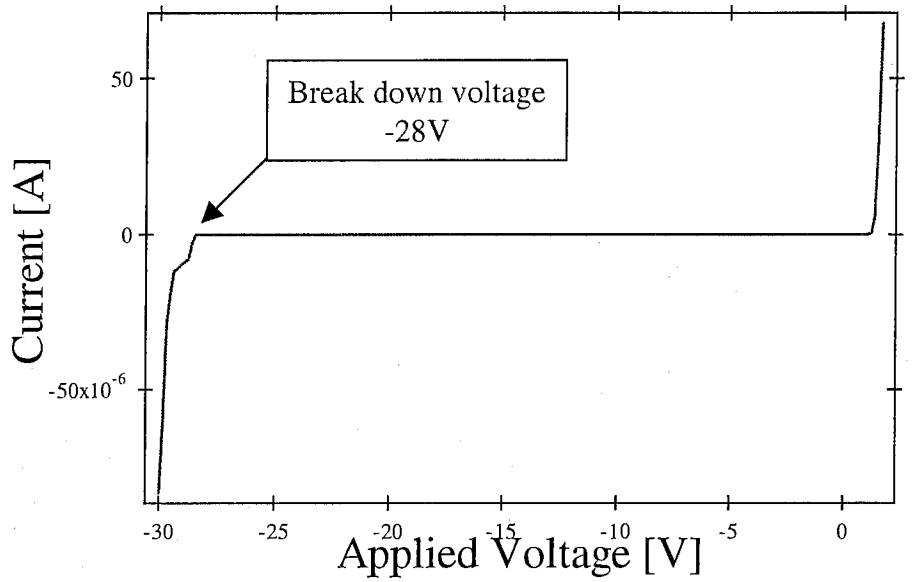

(a)

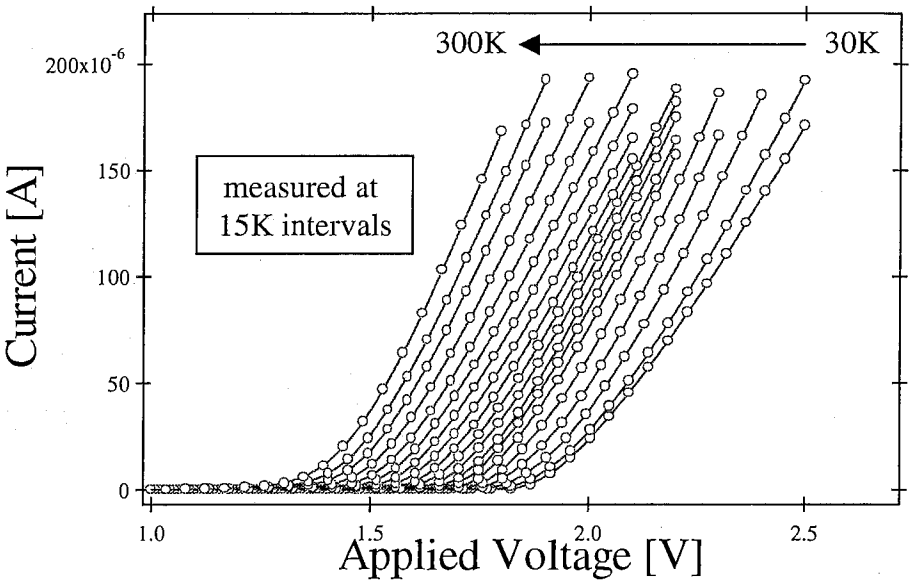

(b)

Fig. 3.10 I-V characteristics of the LJ-visible LED at (a) room temperature and (b) low temperatures

$$I_d = I_s \exp\left(\frac{qV_d}{nkT}\right)$$

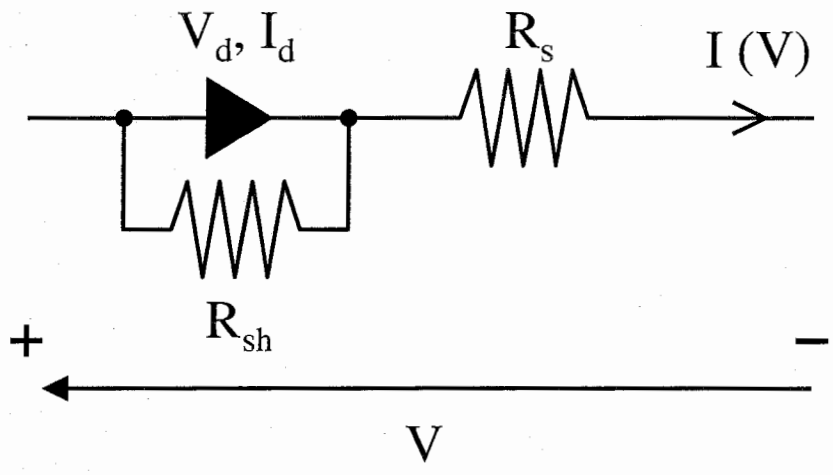

Fig. 3.11 Equivalent circuit of an actual diode under forward bias conditions

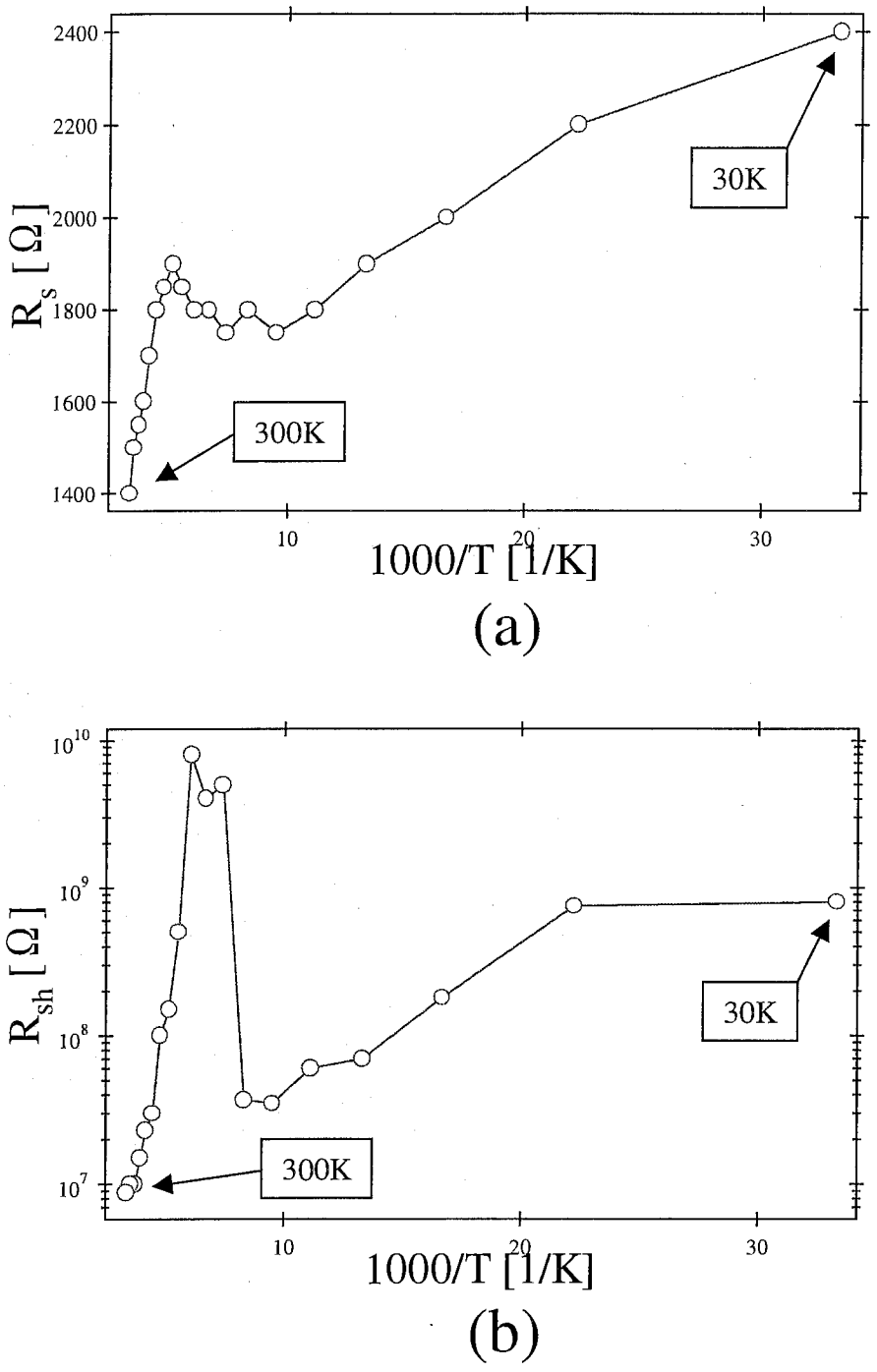

Fig. 3.12 Resistances of the LJ-visible LED as a function of the temperature
(a) Series resistance, R_s
(b) Shunt resistance, R_{sh}

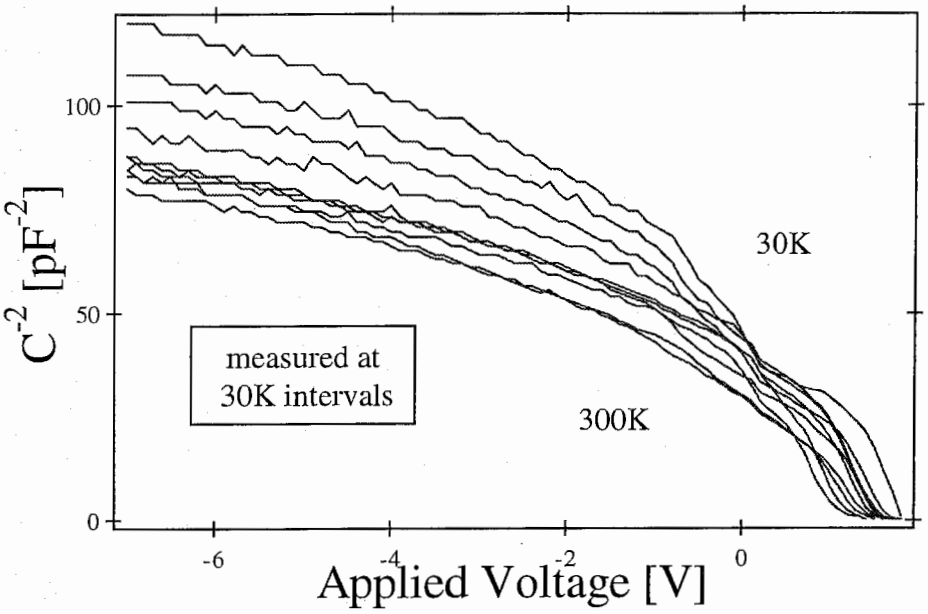

Fig. 3.13 C^2-V characteristics of the LJ-visible LED as a function of the temperature

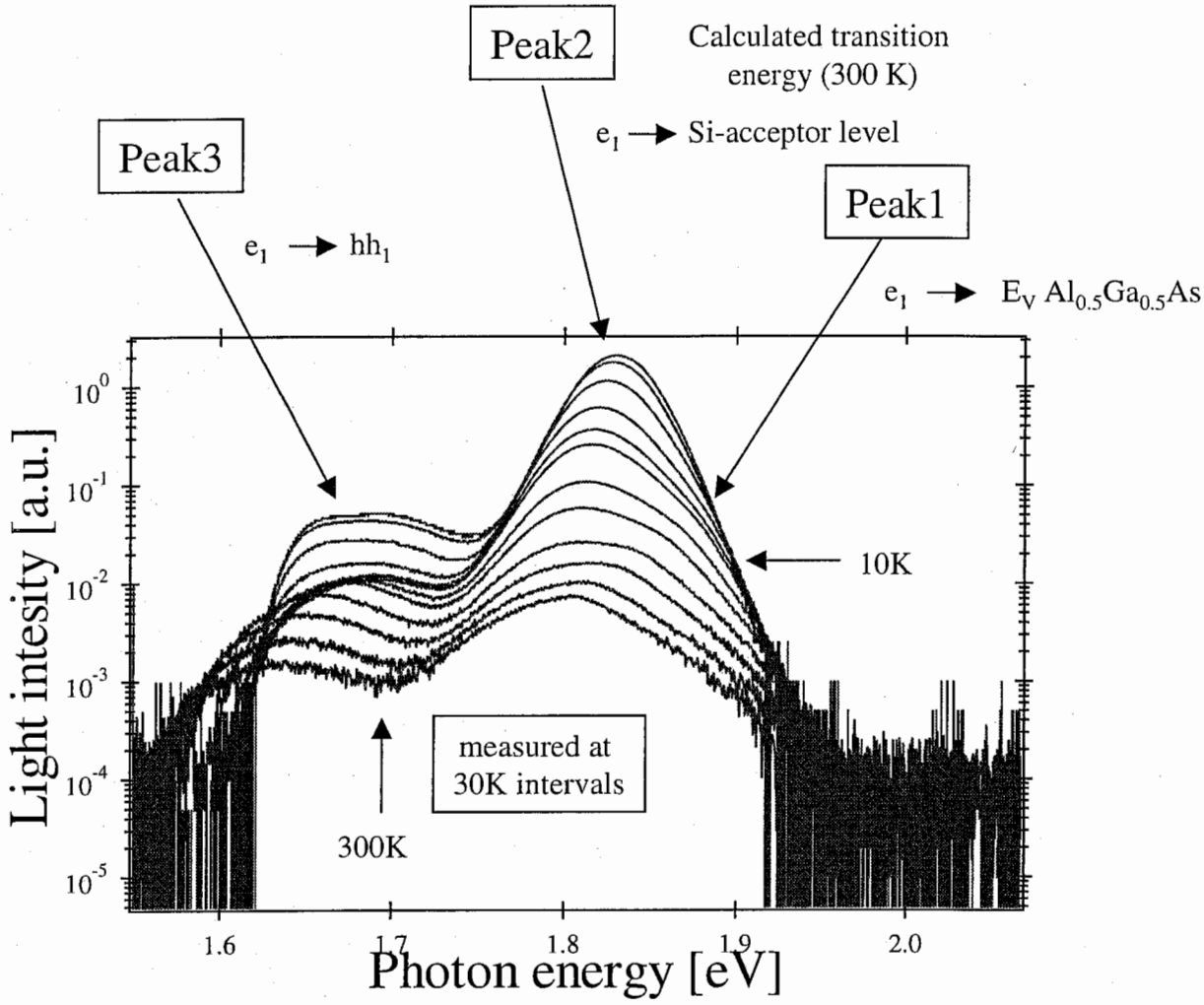

Fig. 3.14 EL spectra of the LJ-visible LED at various temperatures. The applied current was 0.2mA.

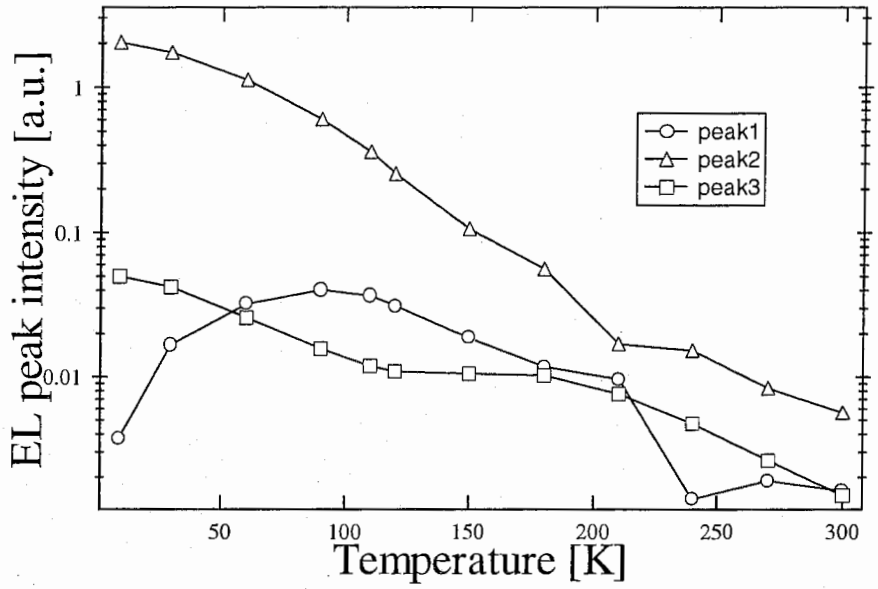

(a)

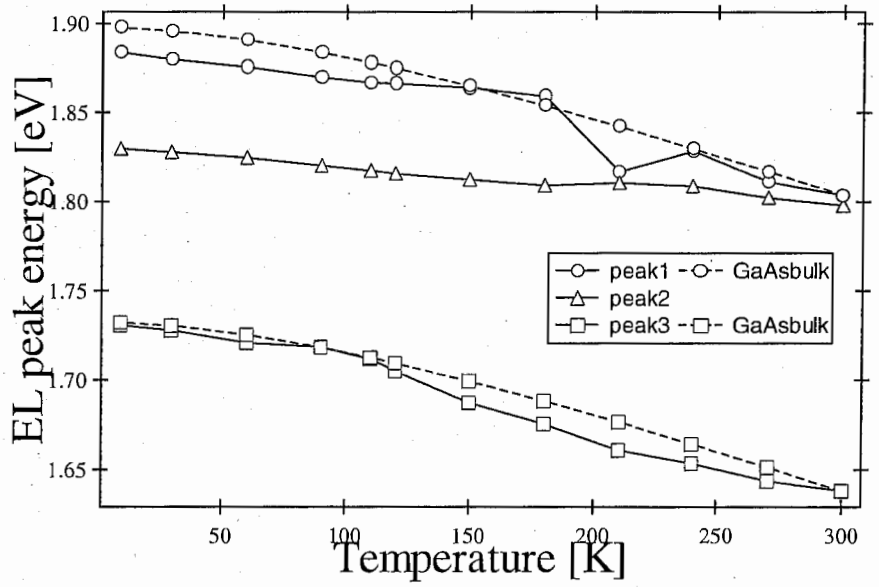

(b)

Fig. 3.15 EL spectrum peaks of the LJ-visible LED with an applied current of 0.2mA
(a) Peak light intensity versus temperature
(b) Peak band gap energy versus temperature

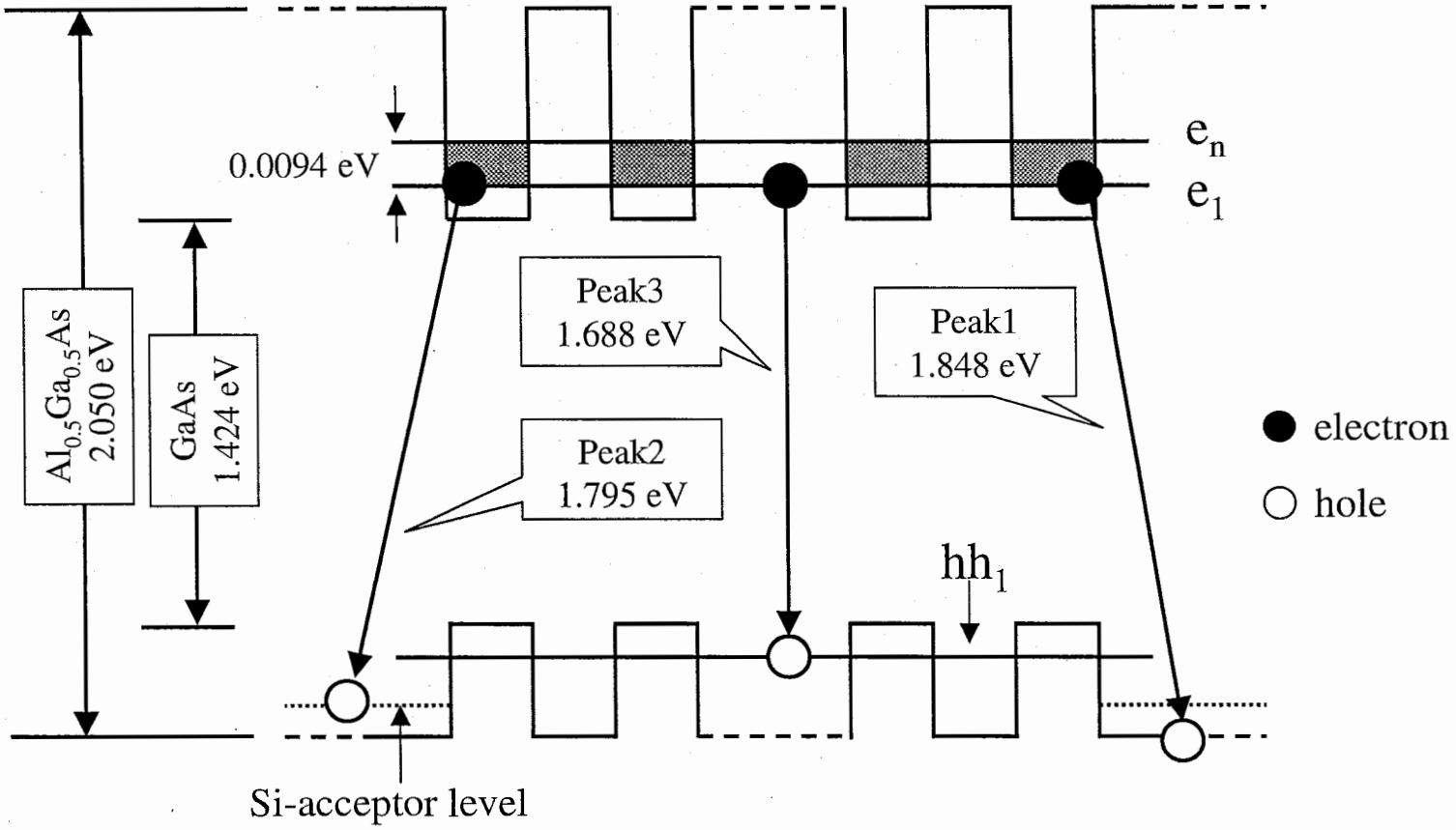

Fig. 3.16 Energy band diagram of $Al_{0.5}Ga_{0.5}As$/GaAs MQW at 300 K. The applied current is 0.2mA.

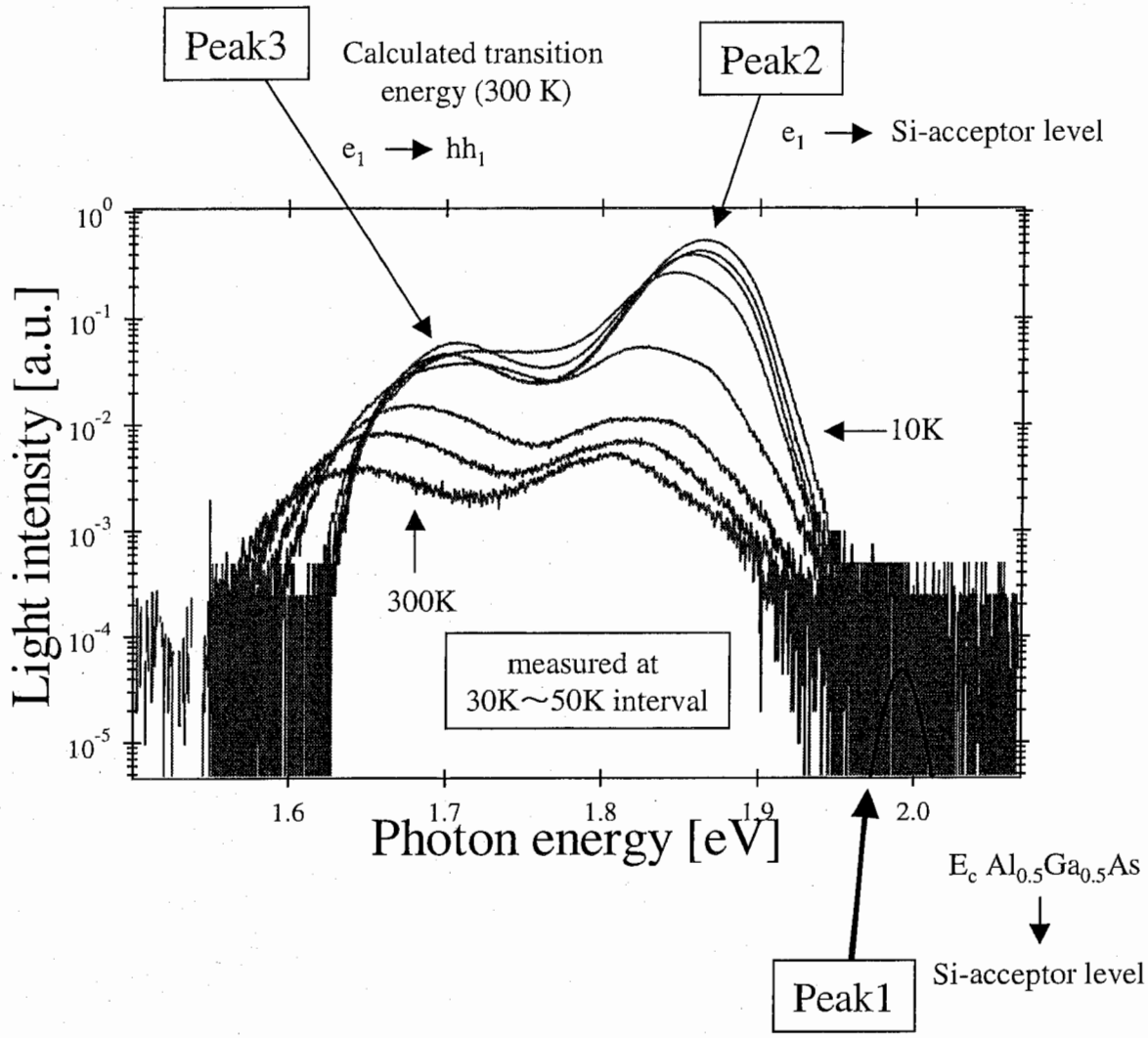

Fig. 3.17 EL spectra of the LJ-visible LED at various temperatures. The applied current was 2.3mA.

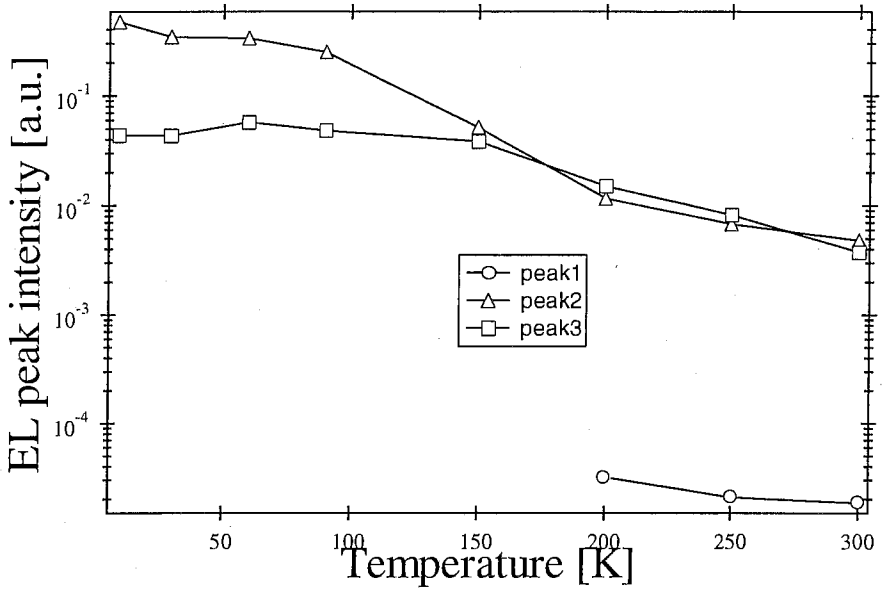

(a)

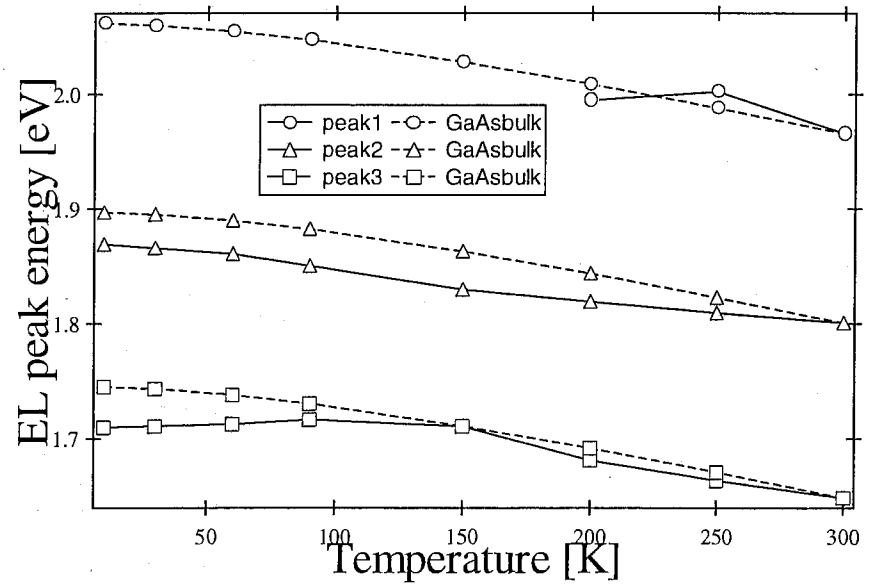

(b)

Fig. 3.18 EL spectrum peaks of the LJ-visible LED with an applied current of 2.3mA.
(a) Peak light intensity versus temperature
(b) Peak band gap energy versus temperature

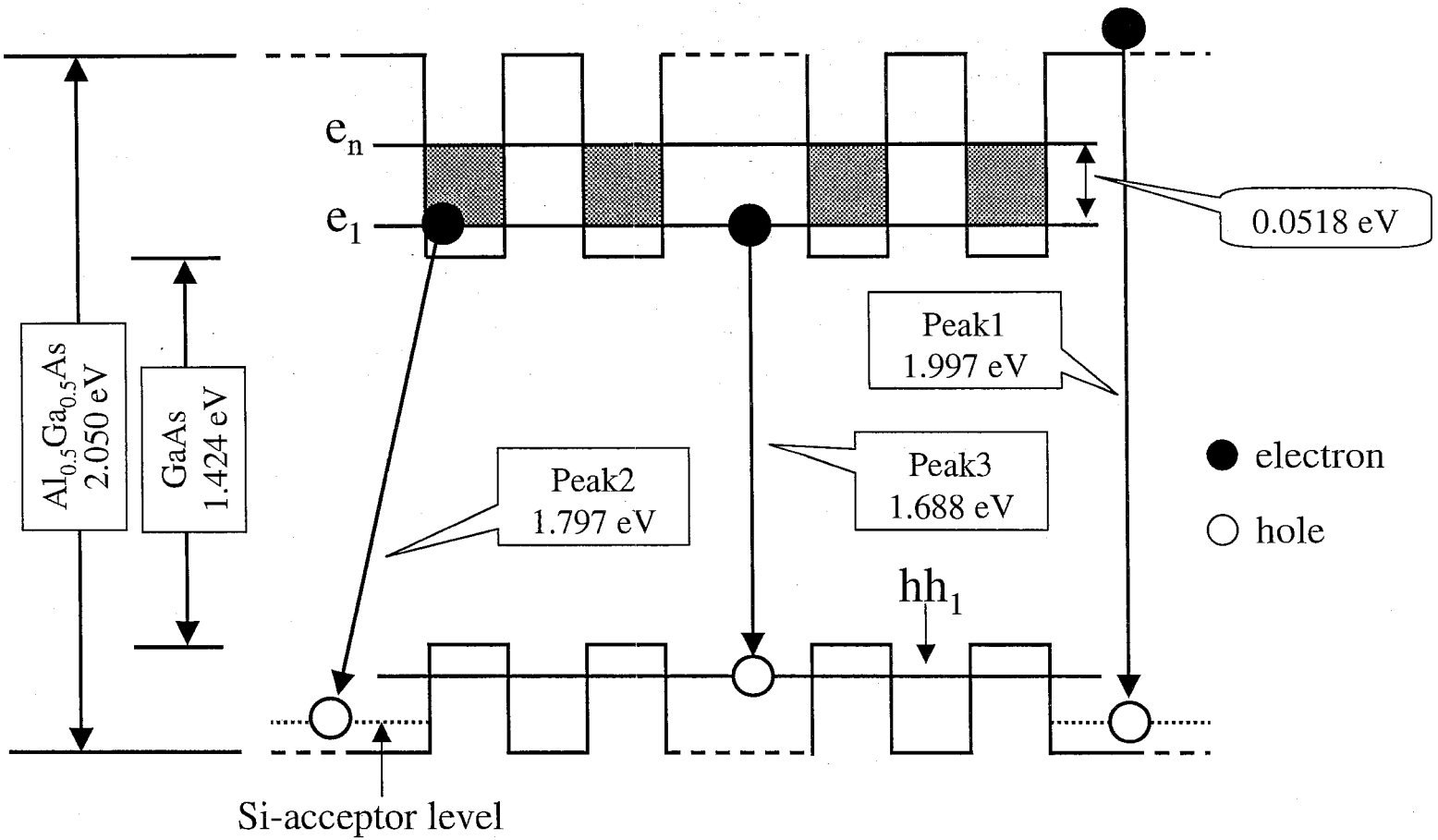

Fig. 3.19 Energy band diagram of $Al_{0.5}Ga_{0.5}As$/GaAs MQW at 300 K. The applied current is 2.3mA.

Growth temperature	▪540℃ (311)A ▪580℃ (100)
As_4-BEP (Beam equivalent pressure)	▪7.53×10^{-6} Torr (GaAs) ▪1.51×10^{-5} Torr (AlGaAs)
Growth rate	▪800 nm/h (GaAs) ▪343 nm/h (AlAs) ▪200 nm/h (InAs)
Carrier concentration	▪(311)A 3.81×10^{18} cm^{-3} (p-type) ▪(100) 3.04×10^{17} cm^{-3} (n-type)

Table 4.1 MBE Growth Conditions

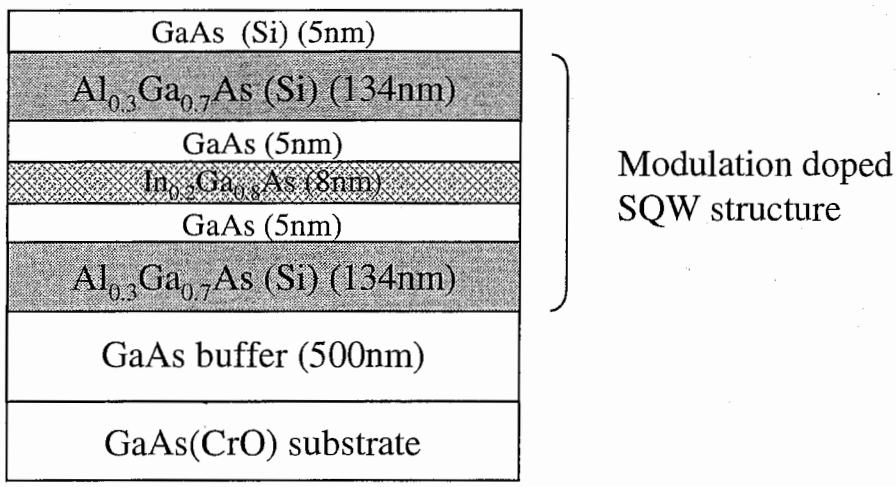

Fig. 4.1 Cross section view of multilayer structures grown by MBE

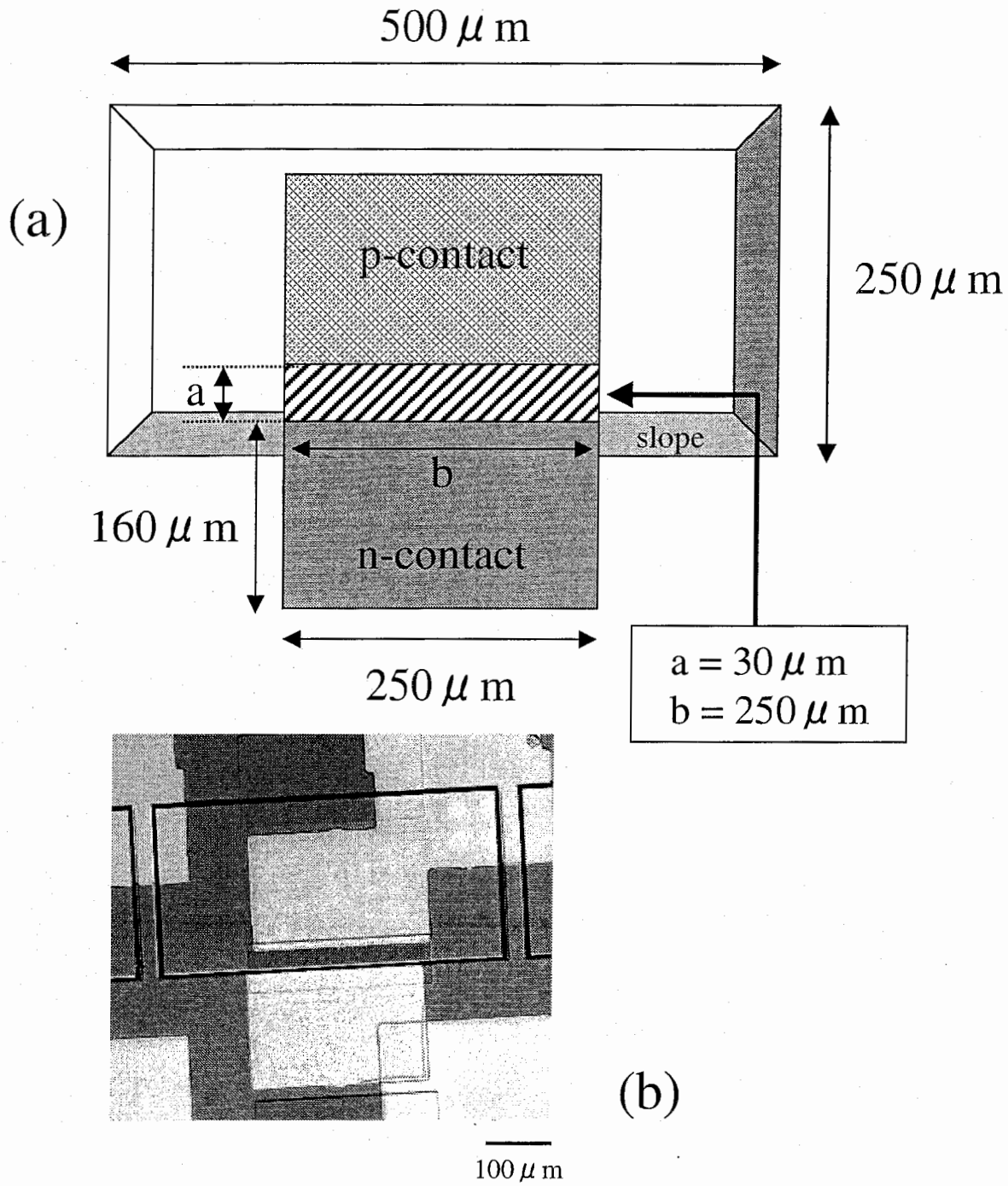

Fig. 4.2 Top view of the LJ-modulation doped LED
(a) Schematic illustration
(b) Optical microscope image

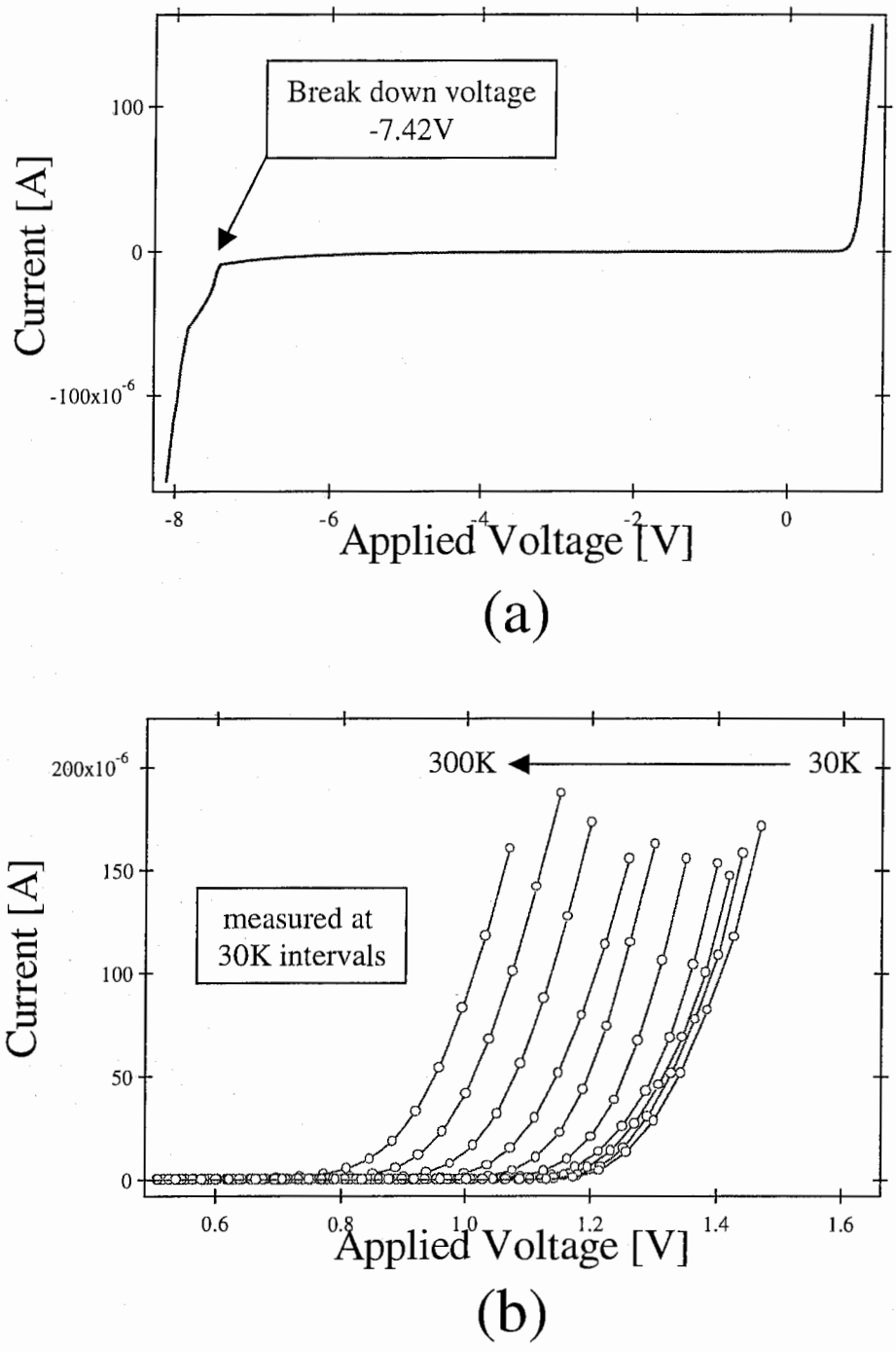

Fig. 4.3 I-V characteristics of the LJ-modulation doped LED at (a) room temperature and (b) low temperatures

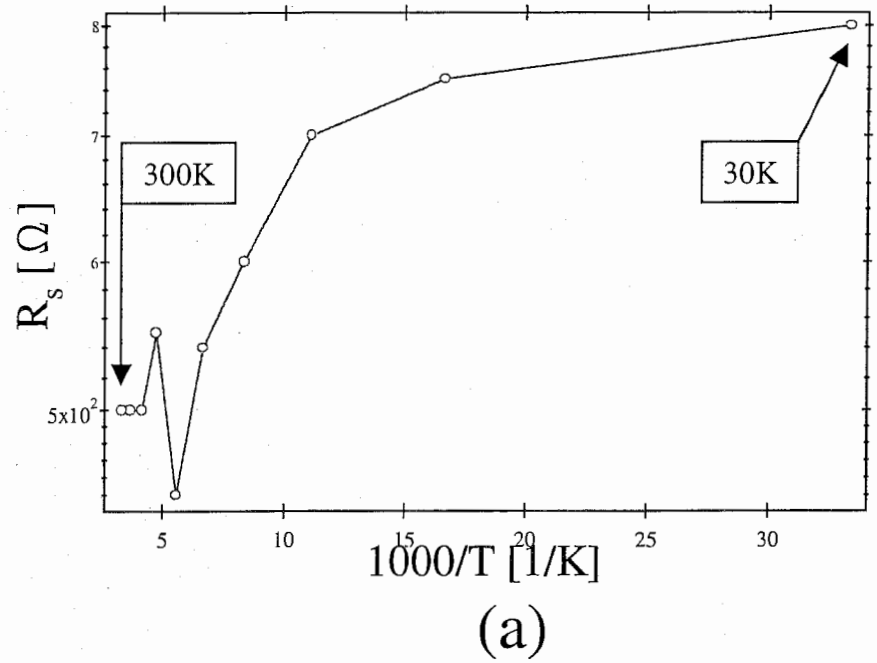

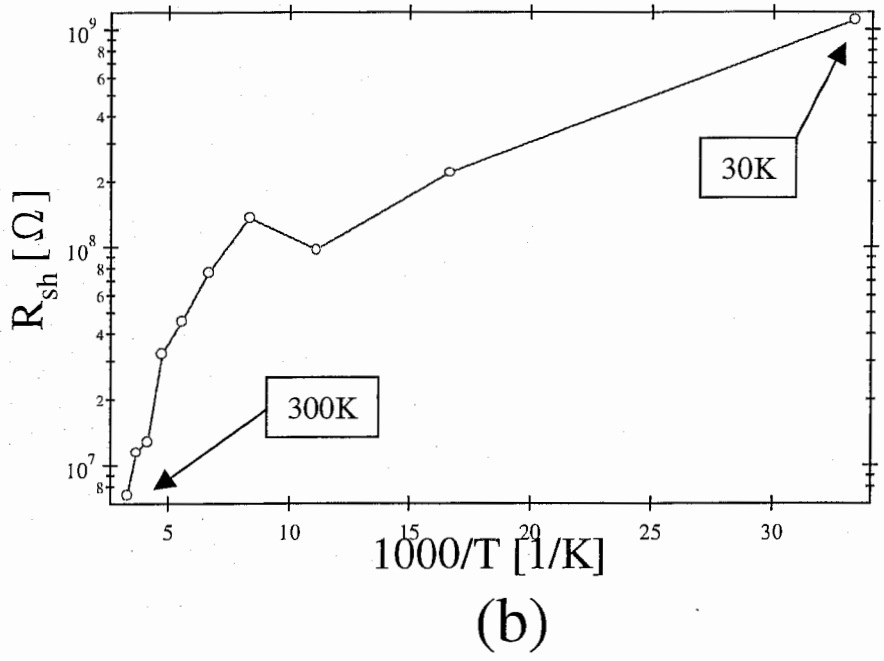

Fig. 4.4 Resistances of the LJ-modulation doped LED as a function of the temperature
(a) Series resistance, R_s
(b) Shunt resistance, R_{sh}

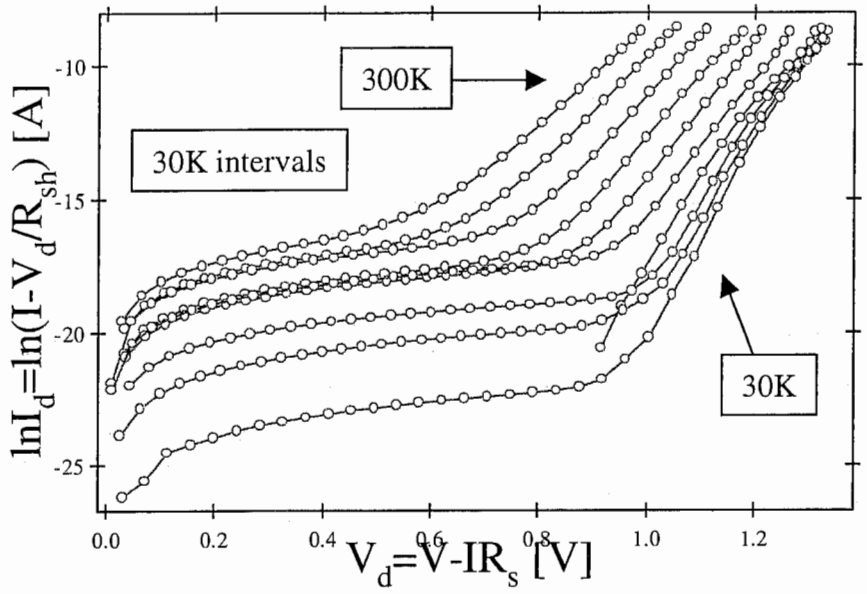

(a)

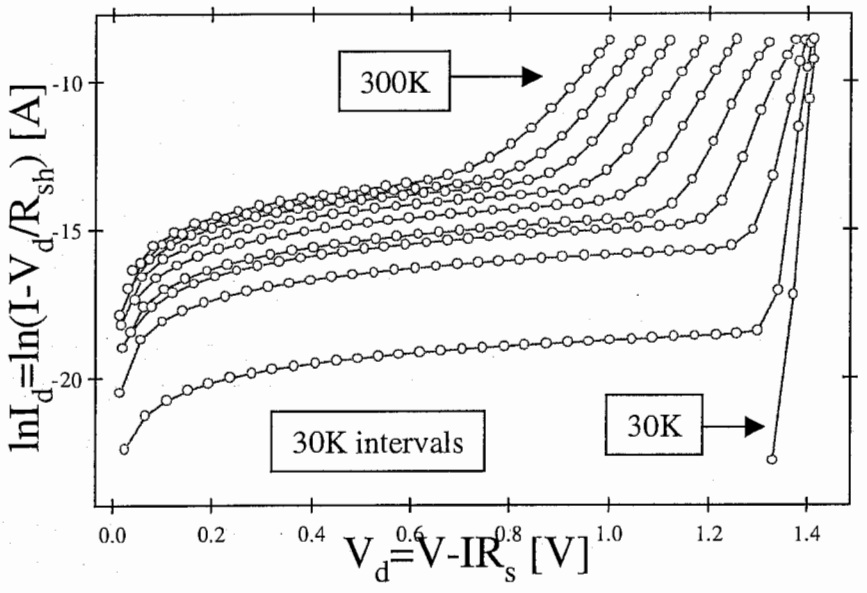

(b)

Fig. 4.5 Fitted I-V curves of the LJ-modulation doped LED with
(a) MBE growth temperature of 540℃
(b) MBE growth temperature of 560℃

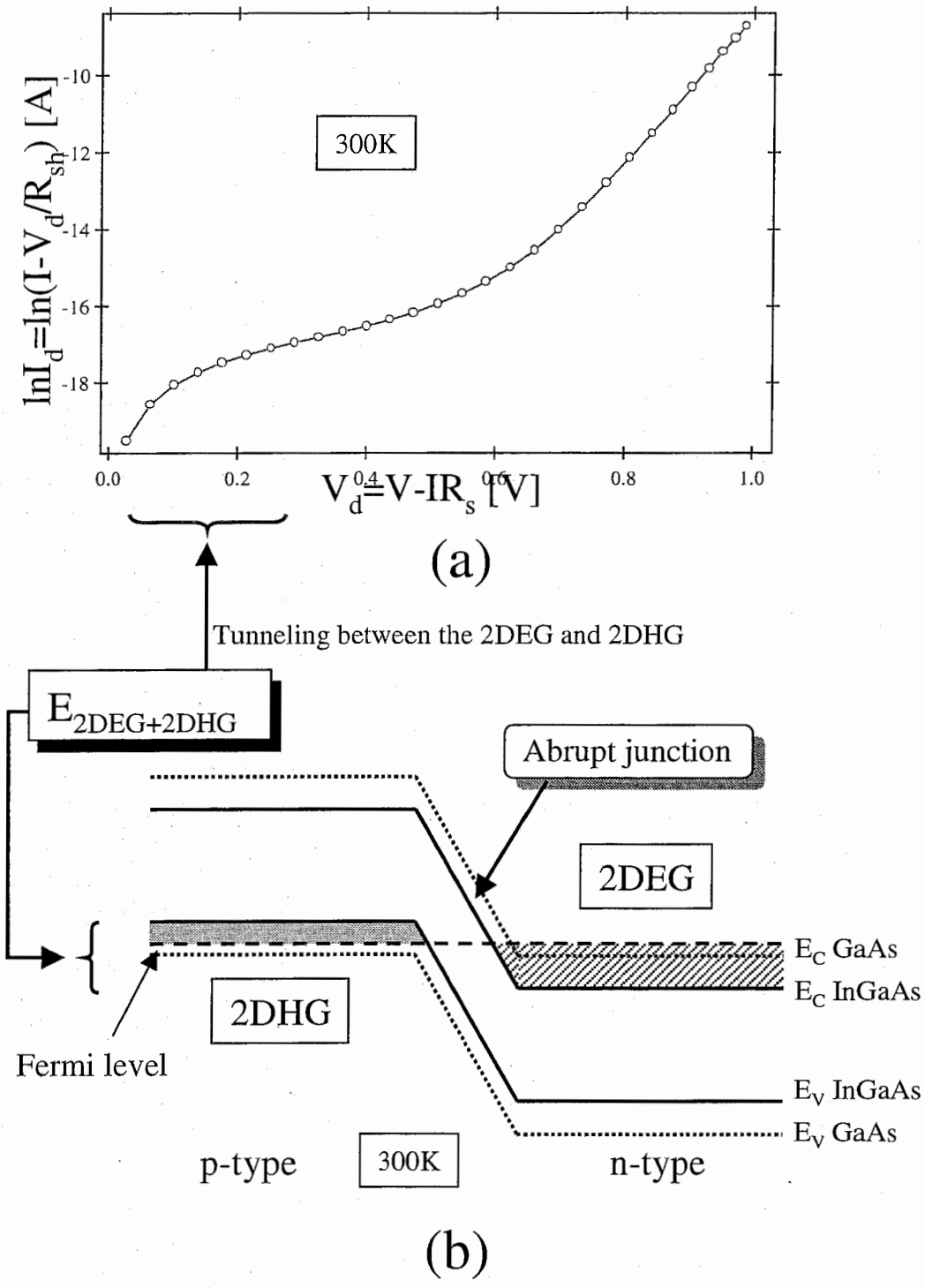

Fig. 4.6 (a) Fitted I-V curve of the LJ-modulation doped LED at 300 K
(b) Energy band diagram of an abrupt p-n junction between two doped regions at 300 K

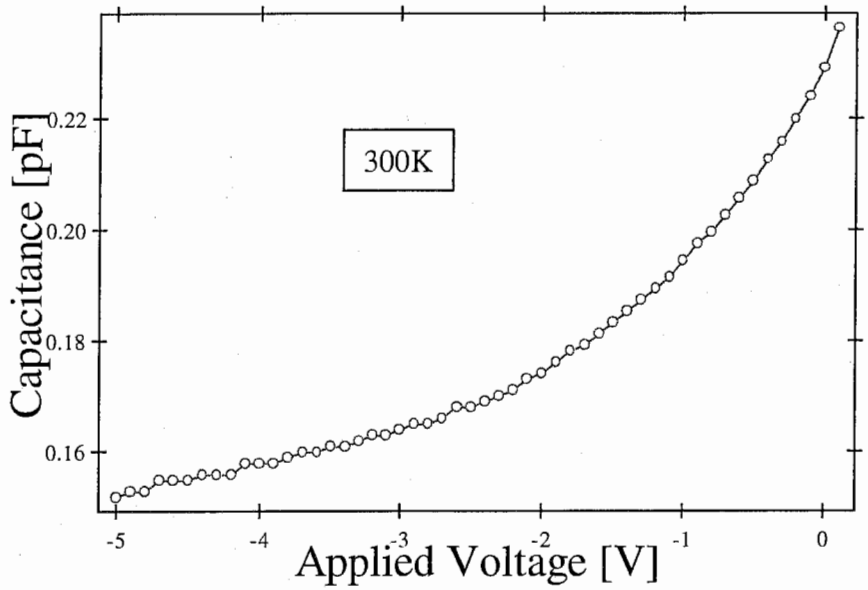

(a)

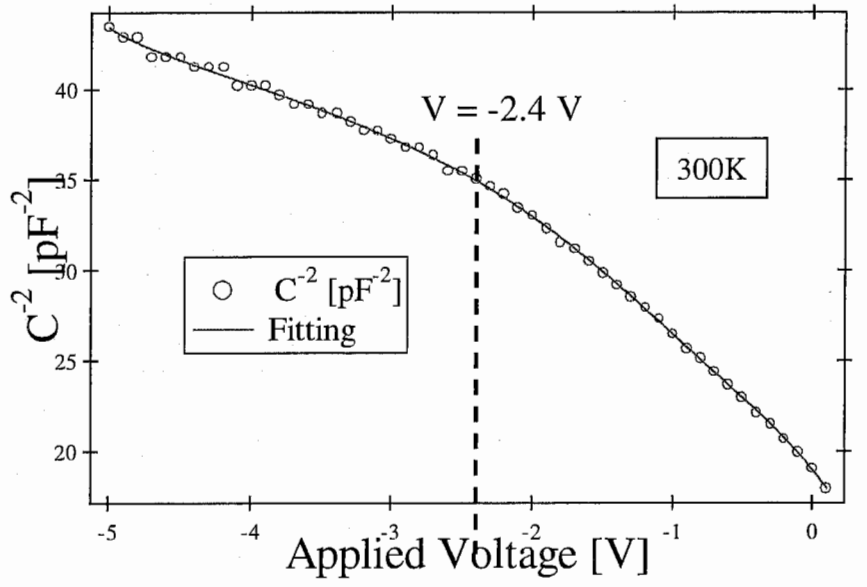

(b)

Fig. 4.7 (a) C-V characteristics and (b) C^2-V characteristics of the LJ-modulation doped LED at 300 K

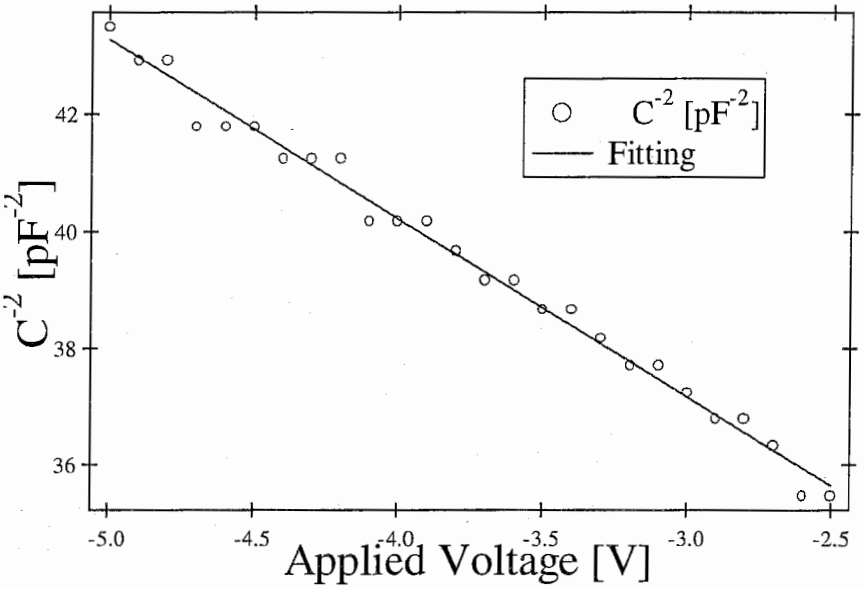

(a)

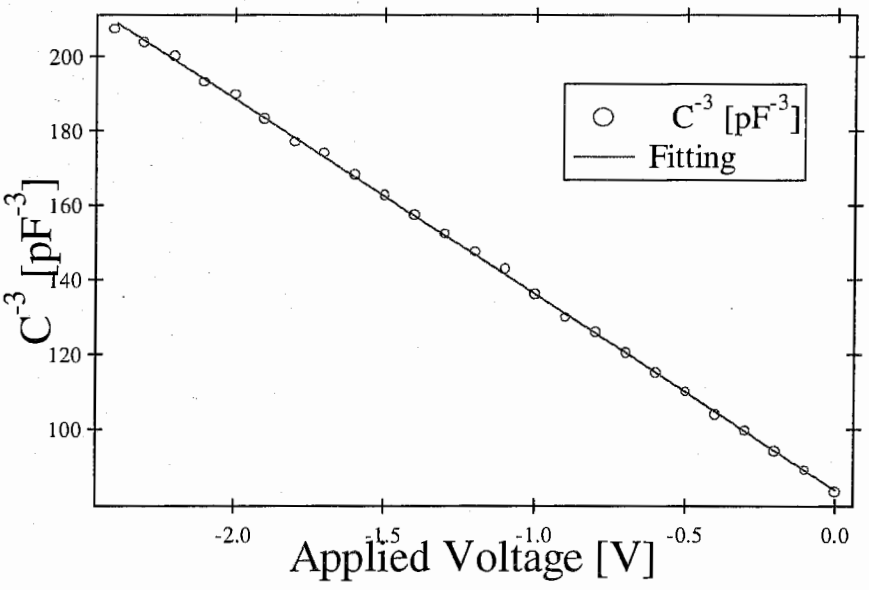

(b)

Fig. 4.8 (a) C^2-V characteristics for the applied current of V < -2.4 V
(b) C^3-V characteristics for the applied current of V > -2.4 V

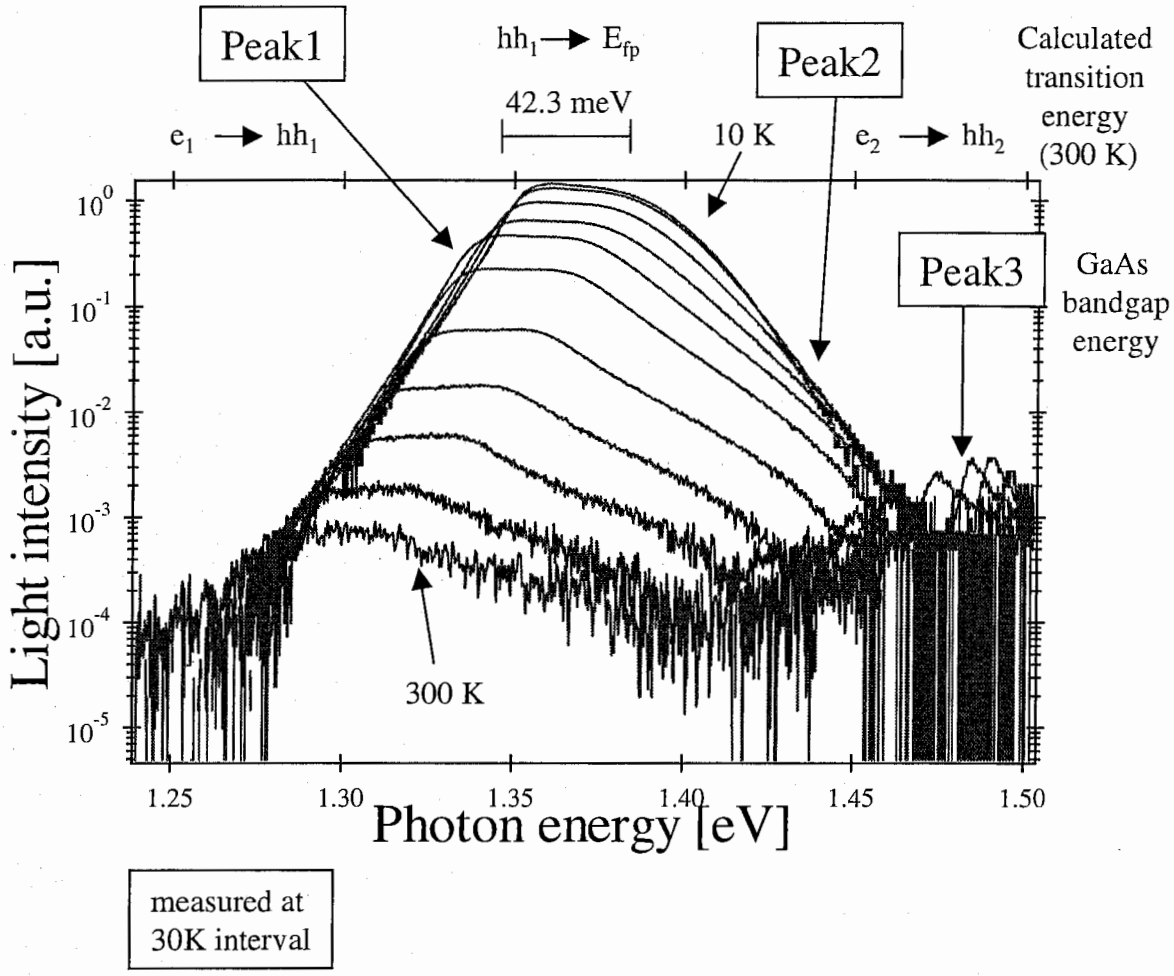

Fig. 4.9 EL spectra of the LJ-modulation doped LED at various temperatures. The applied current was 2.0 mA.

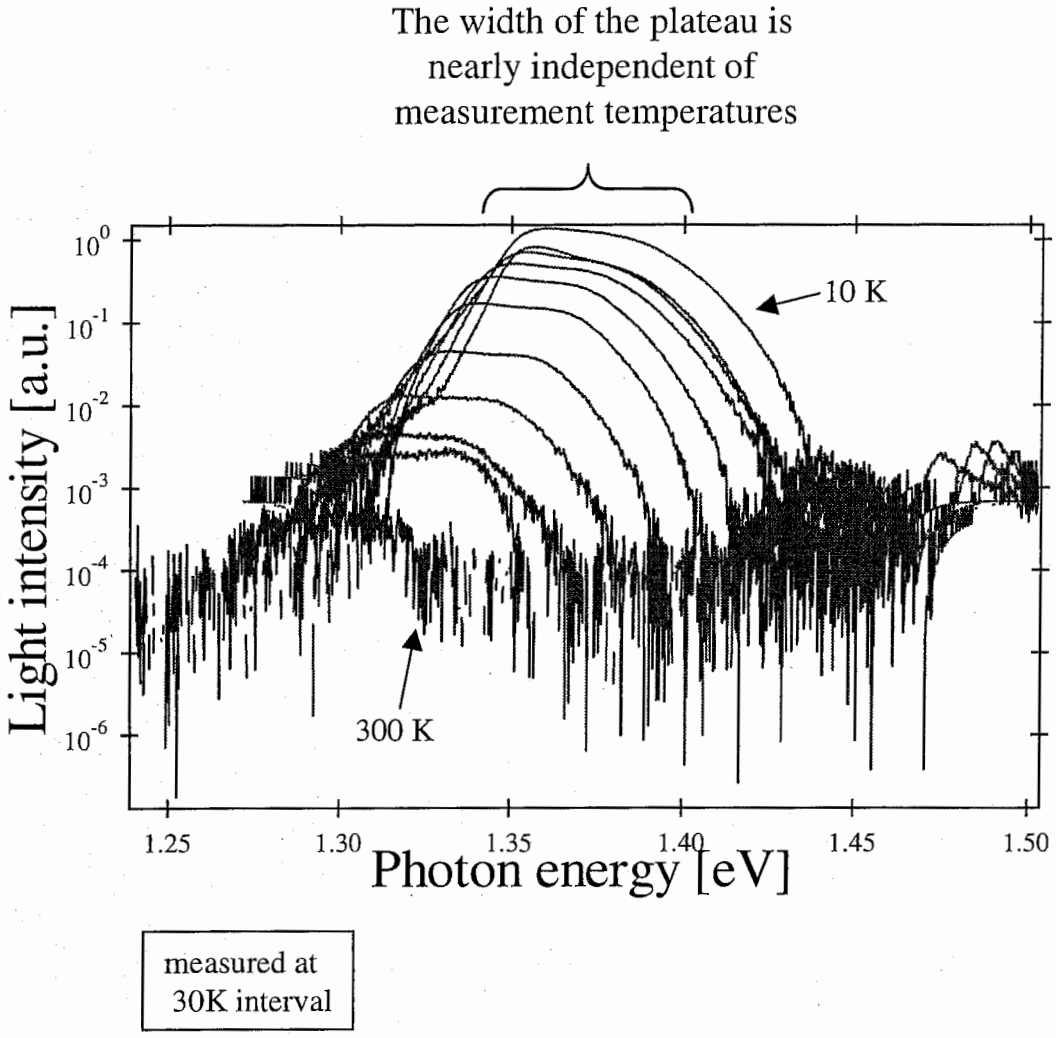

Fig. 4.10 EL spectra of Peak1 at various temperature.
The applied current was 2.0 mA.

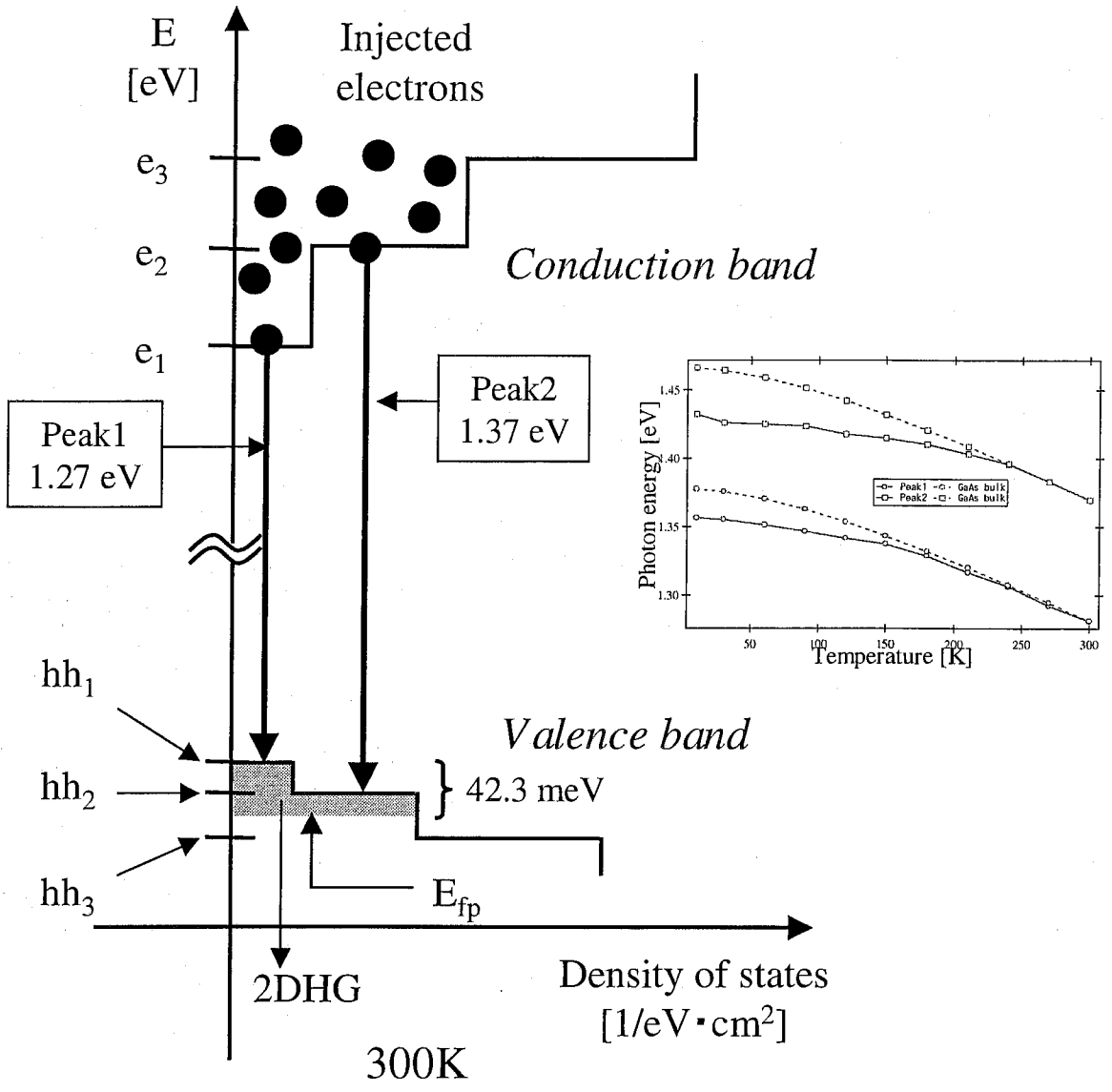

Fig. 4.11 Density of states and occupation of a p-type

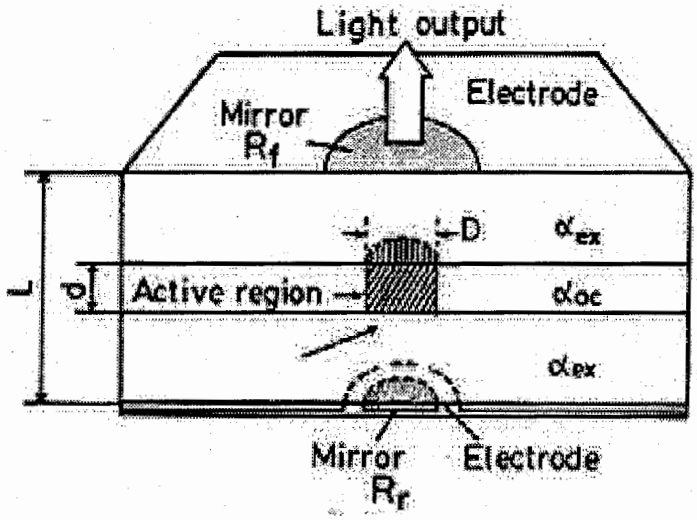

Fig. 5.1 A schematic diagram of a VCSEL

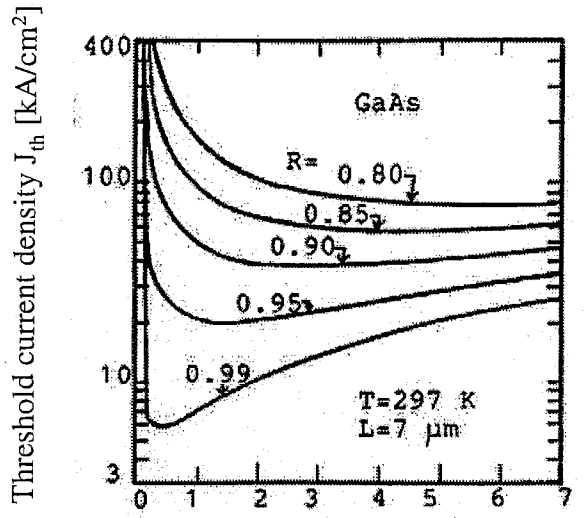

(a)

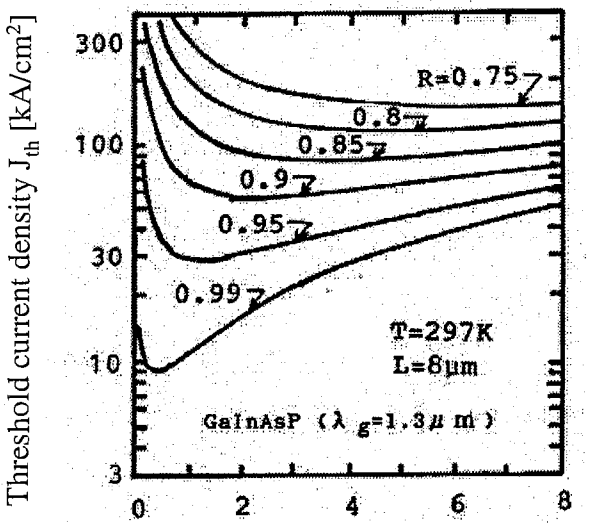

(b)

Fig. 5.2 Threshold current density against active layer for
(a) AlGaAs/GaAs VCSEL
(b) InGaAsP/InP VCSEL

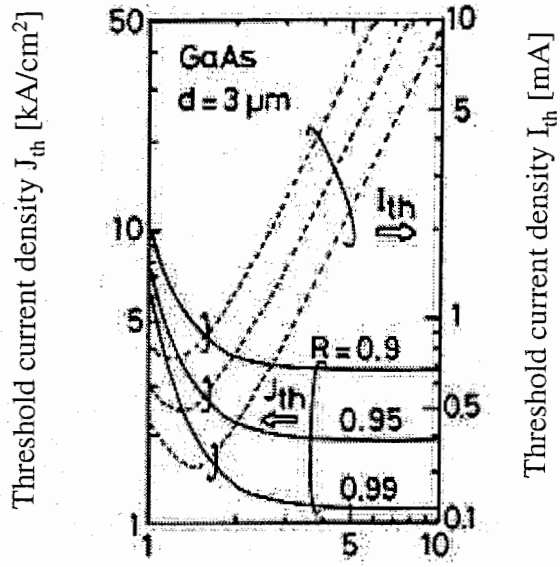

Fig. 5.3 Threshold current density (solid lines) and threshold current (dashed lines) against active region diameter for a AlGaAs/GaAs VCSEL

Growth temperature	▪540°C (311)A ▪580°C (100)
As_4-BEP (Beam equivalent pressure)	▪6.6×10^{-6} Torr (GaAs) ▪1.51×10^{-5} Torr (AlGaAs)
Growth rate	▪800 nm/h (GaAs) ▪343 nm/h (AlAs) ▪200 nm/h (InAs)
Carrier concentration	▪(311)A 3.81×10^{18} cm^{-3} (p-type) ▪(100) 3.04×10^{17} cm^{-3} (n-type)

Table 5.1 MBE Growth Conditions

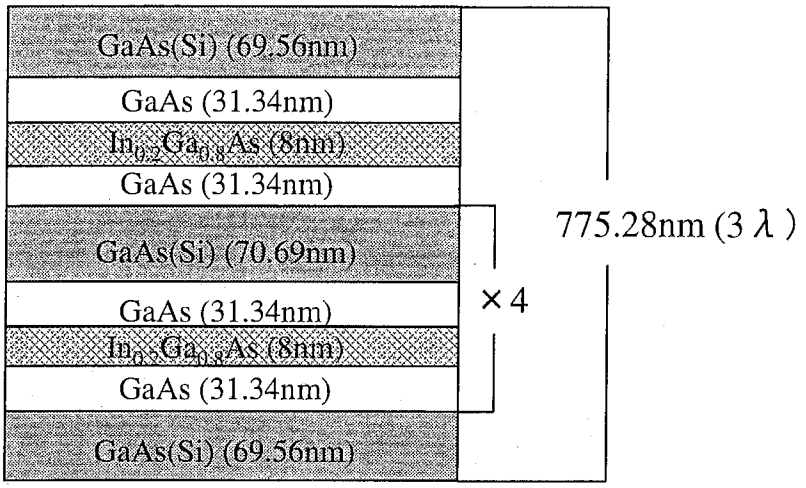

(a) An active layer

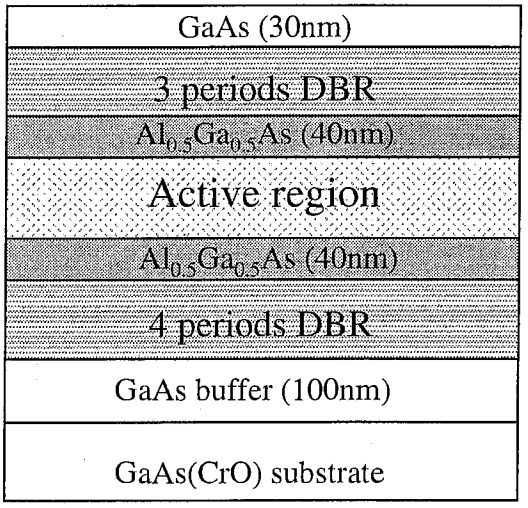

(b) The multilayer structure

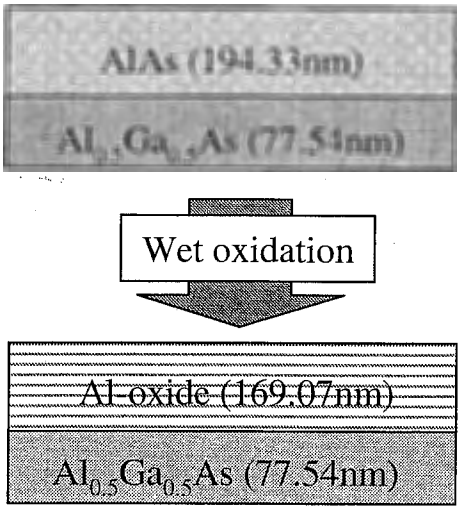

(c) DBR

Fig. 5.4 Cross section view of multilayer structures grown by MBE

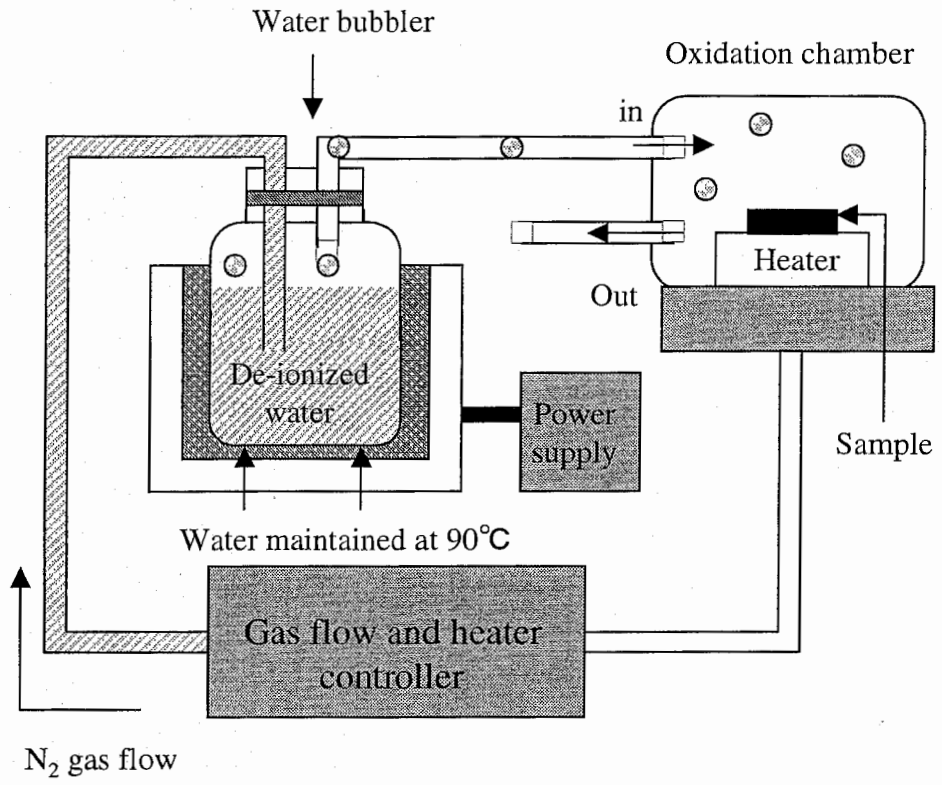

Fig. 5.5 A schematic drawing of the wet oxidation system

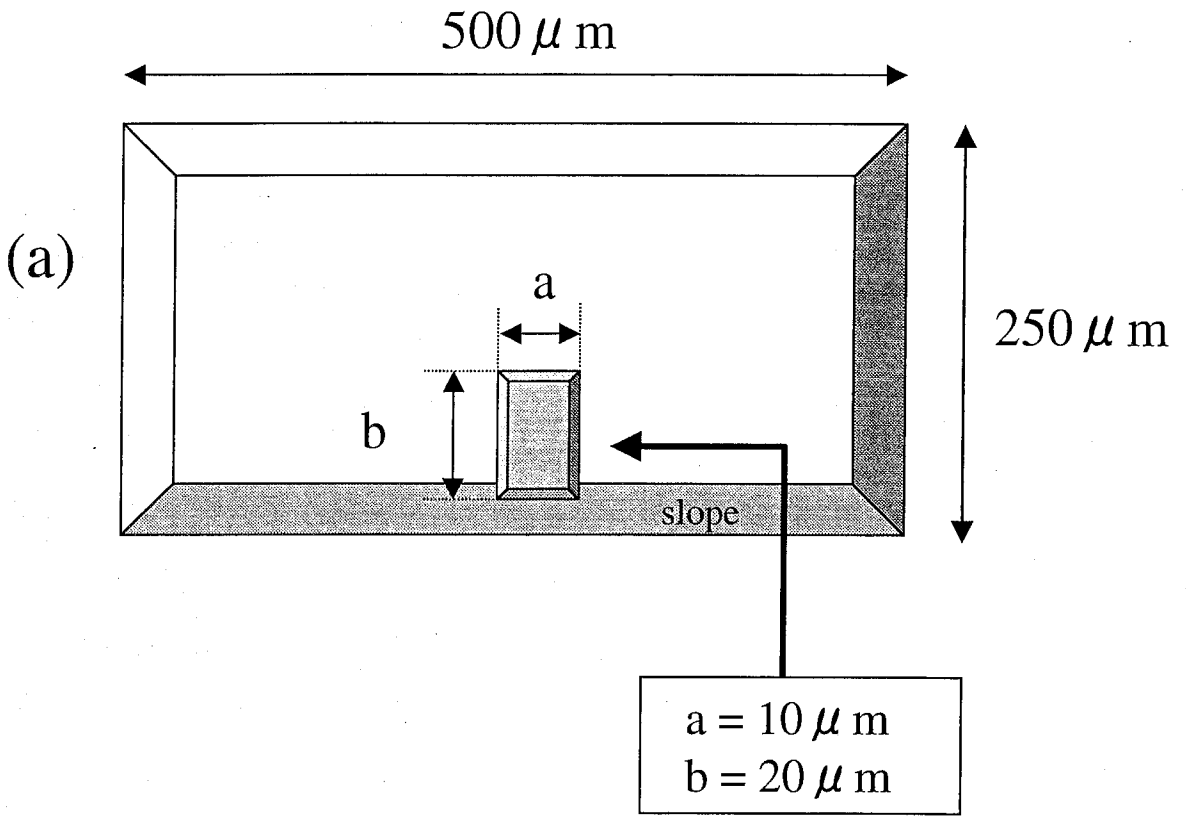

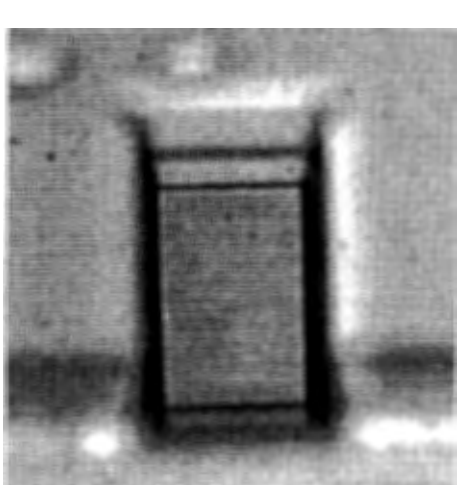

(b)

10 μ m

Fig. 5.6 Top view of the LJ-VCSEL
(a) Schematic illustration
(b) Optical microscope image

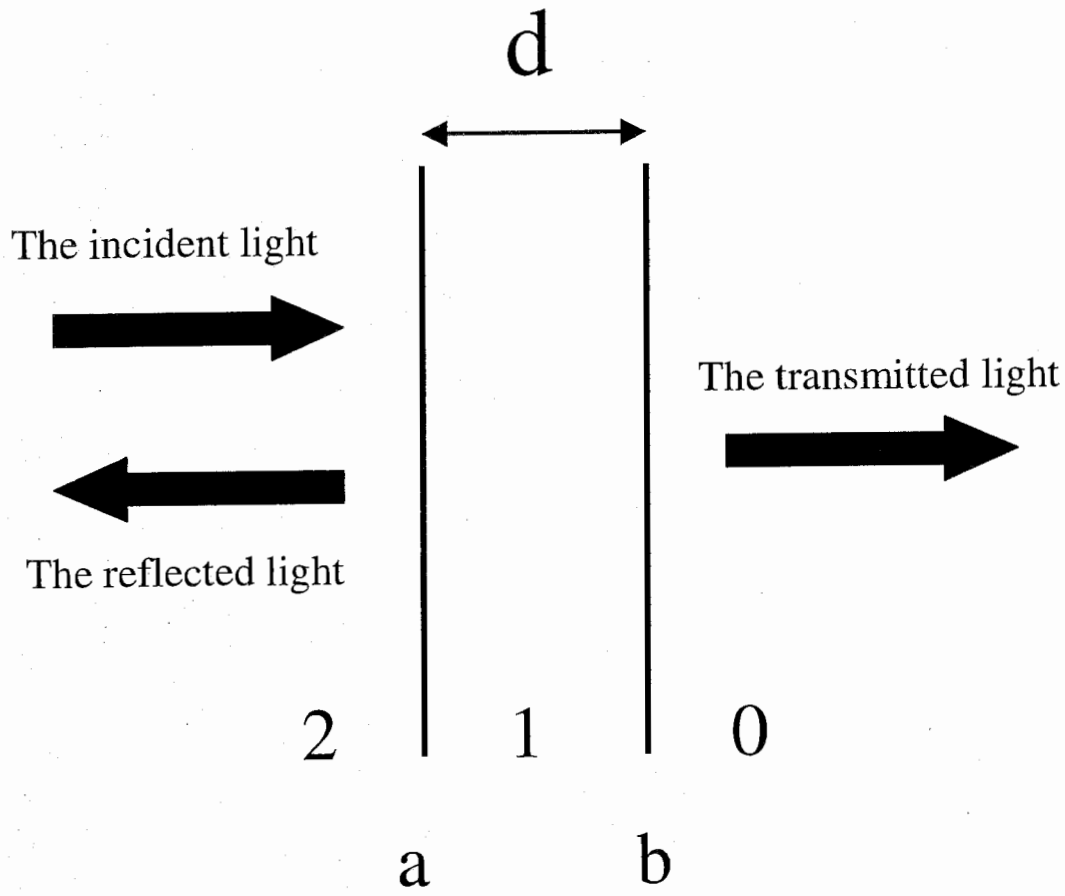

Fig. 5.7 Reflection and transmission of a dielectric slab

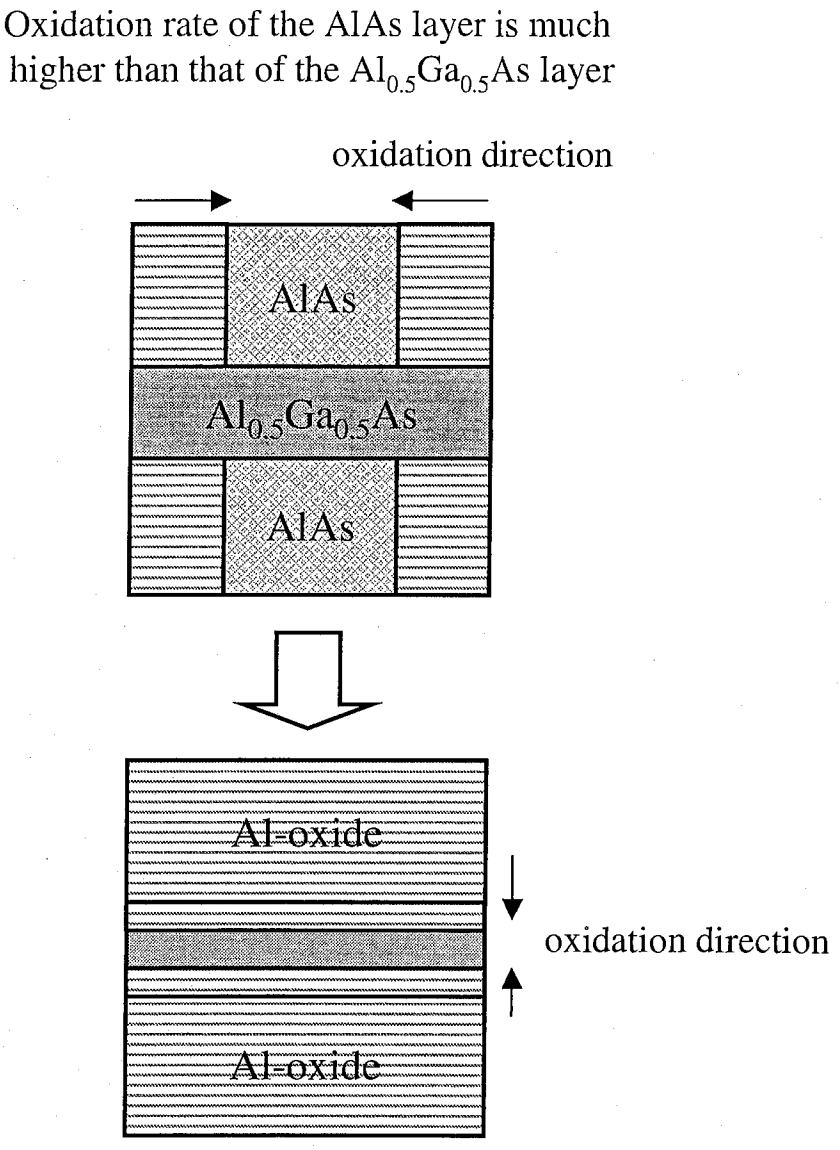

Fig. 5.8 An oxidation model of the AlAs/AlGaAs DBR

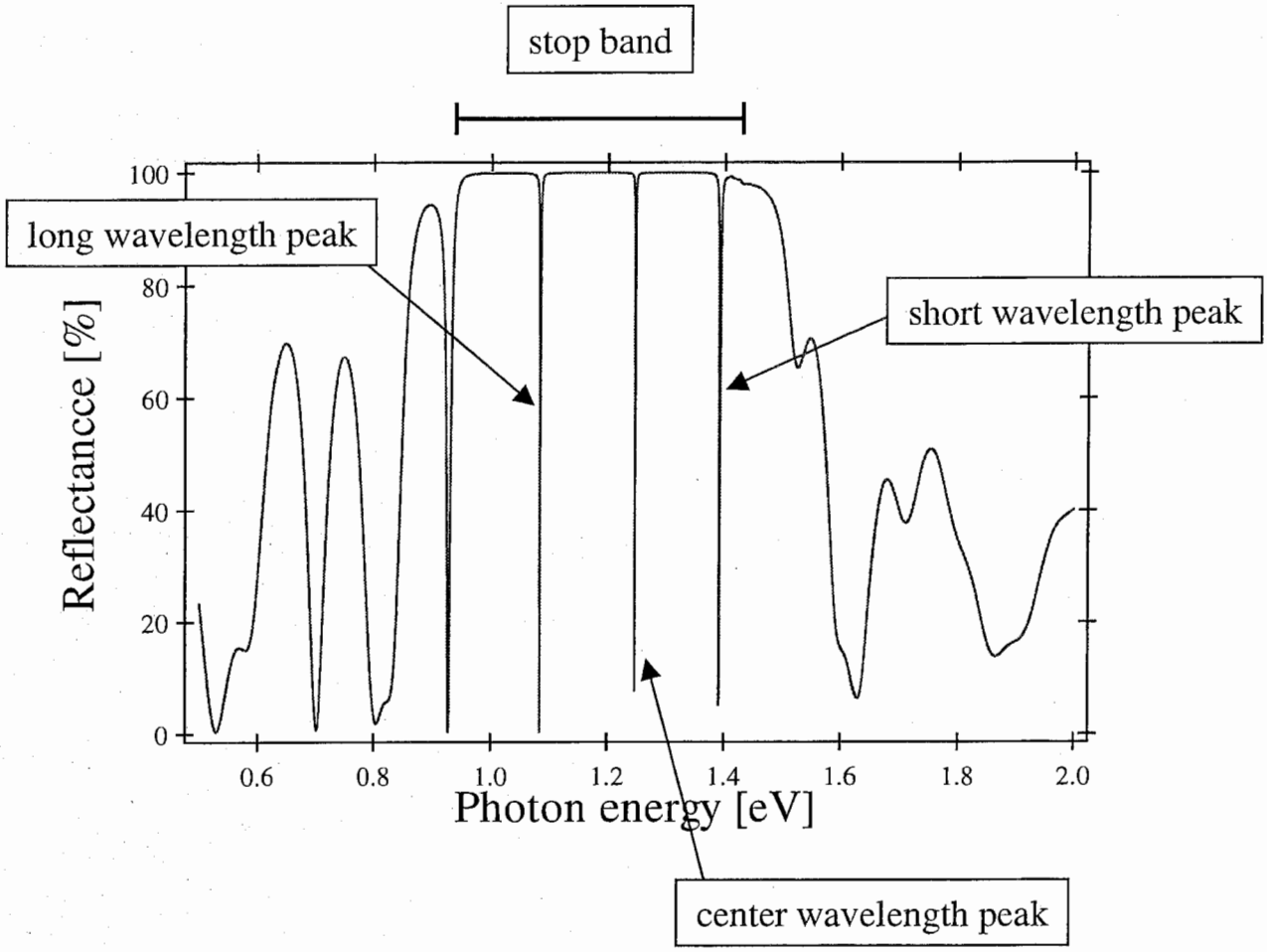

Fig. 5.9 Calculated reflectance spectrum of the LJ-VCSEL

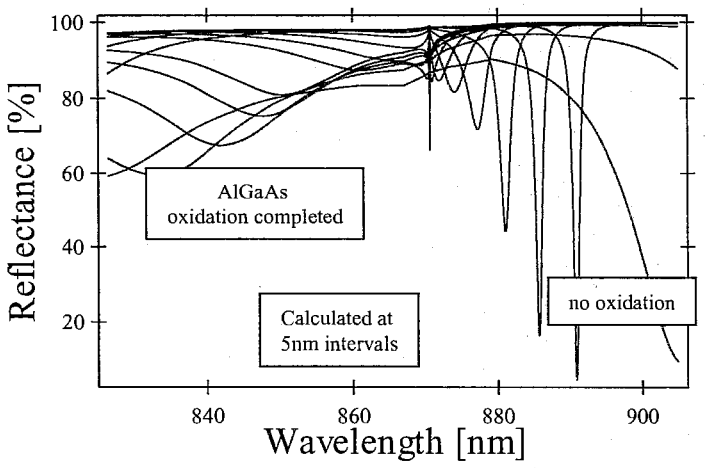

(a)

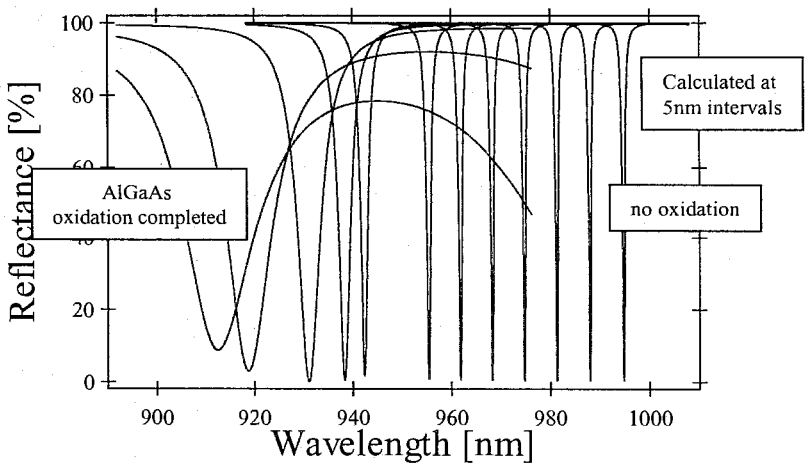

(b)

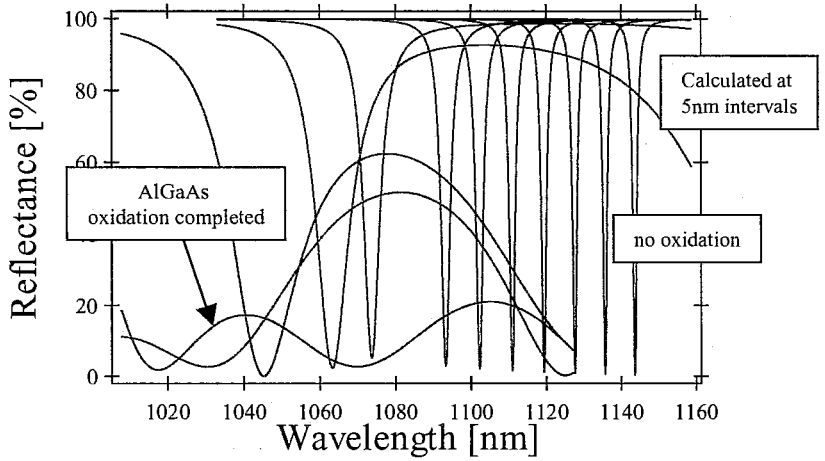

(c)

Fig. 5.10 The reflectance spectra dependence on an $Al_{0.5}Ga_{0.5}As$ oxidized layer width
(a) short wavelength peak
(b) center wavelength peak
(c) long wavelength peak

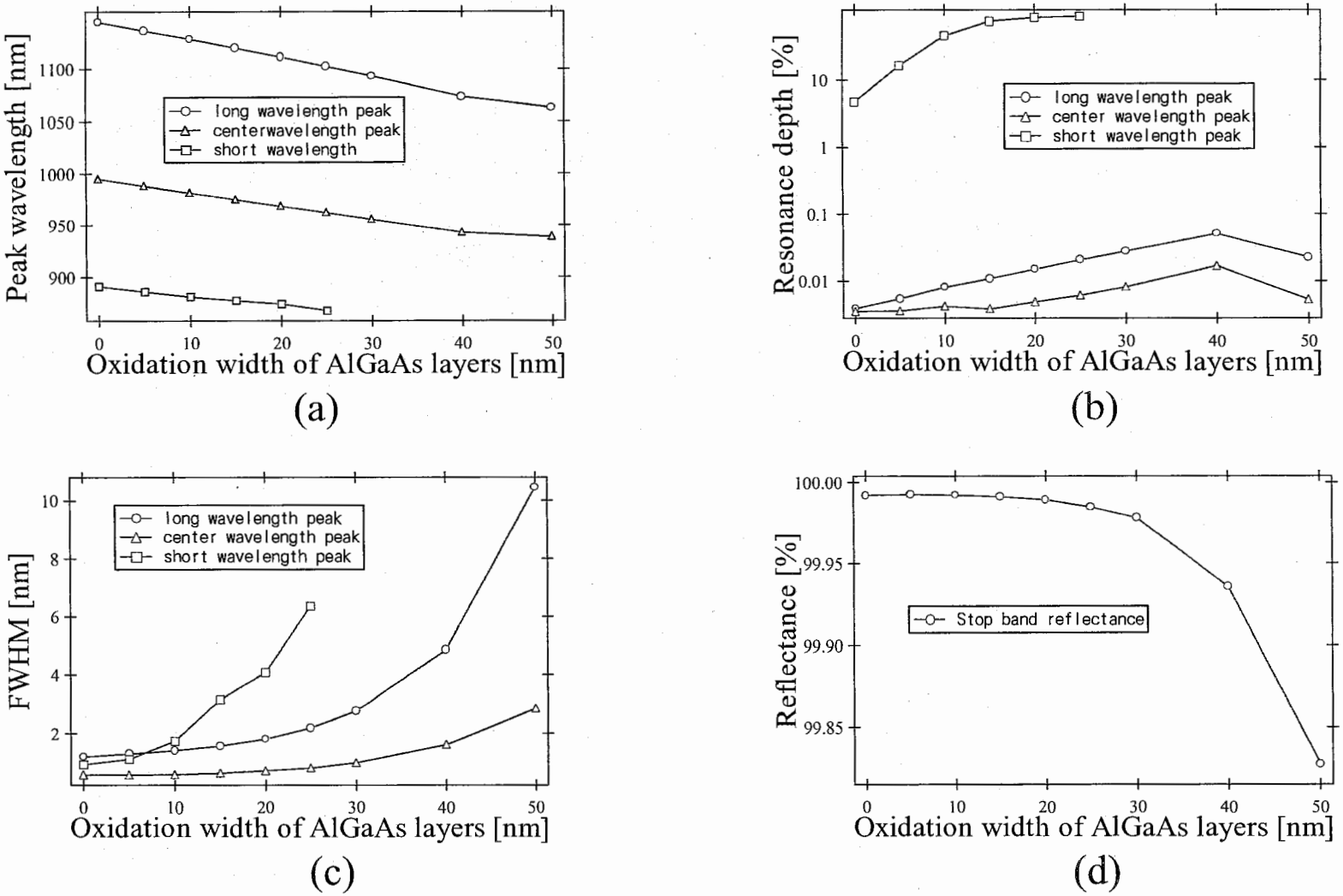

Fig. 5.11 The wavelength (a), resonance depth (b) and FWHM (c) of three resonance peaks and the stop band reflectance (d) as a function of the oxidation width of $Al_{0.5}Ga_{0.5}As$ layers

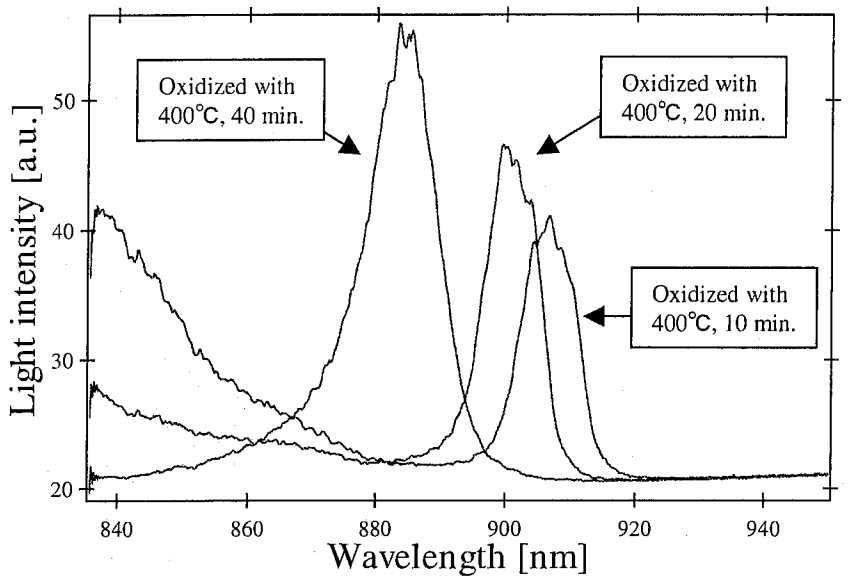

(a)

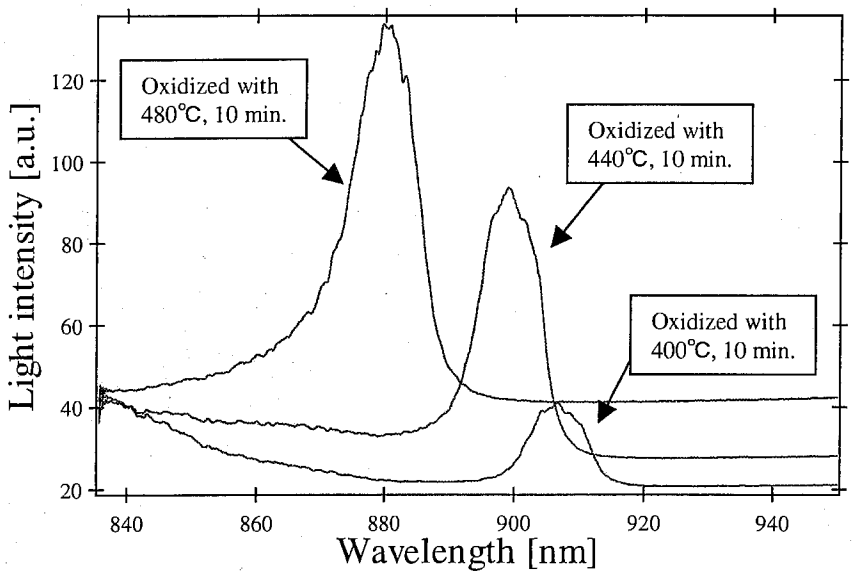

(b)

Fig. 5.12 PL spectra from the LJ-VCSEL with several oxidation conditions
(a) PL spectra dependence on oxidation time
(b) PL spectra dependence on oxidation temperature

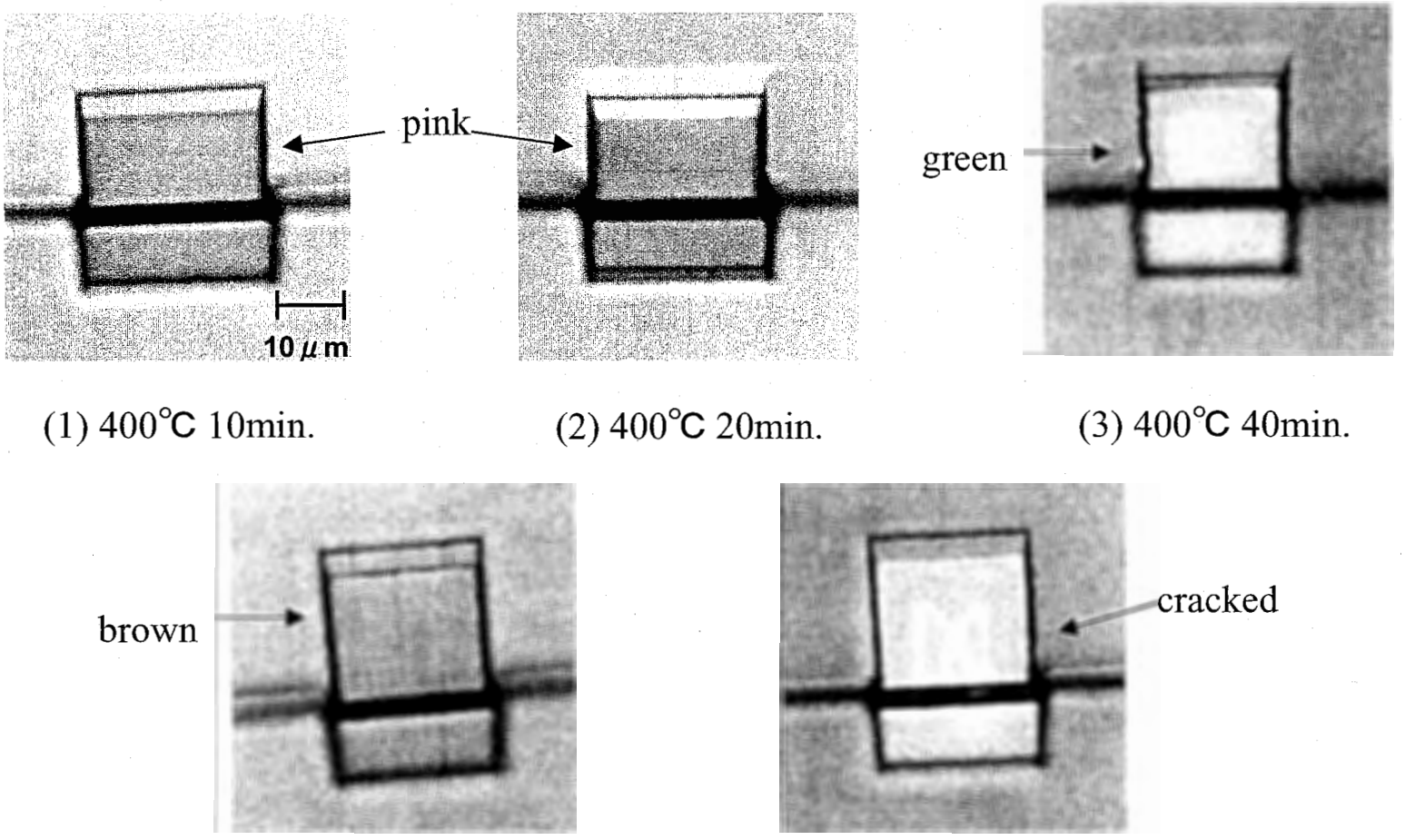

(1) 400℃ 10min.　(2) 400℃ 20min.　(3) 400℃ 40min.

(4) 440℃ 10min.　(5) 480℃ 10min.

Fig. 5.13　Optical microscope images of oxidized LJ-VCSELs

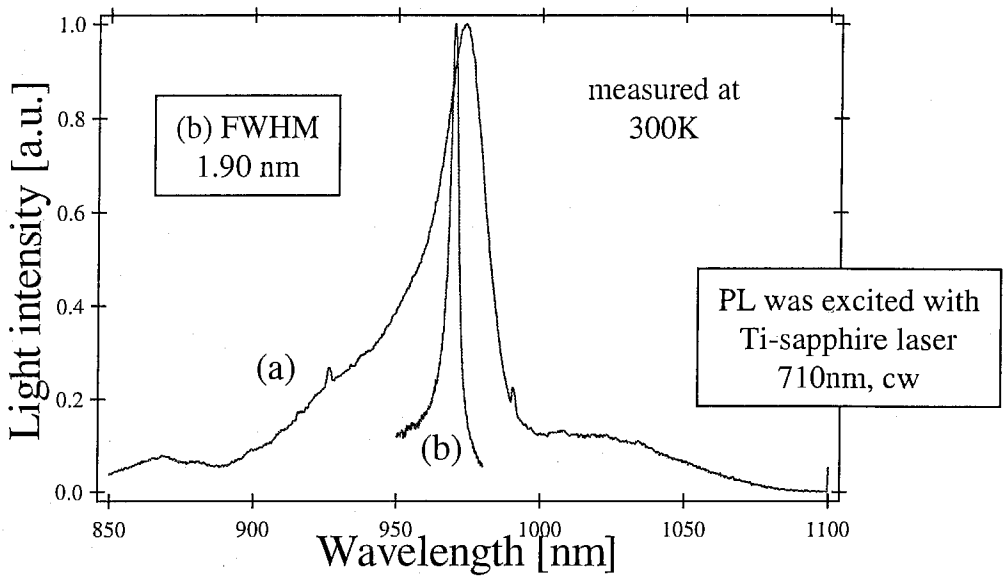

Fig. 5.14 PL spectra from the active layer
(a) measured before oxidizing of the DBR
(b) measured after oxidizing of the DBR

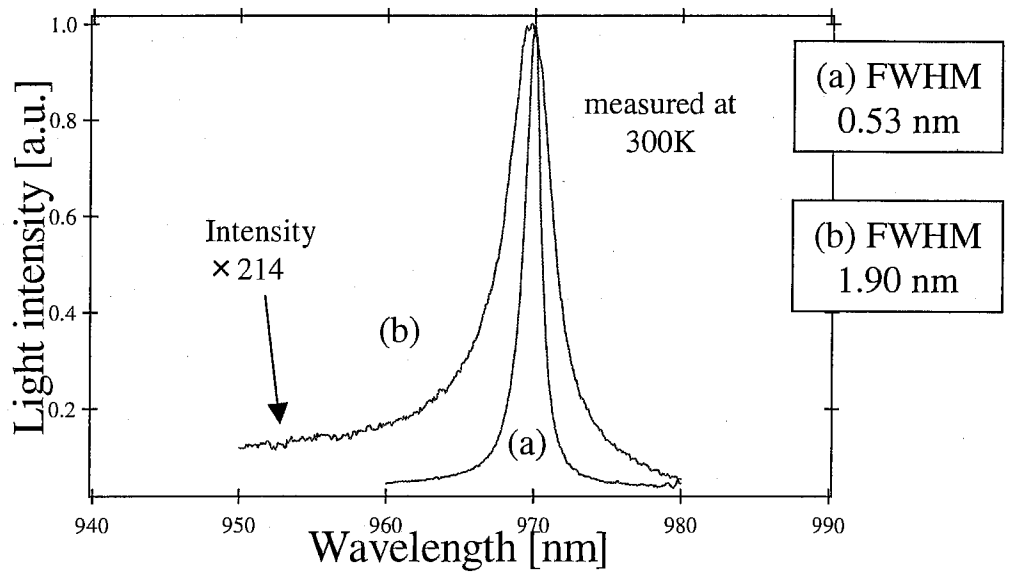

Fig. 5.15 PL spectra with (a) excitation laser powerof 60.6 mW and
(b) excitation laser power of 0.63 mW

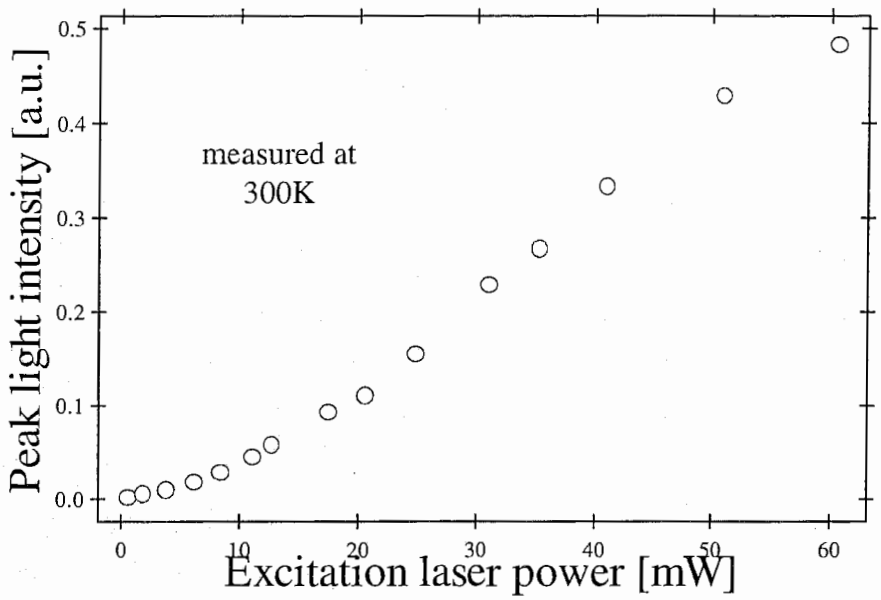

Fig. 5.16 PL peak intensity dependence on the excitation laser power

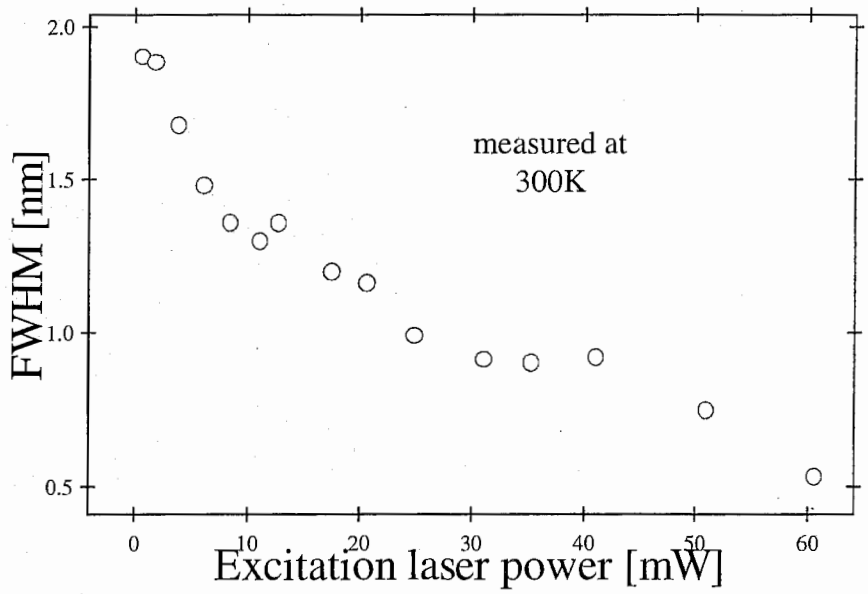

Fig. 5.17 FWHM dependence on the excitation laser power

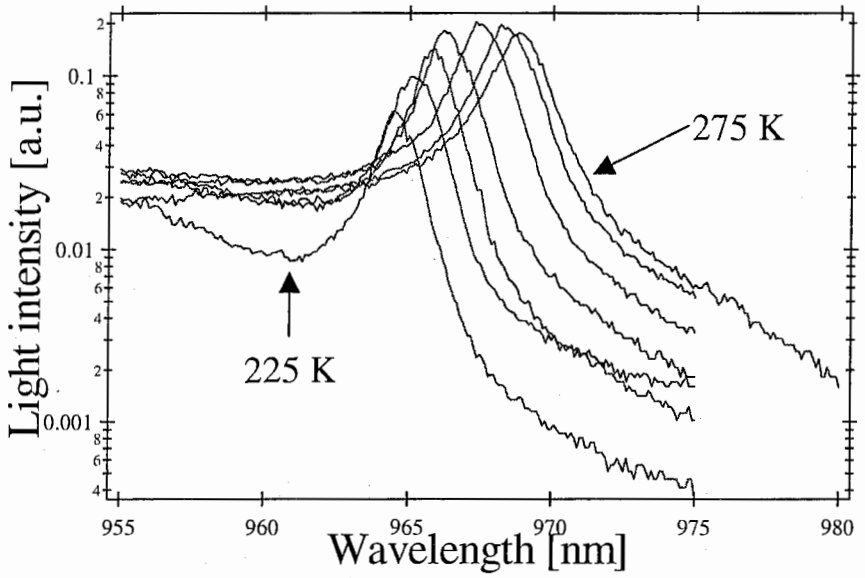

Fig. 5.18 PL spectra dependence on temperature

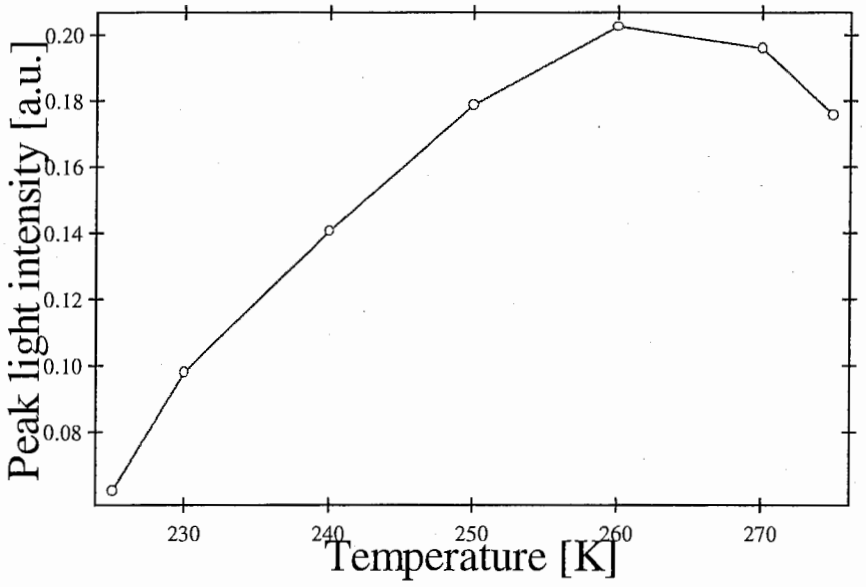

Fig. 5.19 PL peak light intensity dependence on temperature